



HAL
open science

Activated carbon nanofluidics: from blue energy to ionic memory

Théo Emmerich

► **To cite this version:**

Théo Emmerich. Activated carbon nanofluidics: from blue energy to ionic memory. Soft Condensed Matter [cond-mat.soft]. PSL, 2021. English. NNT: . tel-03603163

HAL Id: tel-03603163

<https://hal.science/tel-03603163>

Submitted on 9 Mar 2022

HAL is a multi-disciplinary open access archive for the deposit and dissemination of scientific research documents, whether they are published or not. The documents may come from teaching and research institutions in France or abroad, or from public or private research centers.

L'archive ouverte pluridisciplinaire **HAL**, est destinée au dépôt et à la diffusion de documents scientifiques de niveau recherche, publiés ou non, émanant des établissements d'enseignement et de recherche français ou étrangers, des laboratoires publics ou privés.

THÈSE DE DOCTORAT
DE L'UNIVERSITÉ PSL
Préparée à l'école normale supérieure

**Activated carbon nanofluidics:
from blue energy to ionic memory**

Soutenue par
Théo Emmerich
Le 06 décembre 2021

Ecole doctorale n° 564
EDPIF

Spécialité
Physique/Hydrodynamique



Composition du jury :

Aleksandra, Radenovic Pr, EPFL	<i>Presidente</i>
Fabien, Montel CR, ENS Lyon	<i>Rapporteur</i>
Laurent, Joly Pr, Université Lyon 1	<i>Rapporteur</i>
Radha, Boya Pr, the University of Manchester	<i>Examineur</i>
Lydéric, Bocquet Pr, ENS	<i>Examineur</i>

It is impossible for a man to learn what he thinks he already knows
– Epictetus

Acknowledgements

Developing nanotechnologies can feel ungrateful but is rewarding in the end. Resilience and self-confidence is required to repeat the same actions and improve a protocol for months and even years before it starts working. An advise I would give to someone developing a new nanotechnology: never believe that your protocol is perfect, there is always room for improvement in device quality or in reducing fabrication time.

I have been helped in many ways during this training and benefited from a truly exceptional scientific environment at the Micromegas research group. I am grateful to my amazing advisor Lyderic Bocquet for making me grow and become a scientist. Thank you for your major contribution into the project, thank you for your trust and thank you for providing unlimited material resources as well as exceptional scientific collaborators. You showed me how to conduct research with vision and ambition, I have benefited from your supervision immensely.

I am grateful to K.S Vasu for teaching me nanofabrication and his major contribution in the project. You showed me what being exceptional in the cleanroom means, in terms of skills and also resilience. I am grateful to Paul Robin for sharing his knowledge of memristors, neuroscience, and neuromorphic engineering as well as his major contribution in the project. It was an amazing, and productive, experience to move forward with you and I would be happy to keep working with you in the future.

I am grateful to Antoine Nigues, Michael Rostisher, Jose Palomo and Aurelie Pierret for their precious help regarding nanofabrication. I am grateful to Nikita Kavokine for being my theory book, for his kind words and for his awesome labview programs, working with you was a great chance. I am also grateful to Javier Perez for the nice introduction into the nice membrane-world and teaching me how to make graphene oxide membranes.

Thanks to the people of Micromegas for these nice three years: Mathieu, Sandra, Soufiane, Dounia, Baptiste, Nicolas, Mohamed, Amin, Sophie, Jean, Lucas, Antoine Laine, and the others I forgot. I hope I will find such nice people in my next group. Thanks to the ENS people of the administration: Nora, Zaire and Rachida; we had a lot of fun. Thanks to my friend who listened to me complain for hours when experiments were not working, thanks to my family for their support with a special mention to my dad who kept asking questions even though he had a poor understanding of the answers.

Thank to my love, Alice, for giving me the strength required to obtain the results of this work.

Foreword

Why studying ionic transport in small pipes ?

A first motivation is purely fundamental. Interfacial transport, driven by surface charge and hydrodynamic slippage, occurs less than one hundred nanometers away from the walls [1, 2]. Hence, for conduits with a larger confinement length, bulk dominates interfacial transport and the latest cannot be probed. One needs a pipe small enough to *feel* the interface.

A second one stems from a high potential for applications. Membranes with nanometric pores are required for water filtration, desalination and osmotic energy harvesting [3–7]. Reverse osmosis is currently a major technology; it consists in applying a pressure gradient across a water permeable membrane [8]. This process has limited efficiency and is limited by membrane fouling [9, 10]. By uncovering new interfacial phenomena, nanofluidics may enable paradigm shifts for the membrane industry. Electro or diffusio-osmosis are particularly interesting in that regard [8]. The production of clean energy and water are closely linked and the worldwide demands are ever more increasing. Efficient membranes are critical to foster the water energy nexus [11].

The last reason is the exceptional performances of biological channels for water and ionic transport. The latest is a key regulation process for living organisms [12]. It relies on nanometric and sub-nanometric pores with far more advanced functionalities than their artificial counterparts [13]. For instance, aquaporins have a very high water permeability while being impermeable to ions [14]. Another example are voltage-gated K^+ or Ca^{2+} synaptic channels enabling fine tuning of ionic transport, a key mechanism for adjusting the brain's activity [15, 16]. Reproducing such performances on artificial pores provides fundamental insights and is a milestone towards the realization of smart biomimetic membranes.

In order to pursue experimental investigations of nanoconfined fluids, the first step is to fabricate the conduit. This is actually an important, if not the most important, part of the job. Over the last two decades, nanofluidics technology has been booming fostered by the advent of nanomaterials and the progress of nanofabrication techniques [17–22]. In 2016, a particularly advanced platform developed by R. Boya et al., was put forward: the Angstromslits [23]. They allow control over the confinement down to a single atomic layer hence reaching the atomistic limit of matter. This technology enabled major advances regarding the study of ultra-confined water and ionic/protonic transport [24–27].

The initial goal of the P.h.D was to develop a technology, called retrospectively *activated* carbon nanochannels, taking inspiration from the Angstromslits, often referred to as *pristine* carbon nanochannels in this work. More than a source of inspiration, the latest will also be used as a benchmark for the activated channels here. We will see that the differences in nanofabrication process between pristine and activated channels result in a dramatic enhancement of ionic transport in activated conduits, justifying their appellation. In particular, activated channels are extremely efficient for the harvesting of osmotic (blue) energy coming from salinity gradients. In addition to having a high magnitude, ionic transport can also be exotic in activated nanochannels. We uncover a memory (or memristor) effect, meaning that the device's conductance can be strongly dependent on the channel's history. We will see that this memory is spanning over hour-long timescales and is analogous to synaptic plasticity. It can be used to perform brain-like, or neuromorphic, computations; the very last result of the thesis being the implementation of Hebb's rule on an activated carbon nanochannel.

The thesis is organized as follows :

- **Part I : Nanofabrication.** This part has for object to present some notions of nanofabrications and their use in making nanofluidic systems before presenting the protocol developed in this project. Chapter 1 presents relevant nanomaterials and nanofabrication techniques. Chapter 2 is an overview of some relevant nanofluidic devices, how they are made and what discoveries they enabled. Chapter 3 is a short and illustrated version of the activated nanochannels' fabrication protocol.
- **Part 2 : Enhanced ionic transport and (blue) energy harvesting.** Having developed a new device, we first started by characterizing it with classical methods as well as nanofluidic ones. We discovered that activated carbon nanochannels have outstanding surface properties resulting in an enhanced ionic transport. We then took benefit from these properties to perform efficient osmotic energy harvesting. Chapter 4 will provide a (simple) theoretical basis regarding nanofluidic transport. Chapter 5 will be a short review on osmotic energy: its potential and how it is harvested so far. Chapter 6 will be dedicated to our investigation of nanofluidic transport in activated carbon nanochannels compared to pristine carbon ones.
- **Part 3 : Iontronics.** By opposition to *electronics*, *iontronics* can be seen here as the development and study of ion-based devices performing complex tasks. This was made possible by the discovery of a memory (or memristor) effect in activated carbon nanochannels. Memristors are variable resistors with a memory. They are the electrical equivalent to biological synapses and thus enable to perform brain-like, or neuromorphic, computations. This part of the project is still ongoing. Chapter 7 provides basic knowledge concerning memristors, from theory to applications. Chapter 8 is a report on the memristor effect in activated carbon nanochannels. Finally, Chapter 9 presents our results on the use of activated carbon nanochannels as artificial synapses.

This work has resulted in one publication so far: Theo Emmerich, K.S.Vasu, A. Nigues, A. Keerthi, B. Radha, A. Siria, L. Bocquet. "Enhanced nanofluidic transport in activated carbon nanochannels". *Accepted at Nature Materials*. 2021.

Contents

Acknowledgements	3
Foreword	4
Contents	6
I Nanofabrication	9
1 The toolbox for nanofluidics with 2D materials	10
1.1 2D graphite	10
1.2 2D materials assembly	11
1.3 Patterning techniques	13
1.4 Transfer techniques	15
2 Nanofluidic Devices	17
2.1 Ultra-thin nanopores: 0D	17
2.2 Single transmembrane nanotubes: 1D	19
2.3 Pristine carbon nanochannels (Angstromslits): 2D, the inspiring technology	22
3 Development of a new technology: activated carbon nanochannels	25
3.1 Process-flow	25
3.2 Step 1: Patterning	25
3.3 Step 2: Top layer Dry Transfer	26
3.4 Step 3: Bi-layer heterostructure wet transfer on pierced SiN window	27
II Enhanced ionic transport and osmotic (blue) energy harvesting	30
4 Theory: ionic transport in slippery nanofluidic channels	31
4.1 Procedure	31
4.2 Governing equations	31
4.3 Surface properties	33
4.4 Transport quantities	37
5 A review of osmotic energy harvesting	43

5.1	Industrial potential and current limitations	43
5.2	Single Pores	44
5.3	Macro-scale membranes	47
6	Results: Enhanced nanofluidic transport in activated carbon nanochannels	49
6.1	Motivation and methods	50
6.2	Material characterization by conventional techniques	52
6.3	Nanofluidics material characterization	53
6.4	Osmotic energy harvesting	59
6.5	Main insights	61
III	Iontronics	62
7	Memristors: artificial memories	63
7.1	The fourth missing element	63
7.2	Solid state and nanofluidic memristors	67
7.3	Application as artificial synapses	71
8	Results: Memory effects in bidimensional carbon nanochannels	77
8.1	Motivation and methods	77
8.2	The memory effect	78
8.3	Main insight	82
9	Results: Long-term memory and synapse-like plasticity of activated carbon nanochannels	84
9.1	Motivations and methods	84
9.2	Characterizing the ionic memory	86
9.3	Programming the conductance	87
9.4	Implementation of Hebb's rule	88
9.5	Main insights	89
	Conclusion and perspectives	92
	Appendices	94
A	Development of a new technology : Activated carbon nanochannel (full protocol)	94
B	Nanofabrication : additional images of the devices	95
C	Enhanced nanofluidic transport :SI	98
C.1	O ₂ activated channels and characterization	98
C.2	XPS analysis	101
C.3	Nanofluidics measurements	102
C.4	Channels characteristics and modelling	112
C.5	Analysis of the surface properties	118

C.6	Benchmark activated carbon nanochannels performances	120
D	Up-scaling of energy harvesting	122
D.1	Multichannel devices	122
D.2	Measurements of macro-scale membranes	123
E	Data for the memory effect	127
F	Model for the memory effect (by P.Robin)	132
F.1	Qualitative discussion	132
F.2	1D model	133
F.3	Minimal model: 0D model	136
F.4	Dukhin slowdown	138
G	Data for the synaptic plasticity	141
	Bibliography	143

Part I

Nanofabrication

The toolbox for nanofluidics with 2D materials

2D materials have many qualities making them ideal building block to make nanoconduits. Using them to fabricate state-of-the art nanochannels requires an advanced hands-on knowledge. Here we provide basic descriptions of the material and techniques used in this work.

1.1 2D graphite

Since graphene synthesis in 2004 by Novoselov et al., 2D materials have become special toys for physicists [28, 29]. They have outstanding properties and were originally studied *per se*. With the development of nanofabrication techniques following their discovery, they are more and more used to fabricate nanotechnology platforms, in particular nanoconduits for the study of highly confined fluids. Such materials combine atomic flatness with outstanding interfacial and electronic properties. Their thickness can be as low as one atomic layer and controlled with atomic scale precision [30]. Therefore, they are ideal candidates as a material for nanofluidics technology. In this work we used 2D graphite as building block to develop and fabricate the activated carbon nanochannels. 2D graphite is a multilayer graphene crystal with a thickness lower than 100-200 nm (Figure 1.1.a-b). Its layers hold together because of van der Waals adhesion. Graphene is a flat, single layer, hexagonal lattice of carbon atoms. The hybridization of its atoms is therefore sp^2 and its thickness is 3.4 Å, a bit larger than water molecules (2.8 Å).

The choice of 2D graphite as a material for that project comes for two reasons. The first one is purely technical : it is the easiest 2D material to work with. Hence it is a pragmatic option for someone learning nanofabrication and *a fortiori* developing a new technology. The second one is that the couple formed by water and carbon is peculiar. In particular water have shown to exhibit little friction when flowing along carbon-based surfaces [31–33]. This will be described in more details in chapter 2 and 4. We mainly used crystals of thickness between 50 and 200 nanometers with clean and flat areas (Figure 1.1.b). They are obtained by mechanical exfoliation (Figure 1.1.c). This methods generates crystals of great quality meaning a minimal amount of defects (such as edges/missing atoms) relative to chemical vapor deposition techniques [34].

Nanofluidics devices generally relies on silicon nitride (SiN) membranes as substrates. Such materials have high mechanical strength and are not reactive nor

sensitive to high temperature. We also use such membranes in this work.

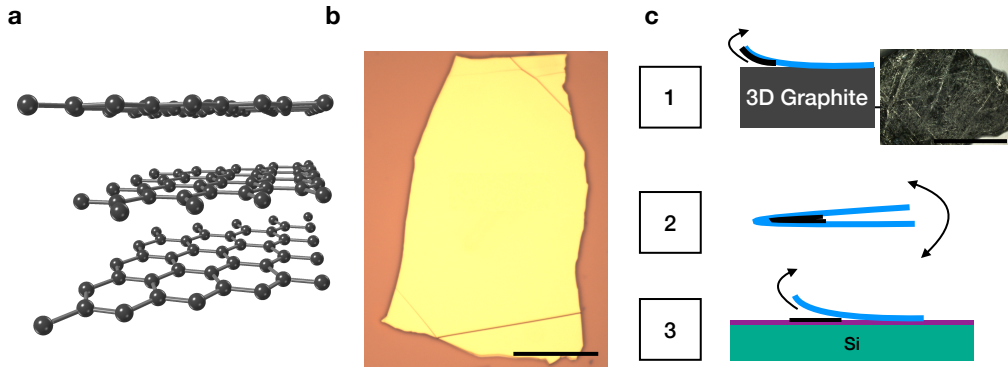


Figure 1.1

2D graphite and its exfoliation process. **a**, Schematic of a trilayer graphite crystal. Each of the layer is made of graphene. **b**, Optical microscopy image of a bidimensional graphite crystal with thickness of 50 nm. The substrate is Si/SiO₂. Scale bar is 20 microns. **c**, Exfoliation process to obtain mechanically exfoliated graphite. **Step 1** : Peeling of graphite layers from a 3D graphite flake. Left : schematic. The peeled graphite layers are represented in black and the tape in blue. Right : Optical microscopy image of a commercial 3D graphite crystal, from [35]. Scale bar is 1 cm. A cleanroom tape is pressed on a commercial graphite crystal and peeled-off which results in the transfer of graphitic layers onto the tape. This is possible because graphite is a graphene multilayer having weak Van der waals interaction between them. **Step 2** : Thinning of the exfoliated layers. The tape is folded on itself multiple times to reduce the graphite thickness. **Step 3** : Deposition on a substrate. Usually the substrate used is silicon with a 280 nm of silicon dioxide. This material favors optical contrast between thick and thin flakes enabling to guess the crystal thickness by their colors. The atomically thin graphene layers appears transparent purple (which is the color of SiO₂) and the thicker ones around 100nm yellowish to brownish.

1.2 2D materials assembly

Once a good enough crystal is found using optical microscopy, we should now fabricate nanoconduits. It is necessary to master at least one patterning technique to remove matter selectively. Being able to transfer a crystal from a substrate to another is also required. The detailed relevant patterning and transfer technique will be described in the next section. The latest enables 2D materials to be stacked up to create van der Waals heterostructures (Figure 1.2.a). Those nanostructures have a good mechanical stability because the layers are held together by Van der waals adhesion. Such realizations enable to reassemble matter in bidimensional layers with atomic scale resolution owing to a large library of available 2D materials to tune properties. In the last ten years it became a widely used nanotechnology platforms for various fields such as condensed matter physics, nanofluidics and nano-optics [36–39]. First nanofluidics Van der waals heterostructures, referred to as angstromslits or pristine channels in this work, were developed in 2016 by R.Boya et al. (Figure 1.2.b) [23]. Such devices allow the fundamental study of bidimensional

molecular and ionic transport with a great versatility because of their well-controlled geometry. Their fabrication process and some results they enabled will be discussed in the next chapter.

2D materials can also be used to fabricate macro-scale nanofluidics membranes. In particular graphene oxide (GO) membranes have attracted particular attention for their exceptional performances in ultra-fast permeation [40], ionic sieving [41], desalination [42] and osmotic energy harvesting [43,44]. The latest will be discussed further in chapter 6. Graphene oxide is an oxidized form of graphene carrying an important negative surface charge. Its performances have been attributed to the combination of low carbon/water friction and surface charge enabling high fluid permittivity and ion selectivity respectively. Its fabrication requires only vacuum filtration of commercially available GO aqueous solutions onto nylon or similar substrates. The GO layers self arrange to form a porous media (Figure 1.2.c). GO membranes can be tuned in many ways depending on the targeted application. It is not an expensive material nor is the membrane fabrication process. They are therefore highly promising for industrial applications.

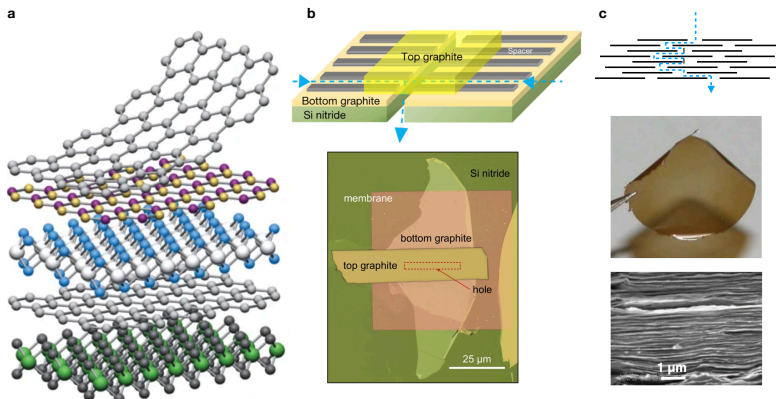


Figure 1.2

Assembly using 2D materials. **a**, Schematic of a van der Waals heterostructure with single layers of different materials, from [29]. 2D materials can be stacked on each other using transfer techniques (described in the next section). The lateral precision for positioning a layer is lower than one micron. **b**, Nanofluidics van der Waals heterostructure(angstroslits/pristine carbon channels), from [23]. Up: Schematic. Two bidimensional graphite crystals (bottom and top) are separated by an array of thin graphite nanoribbons named spacers. The fabrication of spacers will be described in the next section. The device is deposited on a SiN membrane having a rectangular aperture (hole) in its middle. The channels are made of the vacuum space between the spacers, the fluidic path is indicated by the blue arrows. Bottom : Optical microscopy image of a device. The spacer layer is not visible because of its low thickness. **c**, Graphene oxide membranes. Up : schematic. The graphene oxide sheets are stacked on each other. The interlayer distance is on the order of 1nm. The blue arrow indicates the fluidic path. Middle : Photography of a GO membrane held with a tweezer, from [40]. The membrane thickness is one micron. Bottom: Electron microscopy image of the membrane cross section, from [40].

1.3 Patterning techniques

Being able to remove matter is essential for fabricating nanoconduits with 2D materials. Such an operation is called patterning in our context. Here the patterning technique used to fabricate the angstromslits is discussed as well as the one used to fabricate activated carbon nanochannels for comparative purpose. There exists other techniques such as focused ion beam drilling [45, 46], or electrochemical etching that is briefly mentioned in the next chapter.

To fabricate the graphite nanoribbons array used as spacer in the pristine channel assembly, a thin graphite crystal is selected. Its thickness can be determined with atomic precision simply by using optical contrast [30] and it defines the channel's height. It is then patterned via electron-beam lithography (EBL) followed by reactive ion etching (RIE) (Figure 1.3.a). EBL consists of patterning a Polymethyl methacrylate (PMMA) resist layer previously spanned on the crystal thanks to a scanning electron microscope (SEM). RIE occurs in a chamber where an oxygen plasma is created that etch the exposed graphite. This technique is widely used in nanofabrication, in particular in condensed matter physics [47].

On the other hand, we use another technique to fabricate the activated carbon nanochannels (the protocol is given in chapter 3 and 4) : electron beam induced direct etching (EBIE). This technique consists of exposing the graphite to an electron beam in a low pressure water vapor atmosphere. This is done using an environmental SEM. Water molecules are turned into radicals by the electron beam which results in a local etching of the material [48, 49]. This technique was originally developed to cut nanotubes [48] and used more recently to etch selectively graphene [49] or hexagonal boron nitride [50].

The three main advantages of EBIE over EBL/RIE is that it is less complicated, does not require a PMMA sacrificial layers that always leaves contamination and it enables making pattern with non homogeneous thickness. The latest will be precious for the fabrication of activated carbon nanochannels (see chapter 3). The two main advantages of EBL/RIE over EBIE is that it has a higher spatial resolution (10 nm vs 100 nm) and it enables removing a lot of matter rapidly making possible for the pristine carbon nanochannels to count up to 200 channels. On the other hand, as making one channel with EBIE takes approximately 10 minutes, activated channels made by EBIE count a single or a few channels.

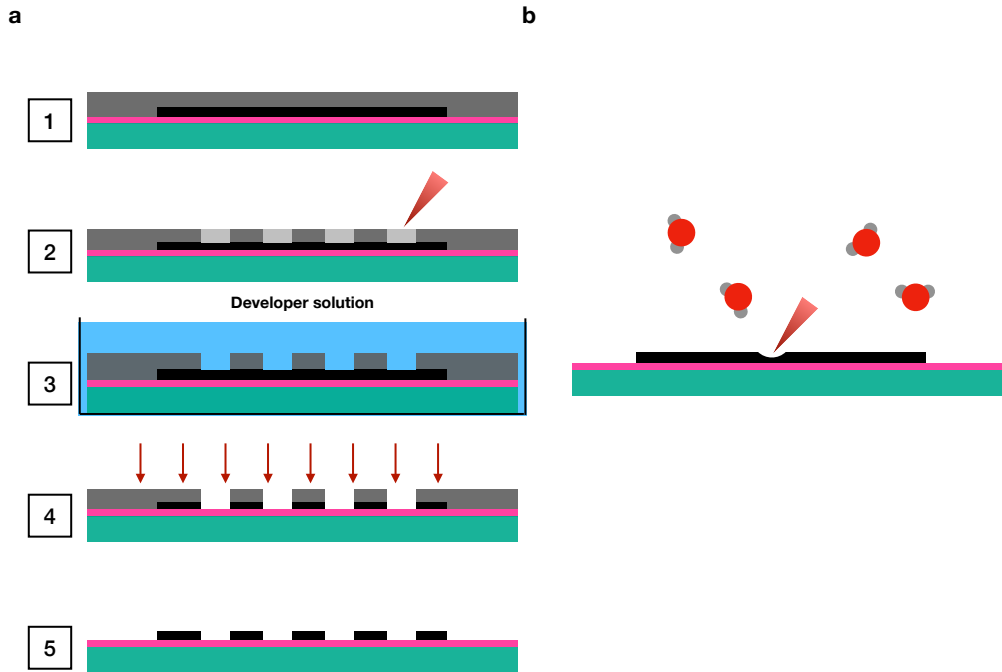


Figure 1.3

Two different techniques to pattern 2D materials. a, Electron beam lithography (EBL) and reactive ion etching (RIE). **Step 1:** Sacrificial PMMA layer spinning. A 2D crystal (in black) is spin coated with a layer of PMMA. The green/purple substrate is Si with a 280 nm SiO₂ layer as in Figure 1.1. **Step 2:** Electron beam exposure. The area to be etched are exposed to the electron beam in a SEM. For a successful process the SEM parameters have to be carefully set. **Step 3:** Development. The substrate is immersed into a developer solution removing the exposed PMMA that became more soluble. **Step 4:** Reactive ion etching. The substrate is placed into a vacuum chamber filled with low pressure O₂. RF wave create oxygen plasma with very reactive species (radicals). **Step 5:** Cleaning in acetone to remove the PMMA. **b,** Electron beam induced direct etching (EBIE). The substrate with the chosen crystal is placed inside a SEM chamber in low pressure water vapor (0.1mbar). Under the electron beam, water molecules become highly reactive radicals. They react locally with the material inducing etching in the vicinity of the beam spot.

1.4 Transfer techniques

The other key nanofabrication technique to master is 2D materials transfer enabling the assembly of van der Waals heterostructures. Transfer consists in placing a 2D crystal from a substrate to another with micrometric precision. This is done inside the cleanroom using a so-called "transfer station". Its made of two high precision micromanipulator stages, a hot plate and a microscope with long working distance lenses. There are two main ways to realize transfer: the dry transfer (Figure 1.4.a) and the wet transfer (Figure 1.4.b). Dry transfer consists of putting into contact a crystal from an initial substrate A to a target substrate substrate B (with eventually a 2D crystal on it) using a sticky polymeric transparent stamp. Wet transfer consist of spinning with a PMMA layer the substrate A with the flake to transfer. The substrate is then dissolved and the PMMA layer with the flake is collected. Finally the film made of the PMMA layer with the flake is placed on the targeted substrate B before being dissolved with acetone.

Hence the main difference is that dry transfer plays on crystal/stamp vs crystal/substrate adhesion whereas wet transfer does not involve adhesion because the substrate A and the stamp (PMMA layer in that case) are subsequently dissolved. The main advantages of dry transfer over wet transfer is that it is faster, easier, more precise and also cleaner (flake's bottom interface is in contact with air vs liquid potassium hydroxide (KOH) solution for the case of wet transfer). The main advantage of wet transfer is that, because it does not involve adhesion competition, it results in minimal stress on the crystal to transfer. Dry transfer may tear and brake the flake, nanometric pattern can also deform after a dry transfer. Hence precious patterned crystals should always be moved using wet transfer method. For easily replaceable ones dry transfer is more convenient. For fabricating activated carbon nanochannels both techniques are used (chapter 3).

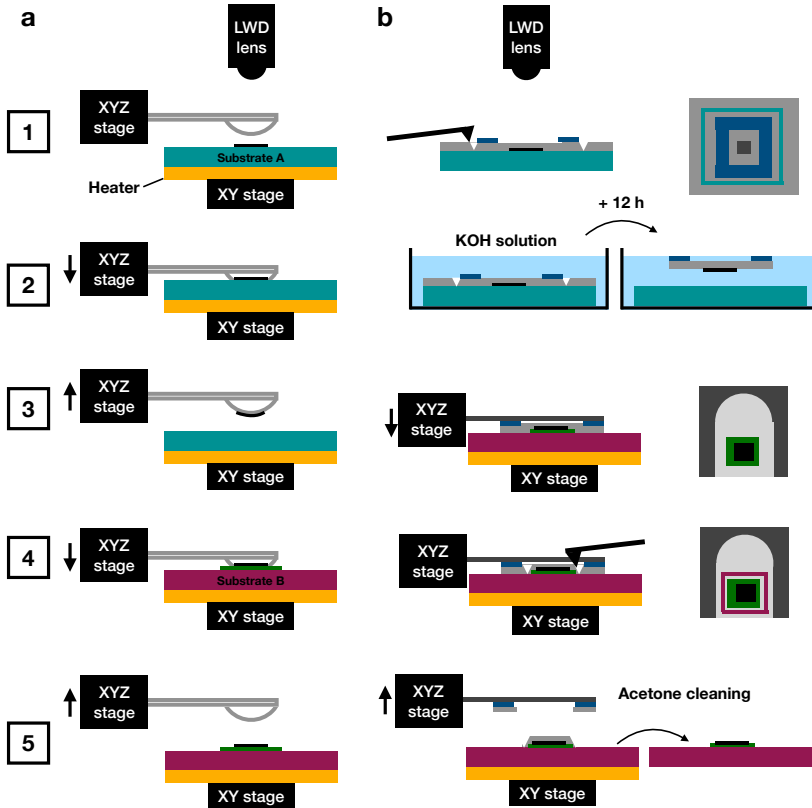


Figure 1.4

2D materials transfer techniques. **a**, Dry transfer. **Step 1:** Apex alignment. The apex of a droplet-shaped PDMS stamp spin coated with PPC (see full protocol in chapter 4 for more information) is aligned with the crystal to lift (in black) and the microscope lens. **Step 2:** First contact. Using z-axis the stamp is lowered until coming into contact with the crystal. **Step 3:** Pick-up. By moving the z-axis up the crystal detaches from substrate A and stays on the stamp. **Step 4:** Assembly. The crystal is carefully aligned with its targeted location (green 2D crystal on substrate B) and lowered to put them in contact. **Step 5:** Removal. A hot plate is used to heat the PPC which becomes less adhesive. The stamp is slowly lifted up leaving the black crystal on top of its target. **b**, Wet transfer. **Step 1:** Transfer preparation. The substrate is spin-coated with PMMA (grey layer) and a rectangular tape piece (in blue) with an aperture in its middle is placed on it making sure the crystal is in the middle of the aperture. The PMMA just outside the tape is then scratched manually with a tweezer. Left : side view the tweezer is represented in black. Right : top view. The green lines are area where PMMA has been removed by the tweezer. **Step 2 :** Etching. The substrate is placed inside a beaker filled with a KOH solution. The KOH enters in contact with the substrate trough the aperture made in the PMMA using the tweezer. After 12 hours the SiO_2 sacrificial layer of the substrate has been etched and the tape with the PMMA and crystal below detaches from it. **Step 3 :** Assembly. The tape with PMMA/crystal is carefully collected and attached to a transfer arm (in dark grey) and aligned with the targeted substrate. It is then placed into contact with the targeted substrate using the z-axis. Left : side view. Right : top view. The transfer arm has a "fork shape" so the crystal to transfer remains visible. **Step 4 :** Second scratch. The PMMA is scratched manually with a tweezer around the crystal to desolidarise it from the arm. The tape is not represented for simplicity in the top view. **Step 5 :** Removal. The arm is finally lifted up. The sample is washed in acetone to remove the PMMA layer.

Nanofluidic Devices

Over the last two decades, advances in fabrication have enabled the design of ever smaller channels until reaching the ultimate atom-scale limit. The more recent development of nanofluidic technologies often relies on nanomaterials. Here we will describe a few of those devices; how they are fabricated and the breakthrough they enabled.

2.1 Ultra-thin nanopores: 0D

Here we present the fabrication method developed by Feng et al. in [51]. Previous thin (a few atomic layers) nanopores drillings have been realized using focused ion beam (FIB) [36] or transmission electron microscope (TEM) [52] but such techniques are more complicated and less precise and therefore not presented here. Fabricating ultrathin nanopore using 2D materials is a 2-step process. First a CVD grown thin 2D material [MoS₂ for the case of Feng et al. [51]] layer is transferred above a pierced SiN window (Figure 2.2. step 1). Second, a nano-pore is opened via electrochemical etching (Figure 2.2. step 2). There are two main advantages to such a nanofabrication. The first one is that the number of steps is relatively limited compared to nanotubes and even more nanochannels/slits which are presented below. Another one is that electrochemical etching enables a measurement in real time of the pore diameter. As the pore size increases, its conductance increases as well and its diameter can be obtained using the conductance formula [51] :

$$G = \sigma \left[\frac{4L}{\pi d^2} + \frac{1}{d} \right]^{-1} \quad (2.1)$$

With σ the conductivity of the solution, L the pore thickness and d its diameter.

Hence, thanks to the use of 2D materials and electrochemical etching, one can obtain nanopores with atomic scale precision on thickness and diameter (Figure 2.2.a). Single or bi-layer MoS₂ nanopores have enabled fundamental discoveries and are promising candidates for a few applications. Non-linear transport inside nanopores with diameters below 0.8 nm have been attributed to ionic Coulomb blockade (Figure 2.2.b) [53]. Taking benefit of the high viscosity and conductivity of ionic liquids, MoS₂ nanopores have also displayed great potential for DNA sequencing, enabling the detection of single nucleotides (Figure 2.2.c) [54]. Finally, this nanofluidic device holds the record for energy harvesting in term of single pore power density [55]. This will be discussed in the chapter 6 of the thesis as it is closely related to this work.

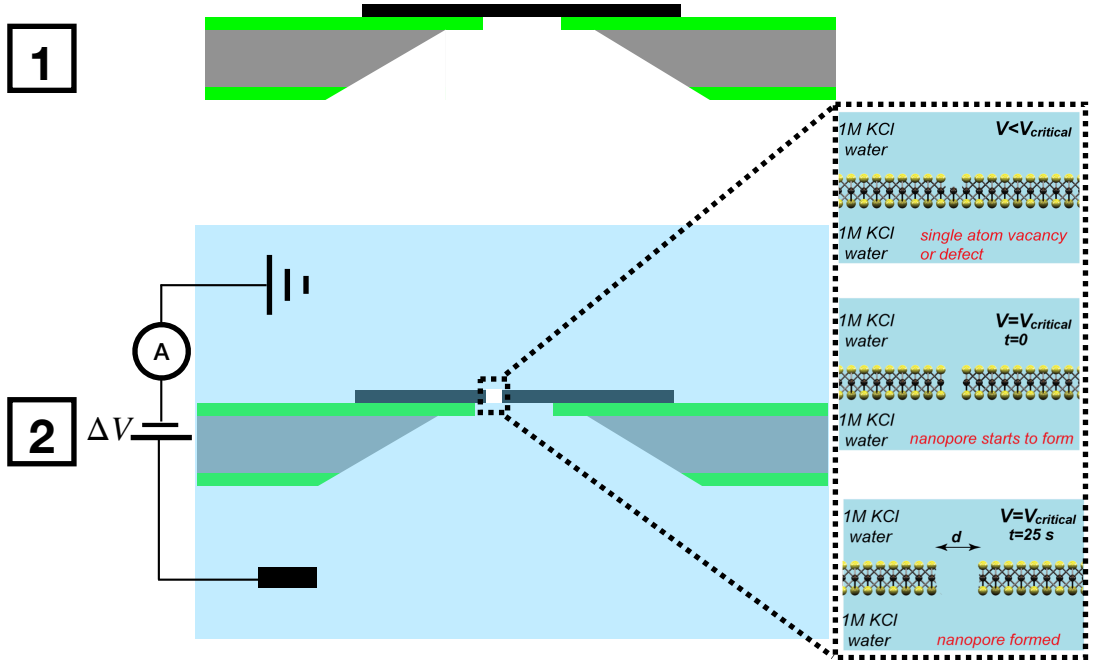


Figure 2.1

Nanopore fabrication. Step 1 : CVD grown MoS₂ wet transfer above a SiN window with an aperture (made by FIB). **Step 2 :** Electrochemical etching of the nanopore. The assembly is immersed into a nanofluidic cell filled with a 1M KCl solution. Zoom up : The potential is gradually increased resulting in an increase of a leakage current. Zoom middle : When a given threshold voltage ($V_{critical}$) is reached, an electrochemical reaction occurring at a vacancy/defect location starts which results in the formation of the nanopore. This corresponds to an abrupt change of conductance as the ions start flowing through the pore [51]. Zoom bottom: By keeping the potential at $V_{critical}$, the pore is enlarged. Zoom images from [51].

Even though nanopores have outstanding functionalities because of their atomic thickness, they are not *a priori* the best devices for the fundamental study of interfaces precisely because they have a close-to-zero liquid/solid interfacial area. Such studies have been fostered by the development of individual transmembrane nanotube setup presented in the next section.

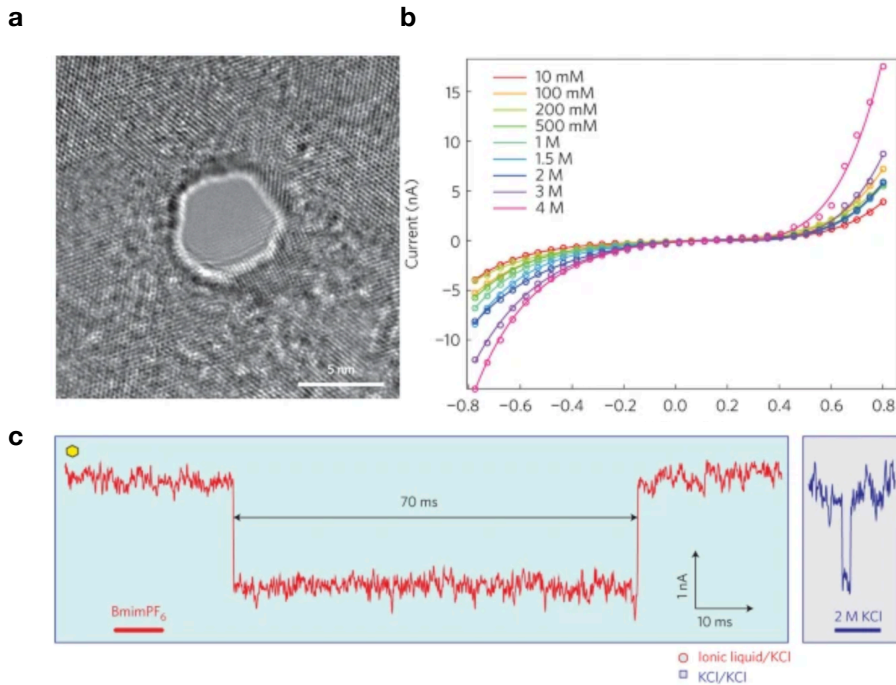


Figure 2.2

Nanofluidics to angstrofluidics with atom-thick nanopores. **a**, TEM image of a MoS₂ nanopore, from [54]. Scale bar : 5 nm. **b**, Ionic current vs applied voltage in a 0.6nm MoS₂ nanopore submerged in KCl at various concentrations, from [53]. The pore behaves as a potential well with an energy barrier (charging energy) much higher than the thermal energy. Ions are able to flow only if an applied bias of sufficient magnitude is applied to overcome the charging energy. **c**, Current vs time during a DNA translocation event inside a MoS₂ nanopore, from [54]. The cis reservoir is filled with DNA and ionic liquid (left) or KCl solution (right). The trans reservoir is filled with a KCl solution (left and right) DNA. When a DNA molecule goes through the pore, a current drop is observed. The value of the current drop is related to the nucleotide type. Using a high viscosity ionic liquid in the cis reservoir enables to slow down the DNA motion which facilitates distinguishing one nucleotide from another.

2.2 Single transmembrane nanotubes: 1D

The study of 1D water and ionic transport started with nanotube membranes, nanotubes being held together by an impermeable lipidic or epoxy matrix [21, 56]. In particular the study by Holt and al. was the first experimental evidence of an anomalously fast water flow in carbon nanotubes pointing to a special water/carbon interaction [21]. However to obtain the most reliable information on materials, the study has to be made on a single pore to avoid averaging over many pores. Such an average may lead to mistakes because of incorrect pore number and eventual inter-pore effects. The realization of a single nanotube membrane was achieved in 2013 by Siria et al. [57]. The authors fabricated the device inside an environmental SEM using a nano-manipulator, electron sensitive glue (naphthalene) and EBIE to

move, glue or cut a single nanotube respectively. The nanotube can be inserted into a pierced SiN membrane for the study of ionic transport (Figure 2.3 step 2 and 3 and Figure 2.4.a). A variant is inserting a nanotube at the tip of a micropipette which has been used for direct flow measurements (Figure 2.4.a) [31]. The nanotube length can be measured *in situ* with the SEM.

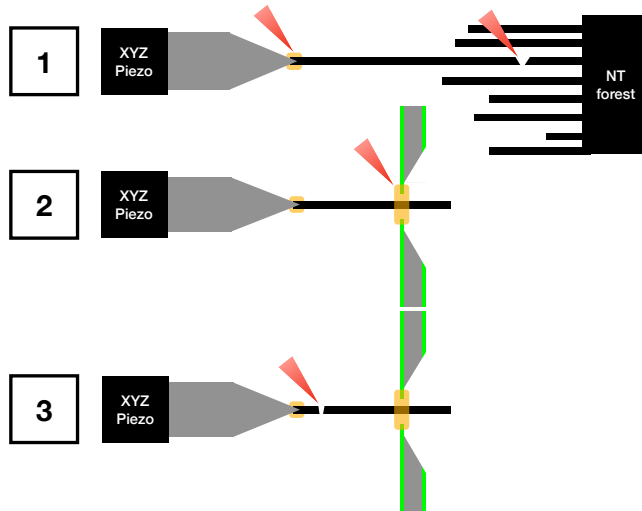


Figure 2.3

Single transmembrane nanotube setup fabrication inside a SEM. Step 1: Picking the nanotube. A tungsten tip linked to a piezo manipulator with nanometric resolution is approached to a commercial nanotube forest. The tip is glued to a single nanotube by introducing naphthalene into the chamber which reticulates under electron beam exposure (naphthalene in transparent orange). The single nanotube is then cut from the forest using EBIE. **Step 2:** the insertion. The nanotube is carefully inserted inside a SiN window or a glass pipette tip (not drawn) and sealed using naphthalene. **Step 3:** Retracting the tip. The nanotube is cut from the tip using EBIE. A variant presented in [57] is simply retracting the tip which induces telescopic retraction of the CNT inter walls.

This setup has been used mostly for the fundamental study of interfaces. At low salt concentration, the conductance of boron nitride nanotubes (BNNT) saturates [57] while it scales as $C_s^{1/3}$ (C_s being here the salt concentration) for the carbon nanotubes (CNT) [58]. This points to a high surface charge in BNNTs independent of the salt concentration while CNTs exhibit lower and salt concentration dependent surface charge. Such a salt concentration dependent surface charge mechanism is referred to a surface charge regulation. pH measurements also indicated that surface charge is fixed on BNNTs but mobile in CNTs. Charge mobilities and regulation are further discussed in chapter 5. A striking results obtained in 2016 by Secci et al. is the direct measurement of very large slip length in narrow CNTs while the BNNTs exhibit neglectable slippage (Figure 2.4.b) [31]. Both materials having the same crystallographic structure this points to subtle water/carbon interactions that were still awaiting for explanation until very recently. Kavokine et al. provided first bricks of explanation regarding the remarkable low carbon water/carbon friction by

showing that it is related to quantum effects [33]. Slippage and its consequence on fluidic and ionic transport are further discussed in chapters 5 and 7. Giant slippage was proposed as a prerequisite for observing mechano-sensitive behavior in narrow CNTs (Figure 2.4.c) [32]. According to the authors, the pressure-current response shares similarities with the one displayed by some biological channels. Finally the BNNTs nanotubes made the first demonstration of the great possibilities offered by nanomaterials for osmotic energy harvesting owing to their large surface charge [57]. This will be further discussed in the chapter 6.

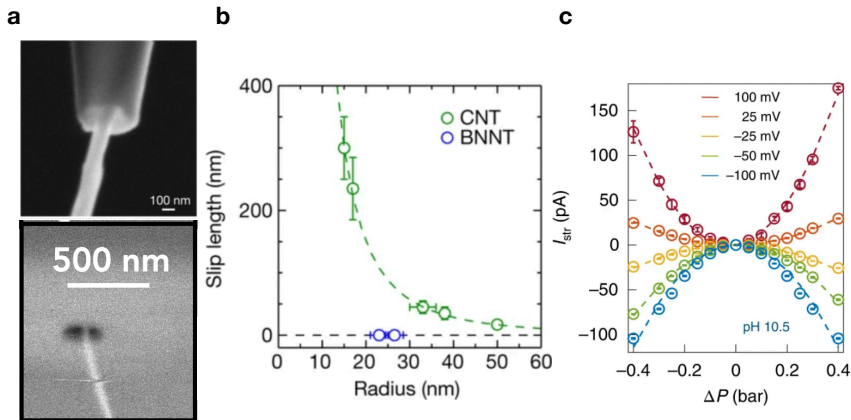


Figure 2.4

Nanofluidics with single transmembrane nanotubes. **a**, SEM image of a nanotube inserted in a pipette (top, from [31]) and in a SiN membrane (bottom, from [32]). **b**, Slip length vs nanotube radius for CNTs and BNNTs, from [31]. The pipette tip with the glued nanotube is submerged into a water bath with colloidal suspension. A pressure drop inside the nanotube is induced by connecting the pipette base to a pump. The colloid motion in the vicinity of the nanotube exit is analyzed using Landau-Squire jet theory which enables to extract the material slip length. **c**, Current induced by pressure (streaming current) vs applied pressure drop for various additional voltage drops inside a narrow CNT, from [32]. A non-usual quadratic dependance of the streaming current with the applied pressure is observed as well as a strong gating effect with the potential. This is equivalent to a modulation of the conductance with the applied pressure defining mechano-sensitivity.

Single transmembrane nanotube setup has proven to be a great tool for the fundamental exploration of interfaces. However it suffers from a few limitations. As the nanotube is picked up from a commercial forest and because of the presence of inner walls, its dimension cannot be tuned with a precision lower than a few nanometers. Also, the signal becomes small for very narrow nanotubes which can make the measurements difficult. Finally, even if as stated before, having one single pore is crucial for accurate characterization, a device where the number of pores can be precisely chosen is always better, for some applications at least. All those limitations were overcome by the development of the angstromslits.

2.3 Pristine carbon nanochannels (Angstroslits): 2D, the inspiring technology

2D nanofluidics channels have been fabricated for two decades using conventional techniques [59]. In 2016, the fabrication of nanofluidics channels relying on Van der Waals assembly and e-beam lithography/RIE represented a major technological advance (Figure 2.5) [23]. The confinement in such channels is fixed by the thickness of an array of graphite ribbons (spacer layer) separating two other crystals (Figure 2.6.a). It can therefore be as high as 3.4 Å (one graphene layer) and controlled with atomic scale precision. The channels length can also be chosen between 500 nm to 10 micrometers or more with a precision of 500 nm given by the resolution of the micromanipulators during the top-layer transfer. Their width can be controlled with an accuracy of a few tens of nanometer with a well controlled lithography. The number of channel can be chosen (technically between 1 and 200). The material can be chosen from a vast library of 2D materials (it has to be transferable and stable in air).

This nanofluidics device is therefore, in my opinion, the ultimate platform in term of confinement and versatility. In only five years it enabled an impressive number of publications [23–27, 60–62]. Here a non-exhaustive list of results is provided to illustrate how the angstroslit’s versatility in fabrication promoted fundamental discoveries. In 2016, R. Boya et al. presented the device and water permeation experiments in channels of thickness varied with atom-scale resolution [23]. The authors find that the permeation rate has a non-monotonic behavior with the number of layers reaching a maximum for devices having spacers with four atomic layers (Figure 2.6.b). The authors interpret this results as the balance between disjoining pressure (dominating at high confinement) and increase in cross-section area (dominating for low confinement). Esfandiar et al. studied ion transport in angstroslits with $N=2$ layers of graphene spacers, corresponding to a confinement of 6.7 Å [27]. They find that ion with hydrated diameter larger than this confinement level can still move through the slits, yet with a decreased mobility (Figure 2.6.c). The authors interpret this results as a squeezing of the ions’ hydration shell resulting in a reduced ionic mobility because of higher hydration energy costs. Finally the angstroslits, as opposite to atom-thick nanopores or nanotubes, can be used to study the fundamental properties of confined static fluids. Fumagalli et al. used atomic force microscopy to measure the out-of-plane dielectric constant of highly confined water film of varying thickness [25]. They find that it strongly decreases with decreasing film thickness and rationalize the results in term of balance between bulk and interfacial water contributions. The latest has a lower dielectric constant because of reorganization of water molecules at the interface. This result can have strong consequences for ionic transport as electrostatic interactions scale as $1/\epsilon$.

The only drawback with this system might be the difficulty in fabrication coming from a high number of steps involved all having a non-zero probability of failure. One of the major challenge being to find a spacer crystal large, thin and homogeneous enough. The initial goal of the PhD was therefore to develop a new system similar and a little bit easier to fabricate in order to be able to produce and study a reasonable number of devices within 3 years.

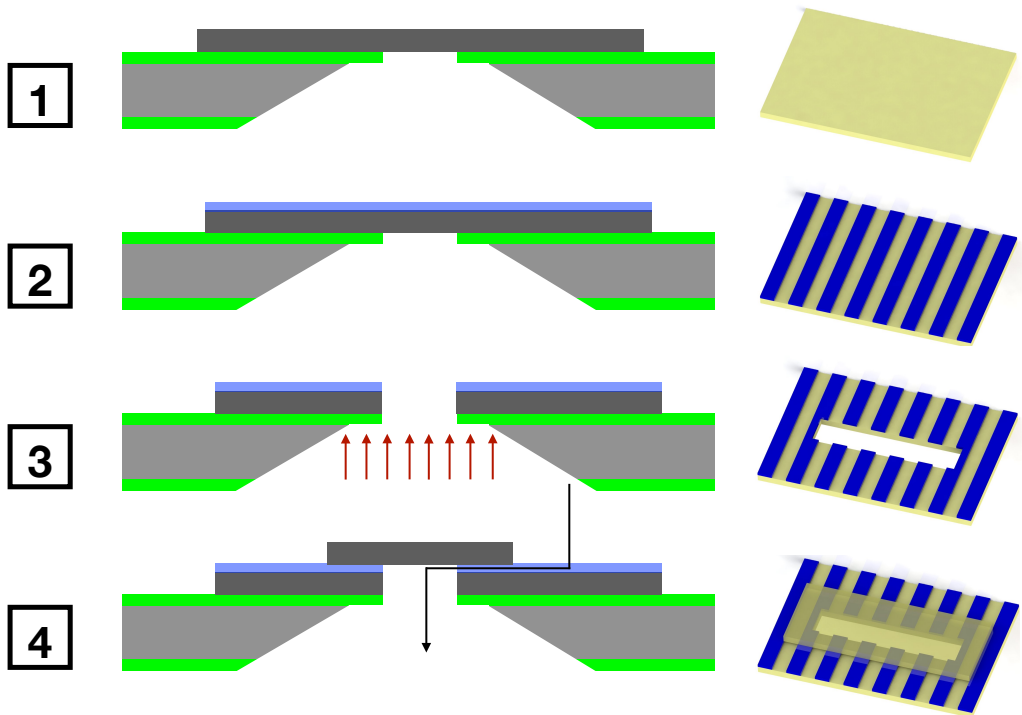
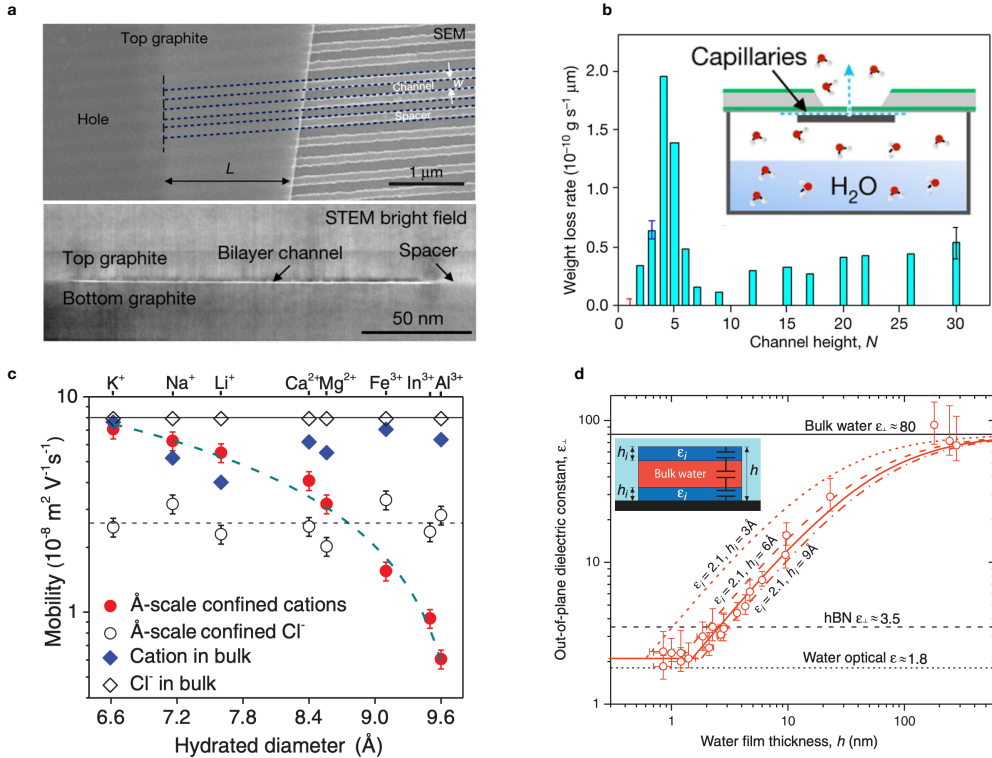


Figure 2.5

Angstroslits nanofabrication : 2D view (left) and 3D schematic without the SiN window (right). **Step 1:** Bottom layer transfer. A bottom crystal of a chosen material (in dark grey (2D)/yellow (3D)) is transferred above a rectangular aperture (of roughly 20x3 microns) on an SiN window. **Step 2:** Spacer transfer. The spacers (in blue) are made using a thin crystal (its thickness can be known with atomic scale precision) patterned in an array of nanoribbons by electron beam lithography followed by reactive ion etching. **Step 3:** Piercing of bottom layer and spacer. This is made using RIE by flipping the device and exposing the device from the back, using the SiN window as a mask. **Step 4:** Top layer transfer. A top layer crystal is transferred (in dark grey (2D)/transparent yellow (3D)) above the aperture and a fraction of the spacer. The channels are made of the covered vacuum space left between the spacers. The fluidic path is indicated by the black arrow.


Figure 2.6

Nanofluidics to angstrofluidics with angstromslits. **a**, Images of angstromslits, from [23]. Top: SEM top view of a trilayer device (h ~ 1.1 nm) microscopy. The image is taken at the top layer edge. The hole in bottom layer and spacers is visible on the image left. Here the channels have therefore a length of 1-2 microns. Bottom: TEM side view of a bilayer channel. **b**, Water permeation vs number of atomic layer of the spacer (defining the channel height/confinement), from [23]. The devices are made of graphite. A container filled with water is sealed with a device (inset). The water evaporates through the channels in a liquid state because of capillary condensation. The system mass is recorded in real time to extract the weight loss rate. **c**, Mobility (electrophoretic) vs ion's hydrated diameter in bilayer (6.7 Å) graphitic channels, from [27]. The mobility is determined from concentration drop experiments (one reservoir is filled with a 10mM solution and the other 100mM) and conductivity measurements at 100mM, using the Henderson equation. The decreased in Cl⁻ mobility in slits relative to the bulk's value is interpreted by the authors as increased friction with the walls that does not occur with cations because of a reversed polarization of the hydration's shell. **d**, Out-of-plane dielectric constant vs water film's thickness in hexagonal boron nitride water channels, from [25]. The dielectric constant is measured with an AFM tip above the device kept in dry nitrogen atmosphere. The channels are filled from below. The dashed and solid lines are theoretical predictions using a model of capacitor in series corresponding to interfacial and bulk water (inset). The fitting parameters are the dielectric constant (ϵ_i) and thickness (h_i) of the interfacial water film. When $h < 2h_i$, the bulk water layer vanishes and the dielectric constant is constant. When $h \gg 2h_i$ the interfacial layer is negligible.

Development of a new technology: activated carbon nanochannels

Taking inspiration from the angstromslits [23] we developed the protocol described in this chapter. In particular the patterning technique is different as we use EBIE instead of EBL+RIE. The assembly order is also different as the transfer above the SiN window is here the final step.

3.1 Process-flow

After mechanical exfoliation of graphite crystals on a Si/SiO₂ substrate, we patterned the chosen crystal using Electron Beam Induced Etching (EBIE) in a low water vapor atmosphere. The pattern consist of a through hole and one/a few channels (Figure 3.1, step 1). The pattern is then covered by a top layer graphite crystal using the dry transfer technique (Figure 3.1, step 2). Finally, this bi-layer heterostructure is wet-transferred onto a commercial (*Norcada*) pierced Si/SiN window (Figure 3.1, step 3).

3.2 Step 1: Patterning

First, we exfoliated natural graphite on Si/SiO₂ substrates (oxide thickness of 280 nm) to obtain graphite flakes of thickness between 50 and 200 nm. We selected a flake with clean and flat area of suitable size (30 μm \times 30 μm or above) as bottom layer using optical microscopy. Then, the nanochannel formation is carried out on the chosen bottom layer graphite crystal using electron beam induced etching (EBIE) [63, 64] in an environmental scanning electron microscope (FEI NOVA NanoSEM) working at a low pressure (0.1-0.2 mbar) water vapour ambience. For making nanochannel, first a through hole of 300 nm diameter is drilled by focusing the beam at a single spot. Then, the hole is enlarged into a square aperture by scanning a 1 μm \times 1 μm window (centering the hole) repeatedly. Finally, the

This part of the thesis was done with the help of Vasu Kalangui and Aurélie Pierret who trained me for exfoliations and transfers. I also want to acknowledge José Palomo and Michael Rosticher for their precious advices concerning exfoliations and transfers. The EBIE patterning was developed with the help of Antoine Nigues. For someone intending to fabricate activated carbon's nanochannel, a full protocol is given in appendix A.

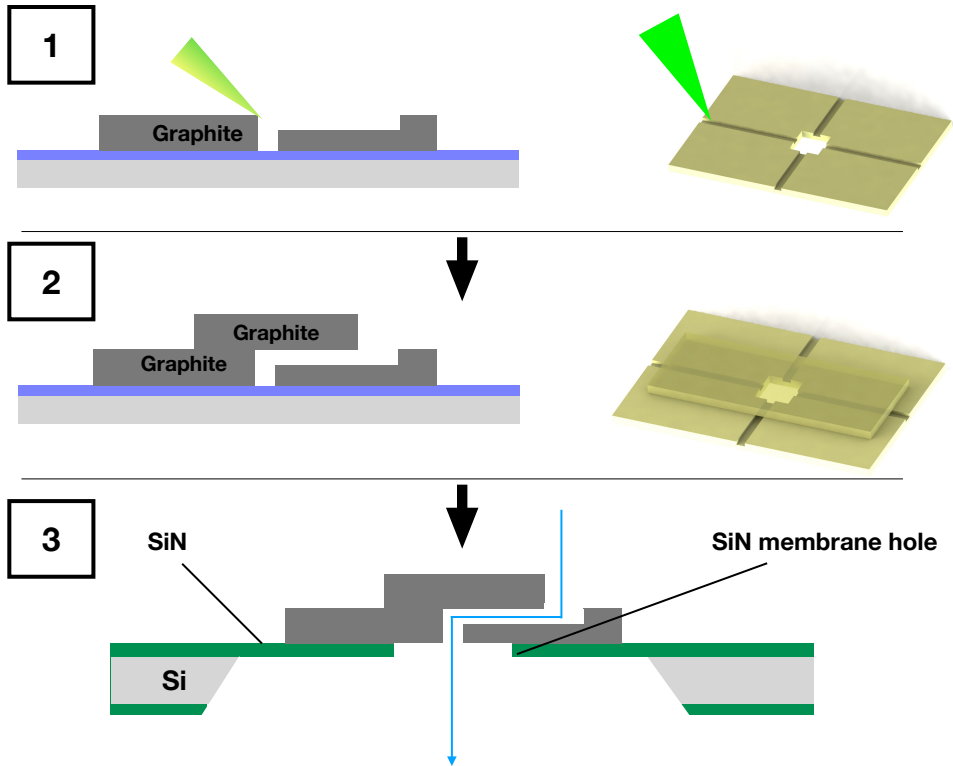


Figure 3.1

Activated channels nanofabrication process flow. **Step 1:** Patterning of the graphite bottom layer on a Si/SiO₂ substrate. Left: schematic. The Si is light grey and the SiO₂ is purple and the bottom layer graphite is grey. Right: 3D schematic of the bottom layer during patterning. **Step 2:** Dry transfer of the top layer above the pattern. Left: Schematic. The top layer is indicated in grey as well. Right: 3D schematic of the bilayer heterostructure after the top layer transfer. **Step 3:** Wet transfer of the heterostructure on the pierced SiN membrane. The membrane is indicated in grey/green. It has a circular aperture (with a diameter of 10 microns) in its center inside which the bottom layer's hole has to land. The blue arrow indicates the fluidic path.

nanochannel of desired channel height is made by single line scan connecting the square aperture's center (Figure 3.2.a-a'). The operation is repeated by rotating the window (Figure 3.2.b-b') or shifting the beam (Figure 3.2.c-c') to obtain multi-channel devices.

3.3 Step 2: Top layer Dry Transfer

A top layer graphite flake of suitable size (20x20 μm or above) and thickness (50 to 100 nm) is carefully transferred onto the activated nanochannel patterned bottom layer, using a glass slide with polypropylene carbonate (PPC) coated polydimethylsiloxane (PDMS) with a droplet shape. After transferring the top layer,

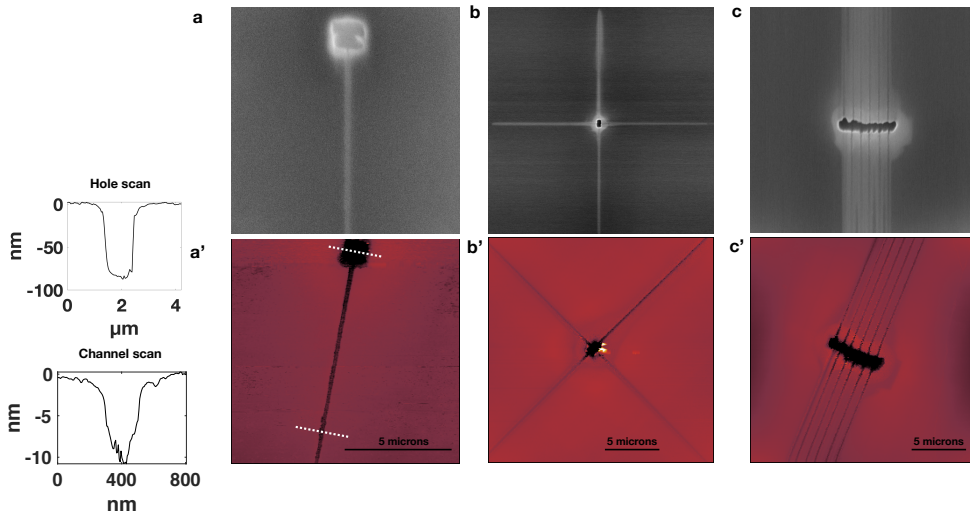


Figure 3.2

Patterning. **a**, SEM and **a'**, AFM images with profile of a single channel pattern. **b-b'**, View of a multichannel ($N=4$) pattern with perpendicular channels. **c-c'**, View of a multichannel ($N=12$) pattern with parallel channels.

the graphite-graphite heterostructure is immediately cleaned using acetone for 3 hours followed by isopropanol (1 hour) cleaning. Figure 3 displays images of devices after step 2.

3.4 Step 3: Bi-layer heterostructure wet transfer on pierced SiN window

Subsequently, the fluidic device is made by wet transfer of this heterostructure with activated nanochannel onto a silicon nitride membrane with circular opening (10 μm diameter). After step 2, the Si/SiO₂ substrate is covered with a 550 nm PMMA film by spin-coating. It is then submerged in a KOH solution (10-30 w%) overnight. The KOH etches the SiO₂ until the PMMA film with the heterostructure detaches. The PMMA layer is carefully collected and washed twice in DI water before being placed on the SiN window. Our micromanipulator provides a sub-micron resolution in lateral and axial motion to precisely align the square aperture (1 $\mu\text{m} \times 1 \mu\text{m}$) in bottom layer graphite onto the circular opening in silicon nitride membrane. To remove PMMA, the fluidic device is cleaned using acetone for 24 hours followed by isopropanol (one hour) cleaning. Finally, the device is annealed in argon/hydrogen atmosphere at 400°C for 4 hours to remove any residual contamination and obtain improved adhesion between top and bottom layer graphite crystals. Figure 3.4 displays images of devices after step 3. Overall wet transferred is preferred for transferring precious crystals or heterostructures that have already been processed. It is heavier and harder than dry transfer but has a higher success rate when properly mastered. This is why dry transfer is used for step 2 as the top layer is a pristine

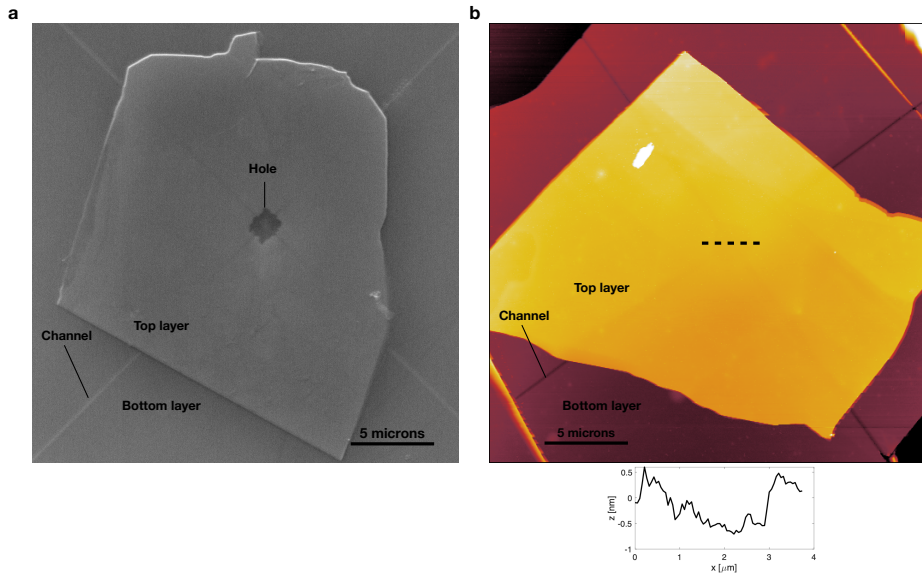


Figure 3.3

Top layer transfer. **a**, SEM image of a bilayer heterostructure after the top layer-transfer. Channels are visible in white. **b**, AFM image of another device at the same stage. Channels are visible in black. Profile above hole shows limited sagging as a sign of good interlayer contact.

crystal that can be easily replaced in case of failure. For step 3, wet transferred is chosen to minimize the chance of losing the device.

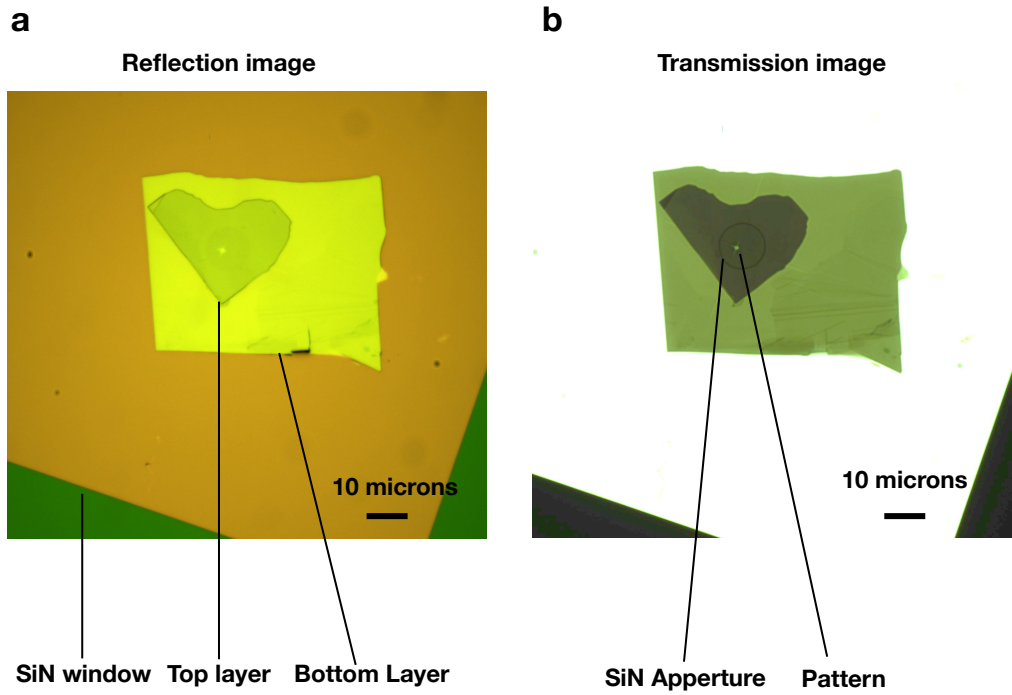


Figure 3.4

Wet transfer on SiN window (finished device) a, Bright field reflection optical microscopy image of a finished device and **b**, Transmission optical microscopy of the same device.

Part II

Enhanced ionic transport and osmotic (blue) energy harvesting

Theory: ionic transport in slippery nanofluidic channels

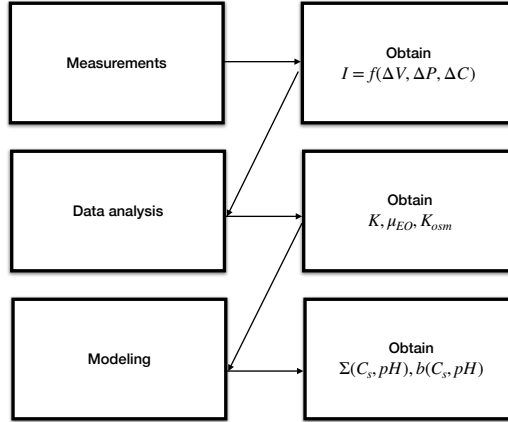
Having developed a novel nanochannel, it is important to characterize it thoroughly. This can be done by using classical characterization technique, described in chapter 6, as well as nanofluidic ones. The goal of nanofluidic characterization is to rationalize ionic transport by extracting the channel's interfacial properties through electrokinetic measurements coupled with appropriate modeling. In this chapter we start by providing theoretical tools to understand this modeling process such as nanofluidics governing equations as well as qualitative and mathematical descriptions of pristine and activated carbon interfaces. Secondly, we explain in more details the model used in chapter 6 to extract pristine and activated nanochannels' surface properties. Lastly we explain diffusio-osmosis, the physical mechanism driving osmotic power generation in activated channels.

4.1 Procedure

The study of ionic transport in nanofluidics allows to characterize materials by extracting their surface properties: surface charge, $\Sigma(C_s, pH)$ and slip length, $b(C_s, pH)$ as illustrated in Figure 4.1. C_s is the salt concentration here. Ionic transport is induced by various forcing such as voltage drop, ΔV and pressure drop, ΔP and concentration drop, ΔC . The resulting ionic current, I is measured (using Ag/AgCl electrodes in our case). This enables to obtain the following characteristic transport quantities: Conductivity defined as $K = I/\Delta V \times l/A$, electro-osmotic mobility defined as $\mu_{eo} = I/\Delta P \times l/A$ and osmotic mobility defined as $K_{osm} = I/\Delta \log(C_s) \times l/A$. Here l is the channel length and A its cross-section area. Finally, theoretical models obtained from nanofluidics' governing equations containing materials' surface properties as ingredients are compared with experimentally obtained values to extract the materials' surface properties.

4.2 Governing equations

General equations governing nanofluidics transport are the same as the ones for micro and even meter-scale confinement. This set of *local* equations is supposed to hold down to confinement of 1 nm [2]. However the boundary conditions of

**Figure 4.1****Process for material characterization**

this set of equations, containing the surface properties, have major consequences for nanoscale confinement only. This can be easily understood because interfacial phenomena, which are a direct consequence of surface charge and slippage, have a range of maximum 100 nm away from the interface [1, 2]. Hence for confinement much greater than 100 nm such phenomena are negligible and cannot be probed experimentally (by studying confined flow). The mathematical description of such boundary conditions and their relevance for a given confinement lengthscale will be further discussed in the next section.

The fluid flow is described by the Stokes equation where the inertia have been neglected, Reynolds number being much smaller than one in nanofluidics systems [1]:

$$\eta \Delta \mathbf{v} + \mathbf{f} = \nabla p \quad (4.1)$$

with η the dynamic viscosity, \mathbf{v} the velocity profile, \mathbf{f} a body force and p , the pressure.

Convective-diffusive dynamics of ions, for a monovalent salt, is given by the following Smoluchowski equation [1]:

$$\frac{\delta \rho_{\pm}}{\delta t} = -\nabla \cdot (-D \nabla \rho_{\pm} \mp \frac{eD}{k_b T} (\nabla \phi) \rho_{\pm} + v \rho_{\pm}) \quad (4.2)$$

where ρ_+ is the density of negative ions, ρ_- is the density of positive ions, t is the time, D is the diffusion coefficient, e is the electric constant, k_b is the Boltzmann constant, T is the temperature, ϕ is the electrostatic potential and v is the fluid velocity.

Neglecting eventual correlations between the ions, the electrostatic potential can be

expressed using Poisson equation [1]:

$$\Delta\phi = -e\frac{\rho_+ - \rho_-}{\epsilon} \quad (4.3)$$

With ϵ the dielectric permittivity of water.

The Stokes equation, for the case of an electrolytic solutions can be written as [1]:

$$\eta\Delta\mathbf{v} - e(\rho_+ - \rho_-)\nabla\phi = \nabla p \quad (4.4)$$

4.3 Surface properties

4.3.1 Surface charge

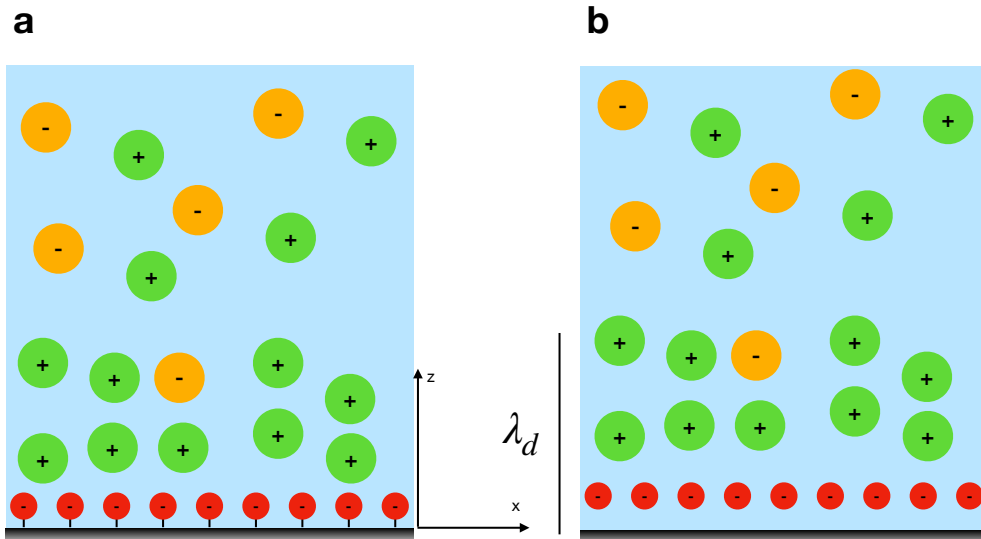
Once submerged in water most interfaces and in particular nanomaterials' have a non neutral (negative) surface charge. Two different kind of charging mechanisms (or electrifications) can occur depending on the material's chemistry. On hexagonal Boron Nitride (h-BN) [57, 65] or activated carbon nanochannels (see chapter 6) negatively charged species, such as hydroxide ions or carboxylic acid(-COOH) respectively, can be attached to the surface via a covalent bond (with length of roughly 1.5 Å [65]). This charging mechanism is named chemisorption because of the because of the established covalent bonding between the charged species and the material (Fig 4.2.a). The charges in this configuration are fixed. For carbon nanotubes (CNT) [58] or pristine graphite interfaces (see chapter 6), a different charging mechanism occurs. Because of a potential well 3.3 Å away from the interface hydroxide ions tends to migrate toward the walls [65]. Such a charging mechanism is refer to as physisorption and in that case the charges are mobile (Fig 4.2.b). Yet their mobility is supposed to be lower than water molecules or other ions in the solution (see chapter 6). The surface charge's scaling with the solution's pH is related to the chemistry of the interface. It is exponentially increasing for h-BN nanotubes at basic pH [57] and scales as $10^{pH/3}$ for carbon nanotubes [58]. It is decreasing at acidic pH for the case of activated carbon nanochannels (see chapter 6-Appendix C). Surface charge can also depend on the electrolyte concentration, mostly in carbon-based materials [58]. Such a mechanism is called charge-regulation behaviour.

Surface charge induces the formation of the so-called, electrical double layer (EDL) or Debye layer. Positive ions in the solution, called counter-ions, screen the surface over a distance λ_D , known as the Debye length (Fig 4.2) [1, 2].

Assuming that there is no fluid-flow, from Eq 4.2, the ionic flux can be rewritten as :

$$j_{\pm} = -D\nabla\rho_{\pm} \mp \frac{eD}{k_bT}(\nabla\phi)\rho_{\pm} \quad (4.5)$$

This Nernst-Planck equation, along with the Poisson equation and the Stokes equation constitute to Poisson-Nernst-Planck-Stokes (**PNPS**) framework widely used in nanofluidics. Assuming steady-state, with a mean field approximation and integrating along the z direction (perpendicular to the surface) with equal concentrations of cations and anions in the bulk ($\rho_+ = \rho_- = \rho_s$ and $\phi = 0$ for $z > \lambda_D$); one can find

**Figure 4.2**

Electrification of interfaces in water. **a**, Interface with chemisorbed species represented in red. The chemical bonds are represented as black lines. Anions are green and cations are represented in orange. **b**, Interface with physisorbed species.

the Boltzmann distribution, for the case of a monovalent salt :

$$\rho_{\pm} = \rho_s e^{\frac{\mp e \phi}{k_b T}} \quad (4.6)$$

Combining it with the Poisson equation yields the Poisson-Boltzmann equation :

$$\Delta \phi - \lambda_D^{-2} \phi = 0 \quad (4.7)$$

With $\lambda_D = \left(\frac{\rho_s e^2}{2 \epsilon k_b T} \right)^{-1/2}$ being the characteristic length over which the surface potential vanishes, the Debye length. It is dependent on the salt density (concentration), ρ_s .

We make the following simplified calculation to demonstrate the necessity of nanoscale confinement to be able to measure interfacial effects. Lets assume a channel of confinement h , width w , and length $L \gg h$ with a fixed surface charge Σ . We assume no concentration gradient along the channel ($\nabla_x \rho_{\pm} = 0$). We neglect any fluid flow effect on ion motion. Lets assume an applied electric field E along the channel ($-\nabla \phi_x = E$). The electrophoretic contribution to the electric current writes [1]:

$$I_{ep} = w \int_0^h dz (j_+ - j_-) = w \frac{e^2 D}{k_B T} \int_0^h dz (\rho_+ + \rho_-) E \quad (4.8)$$

In the limit of a "large pipe" $h \gg \lambda_D$:

$$I_{ep} = w \frac{e^2 D}{k_B T} \left(\int_0^{\lambda_D} dz (\rho_+ + \rho_-) E + \int_{\lambda_D}^h dz (\rho_+ + \rho_-) E \right) \quad (4.9)$$

Here the first term between the bracket being the charges in the bulk (outside of the Debye layer) and the second one being the charges in the Debye layer that screens the surface charge. It can be rewritten as :

$$I_{\text{ep}} = 2\rho_s h w \frac{e^2 D}{k_B T} E \left(1 + \frac{\Sigma/e}{\rho_s h}\right) \quad (4.10)$$

The electrophoretic's contribution to the conductance writes:

$$K_{\text{ep}} = \frac{I_{\text{ep}}}{E} = 2\rho_s h w \frac{e^2 D}{k_B T} \left(1 + \frac{\Sigma/e}{\rho_s h}\right) \quad (4.11)$$

For the limit of large h , $\Sigma \ll \rho_s h$ and the electrophoretic current is no longer sensitive to the surface charge. Hence the bulk contribution to the current or to its fluctuations (thermal noise) does impede measurements of interfacial phenomena in large channels (with $h \gg 100$ nm). The Dukhin number is defined as $Du = \frac{\Sigma}{\rho_s h}$. For $Du > 1$, interfacial electrostatic effects become significant.

4.3.2 Hydrodynamic slippage

Usually, as a boundary condition to solve Stokes equation, the tangential velocity at the wall is supposed to vanish (Figure 4.3.a). However a more general expression can be obtained by balancing the viscous stress with the solid/liquid friction to obtain the more general Navier's partial slip boundary condition [1]:

$$v_x = b \frac{\partial v_x}{\partial z} \Big|_{\text{wall}} \quad (4.12)$$

With v_x the interfacial slip velocity and $b = \frac{\eta}{\lambda}$ the slip length that depends on the interface chemistry and topography. Here λ is a liquid/solid friction coefficient. The interfacial velocity v_x is added to the whole velocity profile (Figure 4.3.b). Solving the Stokes equation, negelection body forces, for a channel of length L , width w and height h yields :

$$Q = \frac{w \Delta P}{12 \mu L} h^3 \left(\frac{6b}{h} + 1\right) \quad (4.13)$$

With Q the water flux and ΔP the pressure difference in the x direction. Analogously to the Dukhin number, if $6b \ll h$, the slippage can be neglected and b can be approximated to 0.

However it is not the case in some nanochannels and slippage can enhance significantly the water flow, in particular for those made of carbon based-materials. Slip lengths of up to 100 nm have been extracted in graphene 2D nanochannels [66] and up to 300 nm in narrow CNT's [31].

4.3.3 Combined effects

As stated above, ion and water transport in the vicinity of an interface is largely controlled by surface charge and hydrodynamic slippage; in particular for the case of osmotic energy harvesting relying in the Diffusio-osmosis(DO) mechanism, which is the one of interest in this work. DO is the generation of a water flux in the

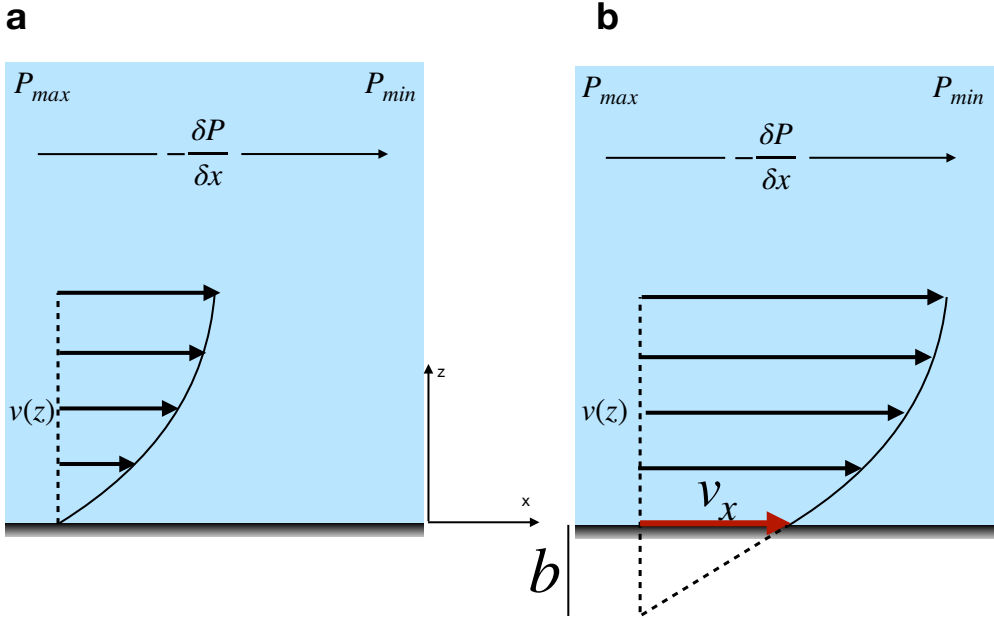


Figure 4.3

Illustration of hydrodynamic slippage. **a.**, Velocity profile in the vicinity of a Slip-free interface in the presence of a pressure gradient. **b.**, Velocity profile in the vicinity of an interface with hydrodynamic slippage pressure gradient. The interfacial velocity v_x is represented in red, the vertical solid black line indicates the slip length.

vicinity of a charged interface. Therefore, it is critical to maximize the surface charge (driving force) and minimize the liquid/solid friction (dissipating force) in order to obtain the best energy harvesting performances. A mathematical definition of this mechanism is given in the a following section. However surface charge and slippage are not necessarily independent from each other and coupling between both effects have been the object of a few studies.

Mouterde et al. showed that mobility of the surface charges can reduce the effective slip length because of the friction of physisorbed hydroxide ions with the neighboring wall or water molecules [67]. An effective slip length for surfaces with mobile charge, such as pristine carbon, can thus be written :

$$b_{eff} = \frac{b_0}{1 + \beta_s \times \Sigma_n} \quad (4.14)$$

With b_0 the material's slip length without mobile charge, $\beta_s = \frac{1}{\lambda} \frac{\lambda_s \lambda_w}{\lambda_s + \lambda_w}$, λ_s being the hydroxide ion/wall friction coefficient, λ_w being the hydroxide ion/water friction coefficient and $\Sigma_n = -\Sigma/e$ is the normalized surface charge.

Furthermore, it was recently shown by molecular dynamics (MD) simulations that the charge repartition on the interface may have a dramatic impact on the interplay between surface charge and hydrodynamic slippage [68]. The authors showed that hydrodynamic slippage (slip length) is independent of the surface charge on ho-

mogeneously charged surface (without chemisorbed charged groups), but strongly decreases with the surface charge on heterogeneously charged surface, such as activated carbon. The authors state that this difference may be explained through binding of counter-ions with charged groups thus increasing the water solid/friction. Such binding being less likely for the case of uniformly charged interfaces. However in this study the authors neglected the effect of mobile charge and assumed a spatial repartition of the charge similar to the one of carbon atoms for homogeneously charged surfaces.

Therefore the choice of fixed or mobile charge to maximize nanofluidic transport, and in particular osmotic energy harvesting, remained open at the start of this work. The experimental results obtained on activated carbon presented in chapter 6 show that in practice fixed charge on a carbonaceous slippery interface is a good configuration for efficient transport.

4.4 Transport quantities

Here, we provide theoretical elements of understanding regarding ionic transport induced by a voltage drop, pressure drop or concentration drop in the vicinity of slippery interfaces with mobile and fixed charge. Refer to [8, 67] for the complete derivations. We assume a slit-like geometry of moderate confinement which is the one of interest in this thesis. Hence we have $\lambda_D < h < w < l$. Where l is the channel length with w the channel's width and h its height corresponding to the confinement.

4.4.1 Conductivity (Motion induced by voltage drop)

As stated above, the conductivity can be obtained from experiments, knowing the channel's dimension, using the following formula:

$$K = \frac{l}{A} \times \frac{I}{\Delta V} \quad (4.15)$$

I is the measured current, ΔV is the applied voltage and $A = w \times l$ is the channel's cross section. The application of such an external voltage results in the generation of an electro-osmotic flow [8]. Electro-osmosis is an interfacial phenomena occurring in the vicinity of a charged interface in the presence of an electric field tangential to the interface (Figure 4.4). In the bulk, the momentum transfer of cations to the water molecules is compensated by anions going in the opposite direction. But in the Debye layer, as there is a higher number of counter ions (cations) to compensate the surface charge, a net water flux arises which drag the non-neutral Debye layer. Hence, the electro-osmotic contribution to the ion motion has to be added to the electro-phoretic (voltage induced) one.

Regardless of the interface, the bulk contribution to the conductivity writes :

$$K_{bulk} = 2\mu e^2 C_\infty \quad (4.16)$$

With $\mu = \mu_+ = \mu_-$ the potassium(+) or chloride(-) mobility (electrophoretic) and C_∞ the salt concentration in the bulk. In the bulk, electro-osmotic flow has no

influence on the conductivity (for KCl) because anions and cations having the same mobility are equally moved in the electric field's direction hence canceling each other.

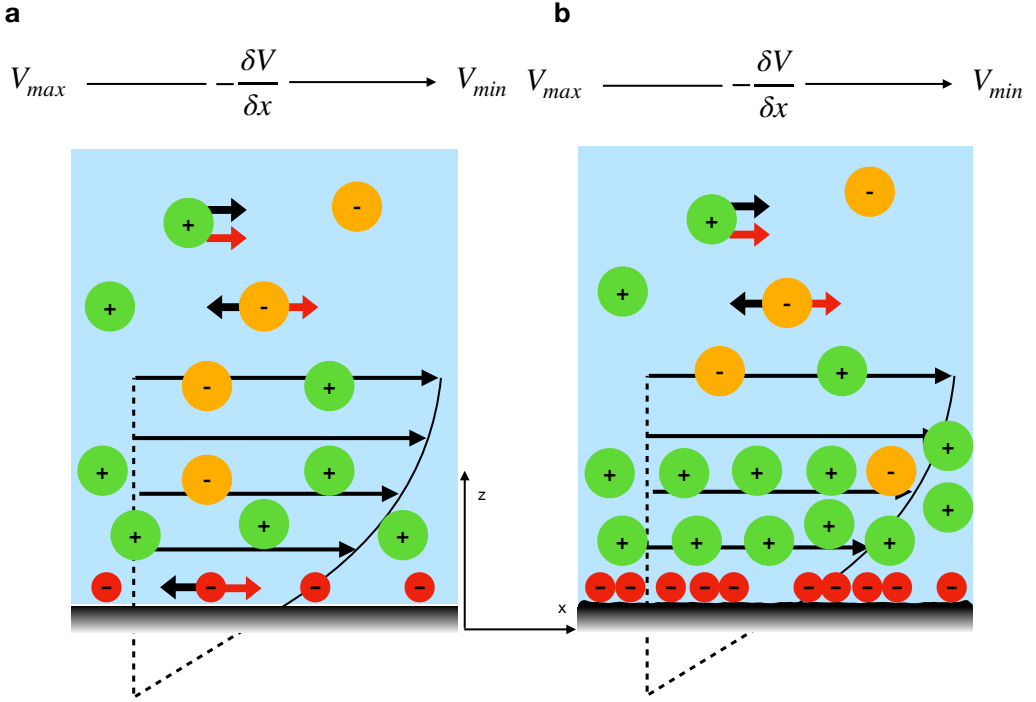


Figure 4.4

Ionic motion induced by voltage drop on slippery surfaces with different electrifications. a, Surface with mobile charge, such as pristine carbon. Black arrow represent electrophoretic contributions and red arrow are electroosmotic contributions. **b,** Surface with fixed charges, such as activated carbon.

The surface contribution can be separated in a 'no slip' term that does not take slippage into account and a 'slip term' that takes the contribution of the slippage to the conductance only. The 'no slip' term can be written as [67]:

$$K_{\text{surf,no-slip}} = \frac{1}{h} \left[\mu e |\Sigma| (1 + \delta) \times \frac{\chi}{\sqrt{1 + \chi^2 + 1}} \right] \quad (4.17)$$

With

$$\chi = 2\pi\lambda_D\ell_B \frac{|\Sigma|}{e} = \sinh\left[\frac{-e\Psi_0}{2k_B T}\right] \quad (4.18)$$

where $\ell_B = e^2/4\pi\epsilon k_B T$ is the Bjerrum length and $\Psi_0 = \lambda_D\Sigma/\epsilon$ is the surface potential. Here $\delta = 1/(2\pi\ell_B\mu\eta)$ is a parameter taking into account the contribution of the electro-osmotic flow, resulting from the advection-driven dragging of the non neutral Debye layer.

We now add the contribution of slippage to the surface conductivity. Let's start by the more complicated case where mobile charges are present (Figure 4.4.a), such as

pristine graphite and CNT. Accordingly to [67] it can be written as:

$$K_{\text{surf,slip,mobile}} = \frac{1}{h} \left[\frac{b_0}{\eta} \times \frac{(1 - \alpha_{ion})^2 \Sigma^2}{1 + \beta_s \times \frac{|\Sigma|}{e} \ell_B^2} + e\mu_m |\Sigma| \right] \quad (4.19)$$

With $\alpha_{ion} = \frac{\lambda_s}{\lambda_s + \lambda_w}$ and μ_m the hydroxide ion electrophoretic mobility. Here the first term is the enhancement of the electroosmotic contribution to the Debye layer motion corrected by the electro-osmotic contribution to the hydroxide ion's motion. The second term is the electrophoretic contribution to the hydroxide ion's motion.

For the case of fixed charge (Figure 4.4.b) we have $\alpha_{ion} = \beta_s = 0$ and the electrophoretic contribution of hydroxide ion to the conductivity vanishes. Hence equation 4.19 can be rewritten as :

$$K_{\text{surf,slip,fixed}} = \frac{1}{h} \left[\frac{b_0}{\eta} \times \Sigma^2 \right] \quad (4.20)$$

The total conductivity is obtain by by summarizing these three contributions:

$$K_{\text{tot}} = K_{\text{bulk}} + K_{\text{surf,no-slip}} + K_{\text{surf,slip}} \quad (4.21)$$

One can see that the conductivity depends on the surface charge and slippage as well as friction parameters α_{ion} and β_s . The friction parameters have been obtained in [26] for the case of 7.2 Å slits and are not required for the case of fixed charge. Even with the reasonable assumption that those friction parameters should not vary too much in deeper slits or for the case of fixed charge there is still two unknown parameters: the slip length and the surface charge. Hence for the case of slippery and charged interfaces, conductivity measurements alone are not sufficient to extract surface's properties values (Σ and b). This is why other kinds of electrokinetic measurements such as electro-osmotic mobility are required to characterize those complex interfaces.

4.4.2 Electro-osmotic mobility (Motion induced by pressure drop)

The electro-osmotic mobility can be obtained from the experiment as :

$$\mu_{EO} = \frac{l}{A} \times \frac{I_{\text{stream}}}{\Delta P} \quad (4.22)$$

with I_{stream} the measured streaming current and ΔP the applied pressure drop. The application of a pressure drop across a nanochannels generates a water flow that will drag the non-neutral Debye layer (and eventual mobile charges) and this results in the generation of an ionic "streaming" current (Figure 4.5). The bulk is also dragged but as its net charge is zero, it does not contribute to the current. Thus streaming currents are favored by a combination of surface charge and slippage. According to [67] the electro-osmotic mobility for interfaces with mobile charge is defined as :

$$\mu_{EO,mobile} = - \left[\frac{\epsilon \Psi_0}{\eta} + \frac{b_0}{\eta} \times \frac{(1 - \alpha_{ion}) \Sigma}{1 + \beta_s \times \frac{|\Sigma|}{e} \ell_B^2} \right] \quad (4.23)$$

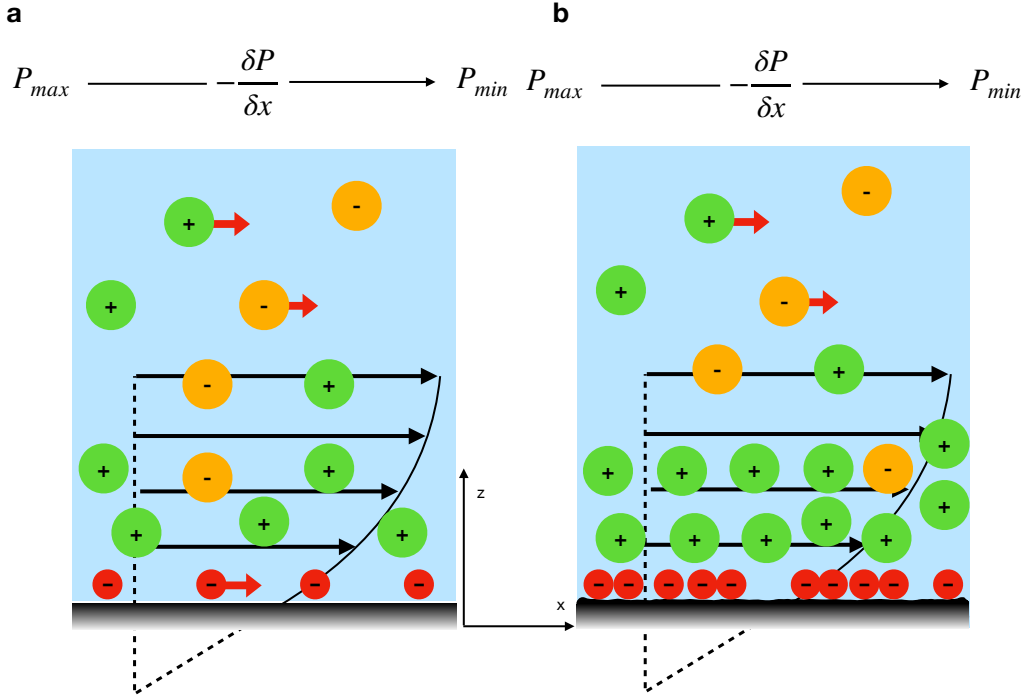


Figure 4.5

Ionic motion induced by pressure drop on slippery surfaces with different electrifications. a., Surface with mobile charge, such as pristine carbon. Red arrows represent the ion motion. **b.**, Surface with fixed charges, such as activated carbon.

The first term representing the no-slip contribution and the second one is the slippage contribution to the streaming current. The contribution of slippage is reduced by the mobility of the hydroxide ions (Figure 4.5.a). As a reminder even though the mobile charge and the Debye layer have an equal net absolute charge of opposite sign, they do not cancel each other because the hydroxide ions are less mobile than the counterions (otherwise the net streaming current would be 0). For the case of fixed charge (Figure 4.5.b) eq 4.23 reduces to:

$$\mu_{EO, fixed} = - \left[\frac{\epsilon \Psi_0}{\eta} + \frac{b_0}{\eta} \times \Sigma \right] \quad (4.24)$$

4.4.3 Osmotic coefficient (Motion induced by concentration drop)

The generation of an ionic current under the application of a concentration drop is related to the diffusio-osmosis phenomenon. Let's first start by considering a simple case where an interface without slippage interacts with a solute via an attractive potential $U(z)$ vanishing away from the interface (Figure 4.6). Let's also state that there is a solute gradient far away and parallel to the surface $\nabla_x C_\infty$. The solute concentration should obey a Boltzmann spatial distribution :

$$C_s(x, z) = C_\infty(x) e^{-\frac{U(z)}{k_b T}} \quad (4.25)$$

Projecting Stokes equation on z yields:

$$c\left(-\frac{\delta U}{\delta z}\right) - \frac{\delta p}{\delta z} = 0 \quad (4.26)$$

where p is the pressure. Here we assumed 0-normal velocity ($v_z = 0$). Integrating equation 4.26 and injecting equation 4.25 yields :

$$p(x, z) - p_\infty = k_b T c(x, z) - k_b T c_\infty \quad (4.27)$$

In the limit $\lim_{z \rightarrow +\infty} U(z) = 0$ we have $C_s = C_\infty$ and there is no pressure gradient in the z direction. This means that the pressure gradient arise only in the diffuse layer which is the Debye layer for the case of an electrolytic solution.

Equation 4.27 can be integrated in the Stokes equation projected in the x-direction :

$$\eta \frac{\delta^2 v_x}{\delta z^2} + \frac{\delta(p(x, z) - p_\infty)}{\delta x} = 0 \quad (4.28)$$

After integration this results in a bulk fluid velocity along x expressed as [8]:

$$v_\infty = \mu_{DO} (-k_b T \nabla_x C_\infty) \quad (4.29)$$

With $\mu_{DO} = \frac{1}{\eta} \int_0^\infty z (e^{-\frac{U(z)}{k_b T}} - 1) dz$. Hence, the pressure gradient along z (whitin the Debye layer) generates a water "Diffusio-osmotic" flux scaling like the concentration gradient and going from the high to low concentrated area.

This phenomenon is behind the generation of ionic current in the vicinity of charged interfaces submerged into electrolytic solutions in the presence of a tangential concentration gradient. Similarly to streaming currents this flux will drag the Debye layer's counter-ions and results in a net "osmotic" ionic current. It is sensitive to slippage and eventual surface's charges mobility. The osmotic coefficient is obtain from measurement and is expressed as :

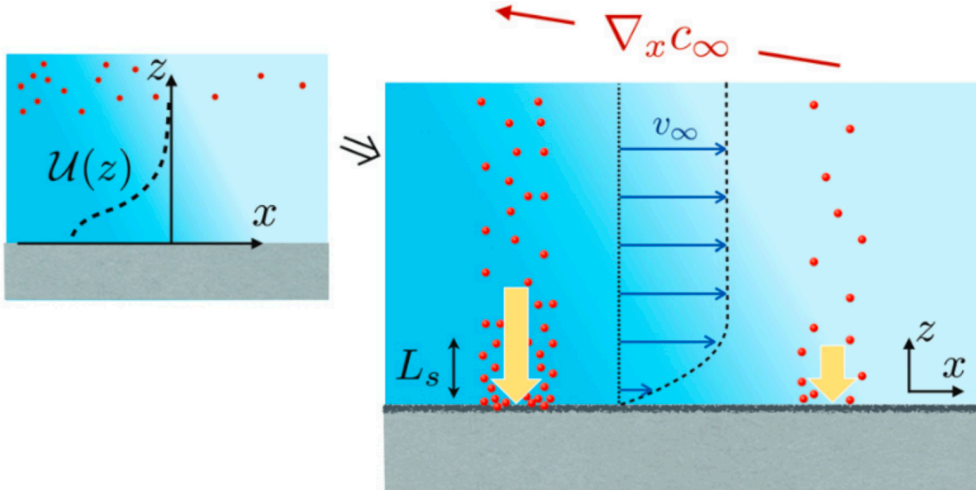
$$K_{osm} = \frac{l}{A} \times \frac{I_{osm}}{\Delta \log(C_s)} \quad (4.30)$$

I_{osm} being the measured osmotic current and $\Delta \log(C_s)$ is the applied concentration gradient across the channel in logarithmic scale.

According to [67] the osmotic coefficient for interfaces with mobile charge is defined as :

$$K_{osm} = \frac{-\Sigma}{h} \frac{k_B T}{2\pi\eta\ell_B} \left(1 - \frac{\sinh^{-1}\chi}{\chi} + (1 - \alpha_{ion}) \frac{b_0}{\lambda_D} \frac{\sqrt{1 + \chi^2} - 1}{1 + \beta_s \times \frac{|\Sigma|}{e} \ell_B^2} \right) \quad (4.31)$$

The first term between the brackets being the no-slip contribution and the second one is the contribution of slippage only. For the case of fixed charge ($\alpha_{ion} = \beta_s = 0$) it reduces to :

**Figure 4.6**

Diffusio-osmosis in the case of solute particles interacting with an interface through an attractive potential. From [8] The interaction of the solute with the interface is higher in the more concentrated side. This generates a force on the fluid that translates into a tangential pressure gradient within the boundary layer from high to low concentration.

$$K_{\text{osm}} = \frac{-\Sigma}{h} \frac{k_B T}{2\pi\eta\ell_B} \left(1 - \frac{\sinh^{-1}\chi}{\chi} + \frac{b_0}{\lambda_D} \sqrt{1 + \chi^2} - 1 \right) \quad (4.32)$$

Diffusio-osmosis, as well as other phenomena, enables the generation of an ionic current from a salinity gradient. This is in fact a conversion of entropy of mixing into usable power that can be converted into usable power. Salinity gradient sources, such as estuaries, are numerous and have a significant potential for the production of a clean and non-intermittent energy. The harvesting of this osmotic "blue" energy have been the object of intense research in the last decade [69]. In the next chapter we make a short review of this field.

A review of osmotic energy harvesting

Important amounts of energy could be extracted from the mixing of fresh and salt water in the estuaries. First industrial pilots have been built in Netherlands and Norway but their performance remain low in part because of an inefficient membrane process. The giant power densities measured at the single pore level have brought a huge momentum to the field of osmotic energy harvesting, especially through the quest for better materials for membrane engineering. Although those performances fall down, they still remain high at the centimetric scale, in particular with carbon based materials. Here we discuss briefly the state of the art of osmotic energy harvesting: its industrial potential and the technologies developed to harvest it from the single pore to the industrial scale.

5.1 Industrial potential and current limitations

With the acceleration of global warming the need for clean and non-intermittent sources of energy becomes more and more pressing. In that context the harvesting of osmotic (blue) energy could play a role in the near future. By entropy of mixing, up to 0.8 kWh/m^3 of water are theoretically available from the various estuaries on the planet [70]. From this energy source, the usable power that may be harnessed is estimated to be on the order of 1 TW [71], equivalent to 14 times the french total production of energy. However harnessing this energy is a considerable fundamental and technical challenge.

Currently two industrial pilots have been built relying on different technologies. The first one was operated by Statkraft at Tofte in Norway and relies on pressure retarded osmosis (PRO) (Figure 5.1.a). Because of the low power density obtained (1 W/m^2 of membrane) resulting in too expensive electricity, this project had to stop in 2014. On the other-hand reverse electrodialysis is more promising (Figure 5.1.b) and the pilot plant built by REDstack at Afsluitdijk is still operational and under development since it opened in 2014. For both technologies, limitations are coming from a low efficiency of the membranes. The osmotic pressure (which is the driving force) is high (30 bars) between the sea and the fresh water [70]. However, semipermeable or perm-selective membranes require sub-nanometric confinement. Thus, this colander-like strategy impedes fast water/ionic transport.

There is therefore a strong need for a paradigm shift to make blue energy harvesting

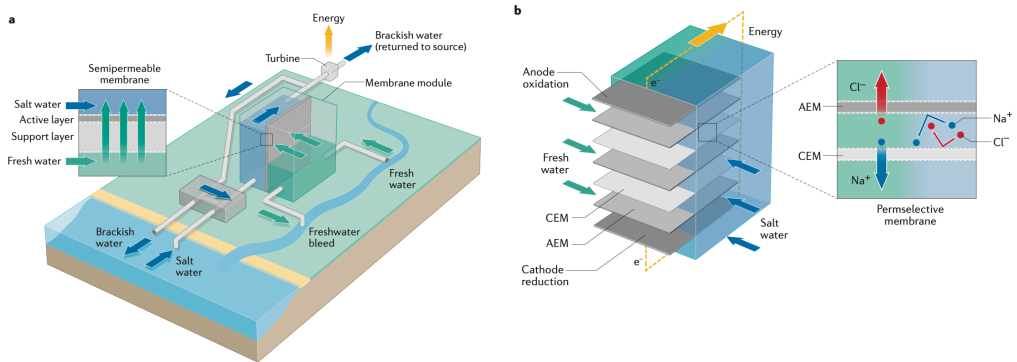


Figure 5.1

Osmotic power generation in industrial pilot projects, from [70]. **a**, Power generation by pressure retarded osmosis (PRO). A water flux is generated by forward osmosis using a semipermeable membrane separating a fresh and a sea water reservoirs. This flux is then used to rotate a turbine similarly to classical hydroelectric power plant relying on gravitational energy. **b**, Power generation by reversed electrodialysis (RED). Ionic transport by diffusion through perm-selective membranes, cation exchange membrane (CEM) and anion exchange membrane (AEM), is converted into usable power with electrodes. Here the conversion from entropy of mixing to electrical energy is more direct as it does not require a turbine.

a reality at the industrial scale. Looking for new solutions to harvest blue energy is usually a two step process. First, studying single pores having a well controlled geometry enables a fundamental understanding of the physics at play. It allows a rigorous screening of efficient materials for energy harvesting and a deep understanding of relevant phenomena such as diffusio-osmosis (DO). Second, once an efficient material is identified, the next step is to fabricate a centimetric scale membrane and to study its performances. Usually, a huge loss in power density occurs between the single pore and the macro-scale membrane pointing to the importance of the membrane's architecture and cell design for efficient energy conversion [72, 73].

5.2 Single Pores

A useful metric to assess the performances of a single pore in terms of energy harvesting is the maximum single pore power density defined as [57, 74]:

$$P_* = \frac{P}{A} = \frac{I_{osm} V_{osm}}{4A} = \frac{I_{osm}^2}{4AG} \quad (5.1)$$

With P the max power available, I_{osm} the osmotic current, V_{osm} the osmotic potential and A the channel cross section. This metric cannot be used to predict the osmotic power at large scale because the scaling with the number of pore is expected to be strongly sub-linear [73]. However it can be safely used to compare single pores of different cross sections and materials with each other.

Before the advent of nanomaterials, study of osmotic energy harvesting started with polymeric films pierced using focused ion beams. In 2010, Guo and coworkers could measure significant osmotic currents corresponding to osmotic powers of up to 100 pW [75] (Figure 5.2.a). The authors claimed that by parallelizing their pore at a

density of 10^{10} cm $^{-2}$ they would obtain three orders of magnitude higher power density than ion exchange membranes (CAM and AEM) used in RED. Even if we now know that this extrapolation cannot be done because of the sub-linear scaling with the number of pore, this still tends to demonstrate that it is possible to harvest osmotic energy with pore of nanometric (and even micrometric) diameters allowing both anions and cations to pass through. This shows that a colander strategy is not required thanks to the DO mechanism. A recent (2020) improvement of the energy harvesting power was recently obtained with mesopores fabricated by Gao and co-workers [76]. They enlarged a nano-pore obtained similarly as [75] by electrochemical etching. This resulted in a factor of 10 increase in osmotic current relative to Guo et al which induced an increase in net power by a factor of 6 and single pore power density of 2 to reach 5000 W/m 2 (Figure 5.2.b). This may be explained by the higher amount of interfacial area in a larger pore, which is the location of power generation under a DO mechanism, definitely showing that sub-nanometric confinement is not required. Another factor in favor of tracked-etched nanopores is the contribution of asymmetric (conical) geometry which enhances the energy harvesting by reducing the dissipation within the channel [70, 77].

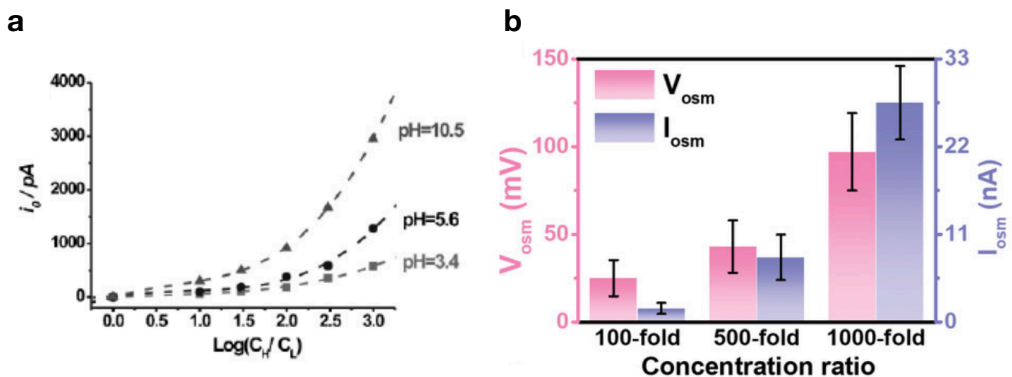
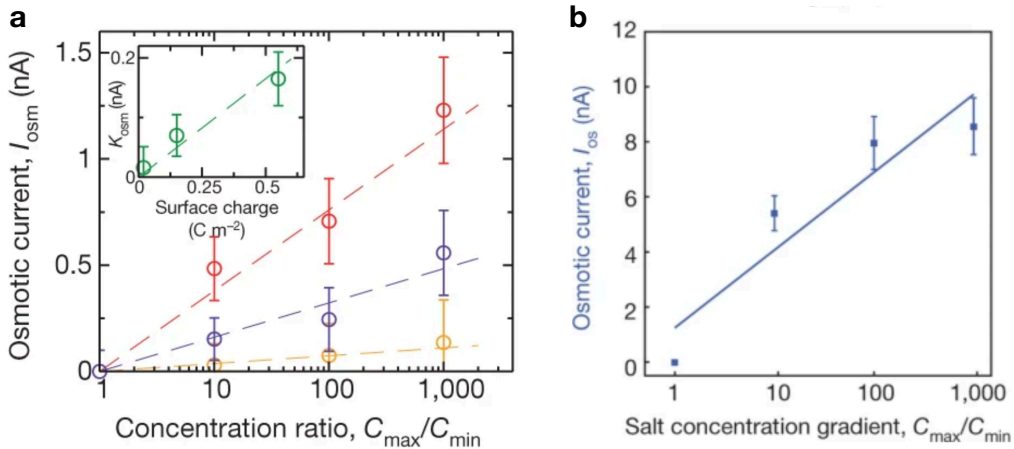


Figure 5.2

Osmotic power generation in tracked-etched single pores. **a**, Osmotic currents vs concentration drop in a conical nanopore (radius : 1200 nm (base) / 41 nm (tip)) at various pH, from [75]. **b**, Osmotic currents and potentials vs concentration drop in a conical mesopore at pH 11 (radius : 920 nm (base) / 410 nm (tip)). [76]. The osmotic potential corresponds to the external potential required to cancel the osmotic current.

Nanomaterials have shown exceptional performances for energy conversion. In 2013, Siria et al. studied ionic transport inside a single transmembrane BN nanotube (Fig 5.3.a). They have shown that BNNTs can have a very large fixed surface charge of up to $1\text{C}/\text{m}^2$ at high pH [57]. This high charge enables significant osmotic energy harvesting by DO mechanism with single pore power density reaching $5000\text{ W}/\text{m}^2$. Activated carbon nanochannels, because they exhibit significant slippage while relying on the same driving force (DO induced by fixed charge), are a significant improvement. Those results are presented in the next chapter.

BNNTs performances were overtaken by two orders of magnitude in 2016 using atomically thin MoS $_2$ nanopores (Fig 5.3.b) [55]. It was shown that osmotic energy harvesting in such pores strongly decreases with the pore's thickness [55, 77]. This points to a different mechanism than DO for the energy generation. Owing to their

**Figure 5.3**

Osmotic power generation with nanomaterials. **a**, Osmotic currents vs concentration drop in a BNNT (radius 40 nm) at pH 5.5 (yellow), pH 9.5 (purple) and 11 (red), from [57]. The scaling of the osmotic coefficient with the surface charge, obtained from conductivity measurements, is linear as expected for a DO mechanism. The osmotic currents are of the same magnitude of the ones obtained in track etched nanocone in Figure 5.2.a with a much lower cross section. We attribute this better performance to the giant surface charge on h-BN promoting efficient DO-induced transport. **b**, Osmotic currents vs concentration drops across a bi-layer MoS₂ nanopore at pH 11 (radius : 5nm) [55].

atomic thickness, the concentration gradient across such pore is maximized. Then, as the pores carry a negative surface charge, the effective cation diffusion coefficient increases and the anion diffusion coefficient decreases in the vicinity of the pore. The pore becomes (partially) selective and effectively filters the ions (allowing mostly cations to pass through) that are pulled from the highly concentrated reservoirs to the least concentrated reservoirs owing to Fick's law. This diffusion driven motion into a selective pore is reminiscent of RED and colander strategy, but with a highly charged and atomically thin colander. The authors find that the optimal pore diameter is of around 10 nm. Smaller pores favors low osmotic currents and large pores have a reduced selectivity. By coupling two nanopores with a an electronic transistor made of a single layer of MoS₂ they could present a first example of self powered nanosystem. This proof of concept illustrates that single pore power generation can be usable *per se* and the goal of such studies is not only to prepare the ground for harvesting osmotic energy at larger scales. Building on those results, Graph et al. were able to enhance the osmotic energy generation using laser illumination [78]. They attribute this result to a photo gating effect of the surface charge. This suggests possibilities for fine tuning of ion transport, which remains a fundamental challenge (see Chapter 9) using external light sources. Also, as pointed by the authors, exposing osmotic energy cells to sunlight may yield better performances in industrial applications.

5.3 Macro-scale membranes

The efficiency of a macro-scale membrane for osmotic energy harvesting is assessed with the power density defined as :

$$P_s = P/A \quad (5.2)$$

Up-scaling of a track-etched nano-pores has been presented by Ma and coworkers [79]. They could measure a power density of 0.02 W/m^2 at pH7 that could be increased to 0.37 W/m^2 by stacking up several membrane in a RED fashion (Figure 5.4.a). By taking into account the material's porosity, the authors calculated a factor of 20/30 losses in term of power density relative to their single pore power density. As displayed in Figure 5.4.b, the single transmembrane BNNT device was recently upscaled [80]. This enabled, an efficient power generation of 0.165 W/m^2 obtained at pH 11 and max concentration gradience. This corresponds to a factor 50 decrease in power density compared to the single pore device (taking into account the material's porosity).

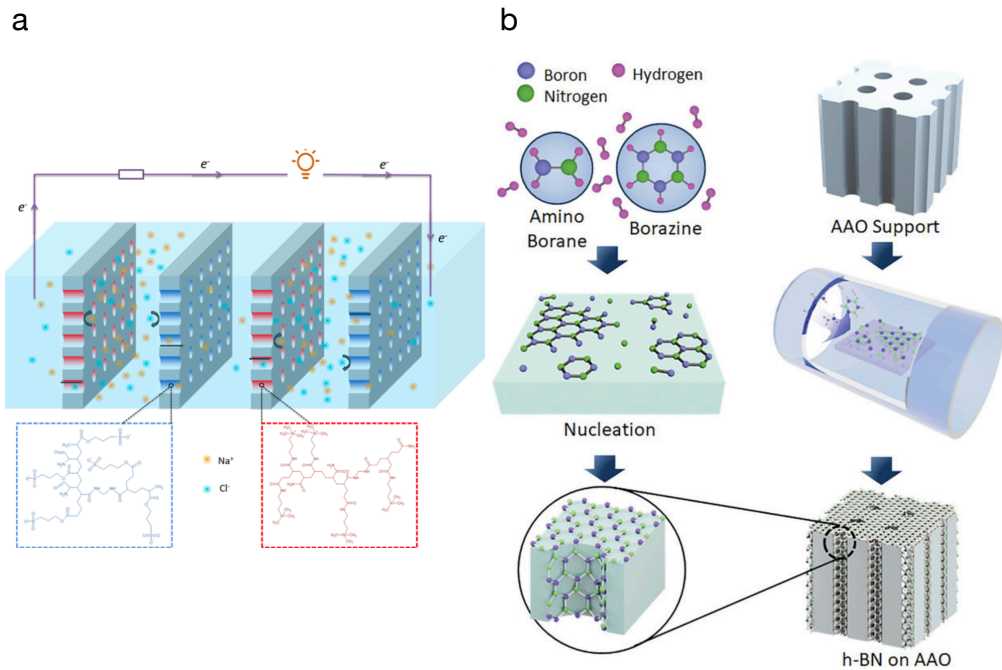


Figure 5.4

Osmotic power generation in multipore membranes. a, Tracked-etched membrane negatively or positively functionalized using different hydrogels, from [79]. b, Array of Boron Nitride nanotubes obtained by chemical vapor deposition inside an anodic aluminium oxide membrane, from [80].

The huge losses in power density from single pore to membrane have been attributed to polarization concentration or entry resistance [72, 73]. However, research on high

performance single pore enabled the discovery of membranes generating significant amount of osmotic power. This demonstrates the validity of the 2-step approach (single pore followed by upscaling) in order to obtain the best performance at the centimetric scale.

Carbon materials, in particular graphene oxide (GO) membranes have raised high hopes for osmotic energy harvesting. They combine a high surface charge with a low carbon/water friction as well as low costs and versatility in fabrication. Zhang and coworkers could reach a power density of 10.6 W/m^2 , significantly higher than other material's [43]. They have shown that GO offers great performances when the concentration gradient is parallel to the GO sheets (Figure 5.5.a). Those performances were further increased by a factor 4 thanks to a novel technique enabling to fabricate highly oriented GO fibers (Figure 5.5.b) [44]. The flux here also being parallel to the fiber. Innovations in fabrication are required to fabricate large scale area of vertically aligned GO. Yet the performances displayed by GO are already very exciting. They suggest an enhanced material performance and call for a characterization of ionic transport and osmotic energy harvesting with a single nanochannel made of carbonaceous material. Such a study is still lacking and this will be our objective in the next chapter.

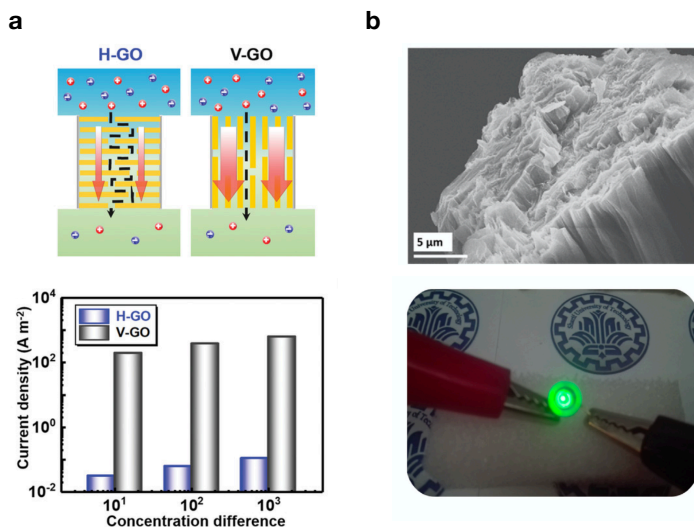


Figure 5.5

Osmotic power generation with graphene oxide. **a**, Graphene oxide encapsulated in epoxy then measured tangentially to the sheets (Vertical GO), from [43]. Up : fluid flow inside regular GO (H-GO) versus vertical GO (V-GO). The fluidic path is direct with V-GO leading to lower losses and more efficient transport. Down : Osmotic current density vs concentration gradient for GO in both configurations. Using V-GO increases the performances by three orders of magnitude. **b**, Graphene oxide fibers fabricated using a rotating coagulation bath, from [44]. Up : SEM image of the fibers. Down : LED powered by osmotic energy using 18 fibers in series.

Results: Enhanced nanofluidic transport in activated carbon nanochannels

The field of nanofluidics has undergone a major leap with the recent development of artificial channels with nanoscale and subnanoscale dimensions, which unveiled a wealth of unexpected behaviors and knowledge gaps [1, 23, 36, 81, 82]. Carbon emerges as a unique material as a water and ion channel, with numerous reports of fast water transport, molecular ion separation, efficient osmotic energy conversion [40, 41, 66, 83–85]. Many of these phenomena still await proper rationalization and further progress is impeded by a lack of fundamental understanding of nanoscale ion transport, which can only be achieved in controlled environments. In this chapter, we investigate ionic transport in nanoscale carbon conduits with unprecedented details thanks to a direct comparison of 'pristine' graphite [23] to 'activated' carbon as nanoconduits. We show that the 'activated' carbon nanochannels outperforms pristine carbon nanochannels by orders of magnitude in terms of ionic conductance, streaming current, (epi-)osmotic currents and surface electrification. A detailed theoretical framework allows us to attribute the enhanced ionic transport across activated carbon nanochannels to an optimal combination of high surface charge and low friction. Further, this demonstrates the unique potential of activated carbon for energy harvesting from salinity gradients, known as osmotic power [69, 77], with single pore power density across activated carbon nanochannels reaching hundreds of kW/m², surpassing alternative nanomaterials [55, 57, 77, 86–89].

This part of the thesis was done in collaboration with the Angstrom-scale fluidics group of the Manchester University. Vasu Kalangui fabricated and measured the pristine nanochannels and O₂-activated nanochannels. Ashok Keerthi also fabricated one pristine nanochannel device.

6.1 Motivation and methods

Two-dimensional (2D) materials and their heterostructures fabricated using vdW assembly established a unique platform for exploring novel phenomena in various fields such as condensed matter physics, nanofluidics and nano-optics [36–39]. In particular the study of graphene based membranes – including up-scalable graphene oxide membranes – for fluidics applications has recently emerged as a research domain of its own, now referred to as carbon nanofluidics. Carbon materials have indeed shown exceptional properties when interacting with nanoconfined fluids and offer unprecedented opportunities for ionic sieving, ultra-fast permeation and electrochemical energy harvesting [23, 40, 41, 44, 66, 83, 84, 90–92]. In this context, the recent emergence of advanced nanofabrication techniques, enabling the investigation of transport across one- and two- dimensional carbon nanoconduits with well-controlled geometries, has considerably extended the fundamental understanding in this field. Pristine carbon nano-capillaries can now be fabricated with atomic scale precision by using graphene as a spacer, which led to the discovery of many fascinating and unexpected phenomena [24, 25]. Here, we introduce new routes to pattern 2D nanochannels using either electron beam induced direct etching inside an environmental scanning electron microscope (SEM) or electron-beam lithography followed by reactive ion etching (RIE). Once covered by a top-layer 2D material using vdW assembly, this allows fabrication of nanofluidic devices with 'activated' carbon channels. In addition to the existing fabrication method for making pristine carbon nanocapillaries [23], we have a comprehensive platform at our disposal to thoroughly investigate the nanofluidic transport on both pristine and 'activated' carbon surfaces, see Fig. 6.1.a-c, to understand the influence of surface modification. We conduct a comparative study of these two distinct carbon nanochannels : symmetric pristine channels with two pristine walls and asymmetric activated channels with one activated wall and one pristine wall. This not only sheds a new light on the detailed mechanisms of ionic transport, but also highlights the performance of activated carbon for osmotic energy conversion. Recent studies have shown exceptional performance in terms of energy conversion across boron nitride nanotubes and MoS₂ nanopores, reaching values of 5 kW/m² - 1 MW/m² [55, 57]. At larger scales, membranes made of graphene oxide have shown excellent performance in this context [44, 93], which one may relate to the functional groups on their surface [94], or defects [77]. A systematic study to uncover how carbon surface properties determines osmotic energy efficiency is however lacking. This is our objective in this work: we unveil, and rationalize, the outstanding performance of activated carbon for ionic transport and specifically for osmotic energy conversion.

Pristine graphene nanochannels, Fig. 6.1b, are prepared as in Refs. [23–25]. Briefly, a single crystal of known thickness is patterned using ebeam lithography (EBL) and etched using dry etching to form an array of strips (spacer layer). This spacer layer is used to separate two graphite crystals (top and bottom layers) of thickness between 70 to 100 nm using vdW assembly. The channels consists of the free space remaining between the strips (Fig.6.2a). Fluidic device with 'activated' carbon nanochannels (Fig.6.1c) is fabricated by etching the nanochannel in a bottom crystal of 50 to 100 nm. The bottom is then covered by a top layer of similar thickness. Two different nano-fabrication process are used to fabricate the activated nanochannels.

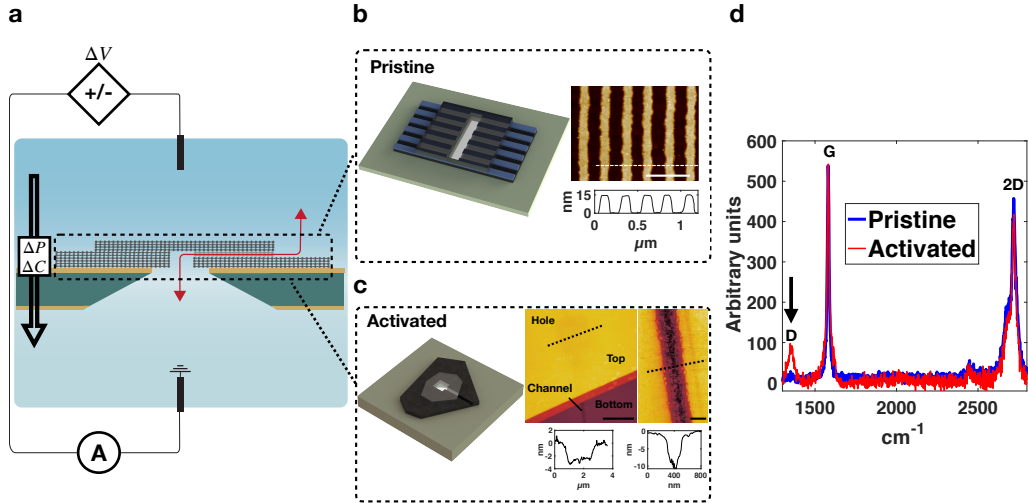


Figure 6.1

Nanofluidic 2D channels and measurement setup. **a**, Experimental Setup. Voltage, pressure or concentration drop are used to induce an ionic current across two different kinds of graphene 2D nanochannels. **b**, Pristine channels. Left : schematic, the Silicon Nitride membrane is grey, the bottom layer is black, the spacers are blue and the top layer is glassy transparent grey. Right : Atomic force microscopy image. **c**, Activated channels. Left : schematic, the Silicon Nitride membrane is grey, the bottom layer with a milled nanochannel is black and the top layer is glassy transparent. Middle : Atomic force microscopy image, the cross section displays limited sagging of the top layer over the bottom layer's through-hole, confirming good interlayer contact. Scale bar: 2 micrometers. Right : Atomic force microscopy zoomed image of the channel with cross section. Scale bar: 150 nanometers. **d**, Raman characterization of pristine graphitic surface and, activated graphitic surface created by SEM milling.

In the first method the channels are etched in an H_2O reactive environment inside a Scanning Electron Microscope (SEM) while in the second, the channels are etched in O_2 using Reactive Ion Etching (RIE).

For the H_2O -etched channels, first, we created a square-shaped aperture ($1\ \mu\text{m} \times 1\ \mu\text{m}$), see Fig.C.2 and Fig 3.1, on the bottom layer graphite crystal by completely etching through it via electron beam induced direct etching (EBIE) in a water vapor environment inside a SEM [49]. Using the same method, a trench of few micrometers length and, channel height varied between 3 and 13 nm is made from one end of the square-shaped aperture by making sure the trench and the aperture are connected. We then placed a top layer graphite crystal on the patterned bottom layer using vdW assembly to fabricate the activated nanochannel. This whole assembly prepared on SiO_2/Si substrate is finally transferred onto a Silicon Nitride (SiN_x) membrane with a circular aperture of diameter $10\ \mu\text{m}$. (see Chapter 3).

For the O_2 etched channels, a bottom layer graphite is first transferred onto the silicon nitride membrane with a rectangular hole of $3\ \mu\text{m} \times 20\ \mu\text{m}$. Then, the rectangular hole in SiN_x membrane is extended into the bottom layer using oxygen plasma dry etching in RIE from the backside of the Si/SiN_x wafer. Subsequently, the bottom layer is patterned using e-beam lithography and oxygen plasma dry etching

in RIE to create a single channel. Finally, a graphite crystal is transferred on top of this patterned bottom layer with single channel to obtain the nanochannel device for our experiments (see Appendix C.1.1). Graphite crystals used in this work to fabricate fluidic devices with pristine and activated nanochannels are obtained by mechanical exfoliation.

Overall, our focus in this work is to investigate surface effects – specifically surface electrification, slippage and their consequences on ionic transport –, thus we targeted channels with only moderate confinement in the range of several nanometers (from 3 to 15 nm), in contrast to previous studies with graphite channels, see *e.g.* [23, 26]. This moderate confinement allows us to disentangle surface from bulk effects in the ionic transport and characterize surface properties. Here, the studied pristine channels with atomically smooth channel walls are 5-15 nm in height, 120-200 nm in width and a few micrometers in length, while the activated channels are 3-13 nm in depth, 100-300 nm in width and a few micrometers in length. We studied three pristine channel devices with $N=1, 30, 200$ channels; and eight activated channel devices (five were H_2O -etched and three were O_2 -etched), with $N=1, 3, 4$ channels; see Appendix C.4 for the detailed geometrical aspects of the pristine channel (labeled as A, B, C) and activated channel (labeled as D-K) devices used in this work. Due to the small response, particularly for streaming measurements, the pristine channel devices are made with multiple channels. Measurements in this work are normalized to a single channel for comparison. As a result, we found minor variations in the measurements for the different devices of the same kind. For example, in view of the qualitative consistency (discussed in the later sections), normalizing the experimental data to a single channel led to minor variations in salinity dependent single channel conductivity, zeta potential and extracted surface properties (surface charge and slip length) for the 3 pristine channel devices (Systems A, B and C) investigated in this work. It also applies in the case of activated nanochannel devices (Systems D-K), even though slight differences are noticed between H_2O and O_2 -etched channels (see Appendix C.3.7).

6.2 Material characterization by conventional techniques

Atomic force microscopy analysis shows that the H_2O -etched channel wall exhibits a relatively increased roughness of typically 0.7 to 1.1 nm r.m.s., see Fig.6.1.c and appendix C, compared to the 200 pm r.m.s. roughness of the pristine graphite crystal. In addition, Raman spectroscopy, Fig.6.1.d, – with 350 nm lateral resolution – on the activated channels shows D-peak, representing the defects on sp^2 crystalline structure of graphite [95, 96] due to EBIE. The emergence of a D-peak has also been observed after oxygen plasma treatment of graphite [97]. Hence, the key difference between pristine and activated nanochannel is that, in pristine nanochannel both the channel walls are made of pristine graphitic surface whereas in the activated nanochannel, the bottom channel wall contains charged sites and nanometric roughness. In H_2O -etched nanochannels, we attribute this defect formation to the etching of graphitic surface with highly reactive radicals such as $OH\bullet$, $H\bullet$, and $HO_2\bullet$, created by the electron beam under water vapor atmosphere in environmental SEM [48, 49]. Further, molecular dynamics simulations have shown that water self-dissociation on graphene edges is energetically favorable [98]. Thus,

the EBIE/RIE induced defects and self-dissociation of water could contribute to the high surface charge in 'activated' nanochannels – as indeed confirmed below – which governs the ionic transport across them. Our electrostatic force microscopy measurements further confirm the difference in surface charge distribution on pristine and activated graphite surfaces (Appendix C.1.2). Chemical analysis of EBIE-made nanoscale patterns remains out of reach because of the spatial resolution of the chemical probes. Our XPS chemical analysis of millimetric-scale graphite exposed to the same RIE program used to obtain the O₂-etched nanochannels unveils an increase of oxygen and C/O species following the etching (Appendix C.2). This is in good agreement with previous XPS analysis of O₂ and H₂O plasma exposed graphite [97, 99] and point to the presence of charged C/O groups attached to the activated channel's bottom wall.

6.3 Nanofluidics material characterization

Ionic current measurements under various driving forces are performed by clamping the nanofluidic devices between two reservoirs as described in [23, 57]. These reservoirs are filled with potassium chloride (KCl) solutions with concentration C_s varying between 1 mM and 1 M; pH is also varied between 3 and 9. Silver Chloride (Ag/AgCl) electrodes placed in the reservoirs are used for electrical current measurements and voltage drop application. They are connected to a patch clamp amplifier (*Molecular Devices Axopatch 200B*). First, the response to voltage drop and pressure drop is measured. Voltage drop between -100 mV and 100 mV is applied with 5 seconds steps of 10 mV. The last current value of each step is recorded. The pressure is applied with a pump connected to the channel's side reservoir with an integration time of typically 15-100 s (see Appendix C.3). Osmotic current measurements are performed by filling each of the reservoir with solutions of different KCl concentration. Specifically, the reservoir connected to the channel is filled with a 1 M KCl solution while the other side is loaded with solution with concentration 10⁻³ M-1 M (see Appendix C.3). All measurements are sampled at 1 kHz with an acquisition time set to 0.1 s.

Before tackling the osmotic energy conversion across the various carbon devices, we first perform an exhaustive investigation of their ionic response and surface properties. Hence, we first explore ionic transport through pristine channels under voltage and pressure drop, Fig.6.2a-d. Such experiments [under voltage drop and pressure drop] enable measuring the conductivity and electro-osmotic mobility (or zeta potential) respectively. This allows us to characterize the electrokinetic properties of the system and get insights into the water-graphite and ion-graphite interfacial behavior. The pristine channels exhibit a linear dependence of the ionic current (per channel), I/N , with applied voltage ΔV (Fig.6.2a) and show a strong dependence of the single channel conductivity, $K/N = \frac{L}{N \cdot w \cdot h} \frac{I}{\Delta V}$ (L,w,h the length, width and height of each channel) with the salt concentration, Fig.6.2b. Further insights on the surface electrostatic properties are obtained by streaming current measurements, Fig.6.2c, where the ionic current I_{stream} is measured as a function of an applied pressure drop ΔP . I_{stream} exhibits a linear response versus ΔP for all KCl concentrations as shown in Fig.6.2c and one extracts the electro-osmotic mobility ($\mu_{EO} = \frac{L}{Nwh} \frac{I_{stream}}{\Delta P}$). The zeta potential of the surface is defined using Smolu-

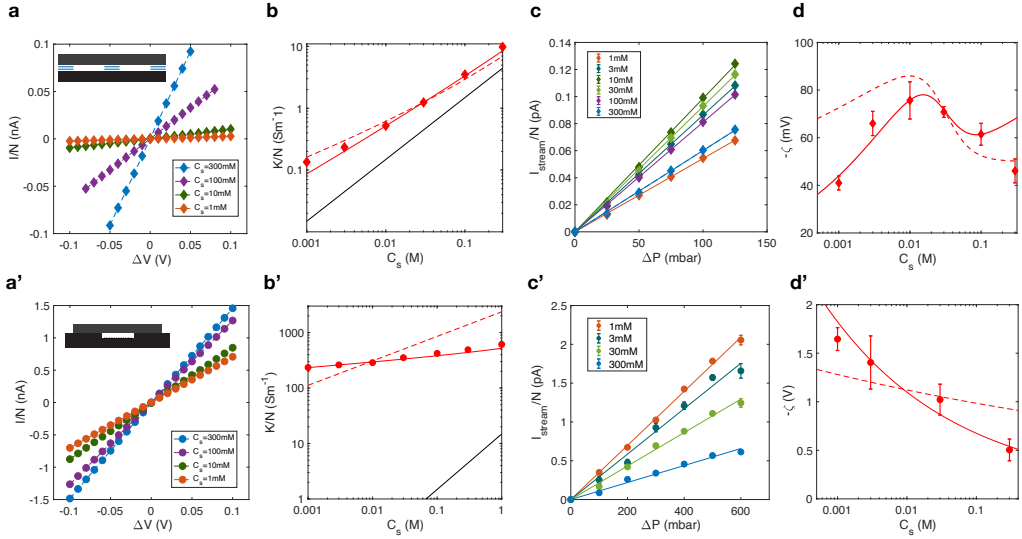


Figure 6.2

Ionic transport across pristine and activated channels. Pristine channels: **a**, Ionic current under voltage drop, normalized per channel (System A: $N = 200$ channels, $\text{pH}5.5$, thickness $h = 15 \text{ nm}$). Inset: schematic cross sectional view of pristine nanochannels. **b**, Conductivity versus salt concentration at $\text{pH} 5.5$. Diamond points are experimental data. Solid black line represent the bulk theoretical conductivity. The red, solid and dashed, lines are the theoretical predictions for the conductivity using the electrokinetic framework building on Eq.(1). The solid red line assumes a scaling behavior $\Sigma(C_s) \propto C_s^{0.68}$, while the dashed red line corresponds to a constant surface potential prediction with $\Psi_0 = -50 \text{ mV}$ in Eq.(6.1); see text for details. All parameters for the concentration dependence of the surface charge and slip are summarized in the Appendix C. **c**, Streaming current under pressure drop, normalized per channel, for various salt concentrations ($\text{pH}5.5$) **d**, Zeta potential versus salt concentration ($\text{pH}5.5$). Diamond points are experimental data. The solid and dashed lines are the predictions for the zeta potential using the surface charge scaling and constant surface potential, respectively, using same parameters as in panel **b**. **Activated channels:** **a'**, Ionic current under voltage drop, normalized per channel (System E: $N = 4$ channels, $\text{pH}=5.5$, thickness $h = 3 \text{ nm}$). Inset: schematic cross section view of an activated nanochannel. **b'**, Conductivity versus salt concentration. Solid circles are experimental data. Solid black line represent the bulk theoretical conductivity. The red solid and dashed lines are the predictions for the conductivity using the surface charge scaling ($\Sigma(C_s) \propto C_s^{0.32}$) and constant surface potential ($\Psi_0 = 240 \text{ mV}$), respectively. Parameters for the concentration dependence of the surface charge and slip length are summarized in the Appendix C. **c'**, Streaming current under pressure drop, normalized per channel, for various salt concentrations ($\text{pH}5.5$). **d'**, Zeta potential versus salt concentration ($\text{pH}5.5$). Solid circles are experimental data. The solid and dashed lines are the predictions for the zeta potential using the surface charge scaling and constant surface potential, respectively, using same parameters as in panel **b'**. Error bars in panels **d** and **d'** are standard deviations from three and five measurements, respectively.

chowski expression, $\zeta = -\frac{\eta}{\epsilon\epsilon_0}\mu_{EO}$ (with η the water dynamic viscosity, ϵ the water relative permittivity, ϵ_0 the vacuum relative permittivity). Note that the Smoluchowski expression remains valid down to nanometric confinement [26]. The zeta potential is used here as a phenomenological parameter quantifying electro-osmotic mobility. It is one of the few tools available for studying charged interfaces along with short interaction microscopy and spectroscopy methods [100]. The zeta potential exhibits a non-monotonic dependence on the salt concentration, with relatively high values ranging between -40 and -80 mV ; Fig.6.2d.

Let us turn to the ionic response across the activated channels. The ionic conductivity – as obtained from the I-V characterization, Fig.6.2a' – is shown in Fig.6.2b'. Ionic conductivity of activated channels is found to be several orders of magnitude larger than the bulk conductivity (solid line), as well as ionic conductivity observed

for the pristine channels in Fig.6.2b, furthermore with a weak dependence on the salt concentration. Such a very strong deviation from bulk effects are confirmed by streaming current measurements on the activated channel, Fig.6.2c', and the corresponding zeta potentials in Fig.6.2d'. These measurements on activated carbon surface highlight huge values of zeta potential, ranging between -0.5 to -2 V (one order higher than that of pristine graphitic surface). To the best of our knowledge, such values of zeta potentials are unprecedented. Nanofluidic transport inside systems with low friction alone, such as pristine nanochannels, or high surface charge alone, such as h-BN nanochannels [24, 26] or nanotubes [57] is of lower magnitude. These behaviors are obtained for all devices with activated surfaces that we measured in the present study, see Fig.6.3 for the conductivity.

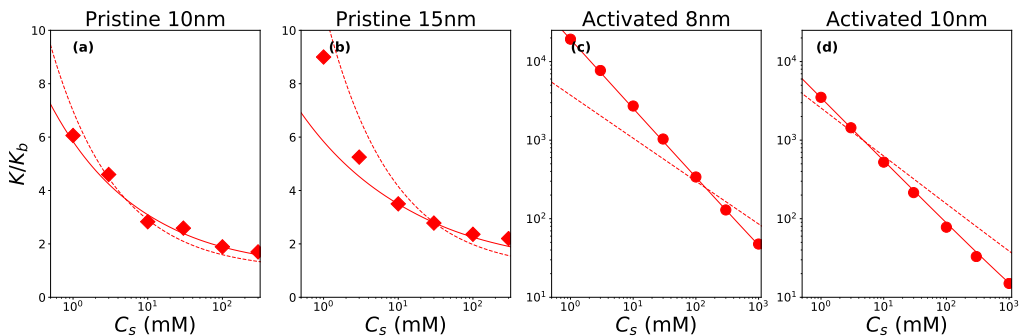


Figure 6.3

Conductivity enhancement for pristine and activated channels: conductivity enhancement K/K_b versus concentration, with $K_b = 2e^2\mu C_s$ the bulk predicted conductivity (pH5.5). **a**, System B: pristine channel with thickness $h = 10$ nm, **b**, System A: pristine channel with thickness $h = 15$ nm, **c**, System F: channel with activated surface and thickness 8 nm, and **d**, System D: channel with activated surface and thickness 10 nm. In all panels, points are experimental data and lines are the theoretical predictions for the conductivity enhancement using Eq.(6.1); see text. The solid red line assumes a scaling behavior $\Sigma(C_s) \propto C_s^\alpha$, while the dashed red line corresponds to the predictions assuming a constant surface potential Ψ_0 ; see text for details. For the pristine channels with 10 and 15 nm thickness, $\alpha = 0.62$ and $\alpha = 0.68$ respectively, while for the 8 and 10 nm activated channels, $\alpha = 0.33$, $\alpha = 0.40$ respectively. For the surface potential, we use $\Psi_0 = -0.025$ V and $\Psi_0 = -0.050$ V for the pristine channels (panel a and b, respectively), while results using $\Psi_0 = -0.220$ V, -0.210 V are shown for comparison for the 8 and 10 nm channels (panels c, d, respectively). All detailed parameters for the concentration dependence of the surface charge and slip are summarized in the Appendix C.

Before taking benefit of such unique properties, the previous results for both the pristine and activated carbon channels call for a proper understanding. The high conductance and electro-osmotic mobility immediately indicate considerable surface transport, however we show that a complete rationalization of our experimental data is reached only after considering the concerted role of surface electrification and hydrodynamic slippage [2, 26].

Our experimental data reporting both conductance and electro-osmotic mobility allows to disentangle both effects and provide much insight into the molecular surface mechanisms. For pristine channels, though the channel height is larger than Debye length for most experiments, the conductivity per channel for all concentrations is found to be significantly larger than the bulk conductance, $K > K_{\text{bulk}} = 2\mu e^2 C_s$ (per channel, with μ the salt bulk mobility $\mu = \frac{1}{2}(\mu_{K^+} + \mu_{Cl^-})$ [2]); $\mu = D/k_B T$ with D the diffusion coefficient and $k_B T$ the thermal energy. This is in contrast to

what would be expected, as for such channel sizes, bulk effects are usually dominant at large ($\sim 1\text{M}$) concentrations. It was recently pointed out by experiments in CNTs and *ab initio* simulations [58, 101] that electrification of pristine graphite can result from physisorption of hydroxide ions on the carbon surface, with the OH^- ions keeping a large motility on the surface. The effect of surface charge mobility on the ion transport in confined channels is accounted for by the framework introduced in [26, 67], which, as a key ingredient, includes a supplementary contribution to the conductivity associated with the mobility of the surface charge of the form, $2\mu_m \frac{\Sigma_m}{h}$ with Σ_m the physisorbed charge, μ_m the surface mobility of the physisorbed ions (here, hydroxyl ions with $\mu_m \approx \mu_{\text{OH}^-}$ [101]). The effect of this mobile surface charge, as evidenced in *ab initio* simulations in [101], has not been properly appreciated up to now. Typically, hydrophobic surfaces with low surface charge are shown to be significantly influenced by the mobile surface charge [58, 67, 101].

Our analysis is based on the transport framework introduced in [26, 67, 102] and accounting for the effects of mobile charge, hydrodynamic slippage and non-linear Poisson-Boltzmann electrostatics. For pristine graphite, we will neglect any chemisorbed surface charge. see Appendix C.4 for the summary of modeling parameters and assumptions.

$$\begin{aligned}
 K_{\text{surf}} &= \frac{2}{h} \left[\mu e |\Sigma_m| (1 + \delta) \times \frac{\chi}{\sqrt{1 + \chi^2 + 1}} + \frac{b_0}{\eta} \times \frac{(1 - \alpha_{\text{ion}})^2 \Sigma_m^2}{1 + \beta_s \times \frac{|\Sigma_m|}{e} \ell_B^2} + e \mu_m |\Sigma_m| \right] \\
 \mu_{EO} &= - \left[\frac{\epsilon \Psi_0}{\eta} + \frac{b_0}{\eta} \times \frac{(1 - \alpha_{\text{ion}}) \Sigma_m}{1 + \beta_s \times \frac{|\Sigma_m|}{e} \ell_B^2} \right] \\
 \chi &= 2\pi \lambda_D \ell_B \frac{|\Sigma_m|}{e} = \sinh \left[\frac{-e \Psi_0}{2k_B T} \right]
 \end{aligned} \tag{6.1}$$

where Σ_m is the charge due to mobile physisorbed OH^- ; b_0 is the slip length; $\ell_B = e^2/4\pi\epsilon k_B T$ is the Bjerrum length and $\lambda_D = (8\pi\ell_B C_s)^{-1/2}$ the Debye length with C_s the salt concentration – here in number of ions per cubic meter –; $\delta = 1/(2\pi\ell_B \mu \eta)$ (η the fluid viscosity). The parameters $\alpha_{\text{ion}} (\in [0, 1])$ and β_s are dimensionless parameters [67] characterizing the differential friction of mobile ions and water molecules with other molecules with respect to the surface. As suggested by previous experiments in [26], we considered $\alpha_{\text{ion}} = 0.8$ and $\beta_s = 50$ for the present work.

The expressions in Eq.(6.1) account for the electro-phoretic and -osmotic contribution to transport, as well as the slippage-induced enhancement of electro-osmosis; the last term of K_{surf} accounts for the mobility of physisorbed hydroxide ions, with $\mu_m \simeq \mu_{\text{OH}^-} = 13 \times 10^{11} \text{ s.kg}^{-1}$. While one expects that such framework can only provide an approximation of the mechanisms at play, it captures all key physical ingredients here and we consider it as guide to rationalize the physics at play. For each salt concentration, one can extract the surface charge Σ_m and slip length b_0 from the combined values of the measured surface conductance $K_{\text{surf}} = K - K_{\text{bulk}}$ and electroosmotic mobility/zeta potential. This enables obtaining analytical expressions of the surface charge and slip length versus the salt concentration, with constant parameters acquired by curve fitting. They can then be used in equation 6.1 to predict the conductivity and zeta potential (solid and dashed lines in Figure 6.2-3). We note that the fitting procedure for the combined conductivity and zeta

potential does not converge for lowest and highest concentration, corresponding to low charge/high slippage and *vice-versa*. Results are summarized in tables C.1 and C.2 for the pristine channels considered (at pH 5.5). We emphasize that without the contribution of mobile charge to the conductivity in Eq.(6.1), it is not possible to account consistently for the experimental data for the conductivity and zeta potential. Interestingly the extracted charge is in the range $-(5-50)$ mC/m² and its concentration dependence can be described as $-\Sigma_m(C_s) = \gamma \times C_s^\alpha$ with the exponent α taking consistent values for the two pristine channels, $\alpha = 0.62$ and $\alpha = 0.68$ (C_s in mM); see Tables C.11. Such scaling laws for the surface charge was actually recently put forward, with an exponent in the range 0.3-1 [103–105]. The slip length decrease with salt concentration (and hence surface charge), with values between tens of nanometers down to 1 nm. One can conveniently describe the concentration dependence of the slip length as $b_0(C_s) = B_m/(1 + \omega C_s^\beta)$ with $B_m = 35$ nm, $\omega = 3 \times 10^{-4}$ (C_s in mM) and $\beta = 2.4$ and we will use the same expression for all pristine channels. It is noteworthy that the competing effect between the concentration dependent mobile surface charge and slip length of pristine graphitic surfaces results in non-monotonic behaviour of zeta potential as a function KCl concentration for pristine nanochannels.

Now, using these expressions as inputs in Eq.(6.1) for the concentration dependence of the charge and slip length, one obtains prediction for the enhanced conductivity K/K_b , see Fig.6.3.a-b, and Figure C.9.d; as well as for the zeta potential, see Fig.6.2d, and Figure C.8.b. It shows a very good agreement for all concentrations for both the conductivity and zeta potential. Importantly the mobile charge contribution dominates conductivity (with minor effect of slippage contribution), while the zeta potential is very sensitive to slippage effects. That a unique expression for the slip length allows to reproduce the zeta potential of different channels assesses the robustness of the description. Interestingly, the exponent α for the concentration dependence of the charge is close to 0.5, which is the expected exponent for a constant surface potential in the Debye-Hückel limit. Hence, we also report as a dashed line the predicted concentration dependence for the conductivity and zeta potential using a fixed surface potential Ψ_0 , hence replacing the concentration dependence of Σ_m – (dashed line in Fig.6.3a and 3b and Figures C.10b-11d). The latter shows an overall very good agreement with the experimental data, suggesting that the pristine graphite may be well described by this simple constant potential framework. The values for the surface potential of the pristine carbon surfaces are typically in the range of several $k_B T/e$ (~ 25 mV) as expected for physisorption. This charging mechanism is in good agreement with our pristine channels pH measurements showing an increases of the conductivity with hydroxide ion concentration (see Appendix C.3.6).

Let us now turn to the results for activated carbon surfaces. The considerable enhancement of the conductivity and zeta potential – see Fig.6.2b',d' and Fig.6.3.c-d (see also Figure C.8 and C.9) suggests defect-induced electrification of the activated carbon surface as a dominant mechanism and one can safely neglect the previous mobile charge contribution in this case. Accordingly, we use a simplified version of the previous model, with the mobile charge replaced by a fixed (chemisorbed) surface charge Σ and $\alpha_{ion} = \beta_s = 0$ for fixed charge. This considerable enhancement also indicates that the bottom wall that has been exposed to electron-beam

dominates the ionic transport in the activated channel. Hence, the previous expressions should be divided by a factor of 2 to take into account the activated channel's asymmetry by neglecting the top pristine wall contribution. To verify that the enhancement is not coming from slippage induced by the top layer we fabricated a control activated channel with a slip-less h-BN top layer that also behaved as an activated channel (see Figure C.12). From the combined experimental data for the conductivity and zeta potential, one can infer the surface charge and slippage. Extracted data for the various investigated systems are given in Tables C.4-5. Overall, the surface charge reaches much larger absolute values, in the range of C/m^2 , while the slip length strongly decreases with salt concentration to reach a few Å at high concentration and is typically in the range of Debye lengths. Data for the various activated systems explored – with confinement between 3 and 13 nm –, are consistent with scaling behaviors $-\Sigma \propto C_s^\alpha$, and $b_0 \propto C_s^{-\beta}$ with $\alpha \in [0.32, 0.4]$ and $\beta \in [0.55, 0.6]$ (see Tables C.12 and Appendix C.4 for complete list of parameters). Interestingly the concentration dependence for the surface charge is fully consistent with a charge regulation behavior, which predicts an exponent of 1/3 [58], pointing to the chemical reactivity of the activated carbon surface. The scaling for the slip length suggests a relationship $b \sim \Sigma^{-\theta}$ with $\theta \approx 1.5 - 1.7$, which is consistent with recent predictions suggesting $\theta = 1 - 2$ depending on the regime considered [68, 106]. Using these scaling laws for the charge and slippage as only ingredients, one can now predict the functional dependence of the enhanced conductivity on salt concentration, as well as that of the zeta potential: this shows a very good agreement with the experimental data for all investigated activated systems, see Fig.6.3.c-d (see also Figure C.8 and C.9). In the end, only 4 parameters are needed to reproduce the data for the enhanced conductivity and zeta potential per channels, with one parameter α being constrained to a value close to 1/3, while the others are consistent between the various activated channels. Note that in contrast to the pristine graphite, the fixed surface potential prediction is less effective for the activated channels, as shown in Fig.6.3.c-e using typical values for the potential ($\Psi_0 \sim -0.2V$). We further performed ionic current measurements using KCl solutions with different pH to investigate its influence on ionic conductivity and zeta potential (see Appendix C.3.6. It appears that activated channels have a higher sensitivity towards acidic pH in line with the chemical reactivity of carboxylic acid (-COOH).

Overall, the data for the various channels with activated graphite are qualitatively consistent between each others – notably in terms of the measured scaling laws for the charge and slip –, with furthermore a semi-quantitative agreement, with only slight differences in the quantitative values for the charges and slip lengths. For example, it is obvious from Tables C.4.1 that, regardless of the channel dimensions, the salinity dependence of conductivity enhancement and zeta potential (electro-osmotic mobility) for System D and System E shows adequate consistency in terms of absolute values and scaling laws which is again well reflected from the salinity dependence of surface charge and slip length values. The similar consistency in salinity dependence of conductivity enhancement and zeta potential values also applies in the case of pristine nanochannel devices System A and System B with different dimensions (Tables B.4.1). However, it is noteworthy that with the same channel height of 10 nm, for any KCl concentration the activated nanochan-

nel device (System D) exhibits significantly high surface charge and zeta potential and, considerably small slip length values compared to pristine nanochannel device (System B). Overall, the activation increases the surface charge by 1-2 orders of magnitude and reduces the slip length by one order of magnitude compared to pristine graphitic surface (Figure C.15). Considering the randomness of surface etching in EBIE and RIE methods, activated carbon surface in our work can be regarded as heterogeneously charged surface. We observe a strong decrease of the slip length with the surface charge on activated surfaces (Figure C.16). Such a behavior was recently attributed to a heterogeneous surface charge distribution [68]. Our theoretical analysis thus enables extracting effective surface properties, which average over surface inhomogeneities, as described *e.g.* by [68,107]. A key finding is that activated carbon surfaces exhibit a unique combination of high charge with significant slip length, on the order of the confinement length scale (Figure C.17).

6.4 Osmotic energy harvesting

Building on these physical insights, we now turn to the ionic response under salinity gradients. We use different KCl concentrations in the two reservoirs in the range 1 – 1000 mM and measure the resulting electric current on the Ag/AgCl electrodes for a variety of concentration ratios, C_{\max}/C_{\min} , keeping the maximum concentration to 1M. Following [55,57], the obtained current is corrected for the contribution resulting from the Nernst potential and originating in the difference in salt concentration at the two electrodes (see Appendix C.2). As shown in Fig.6.4, we observe

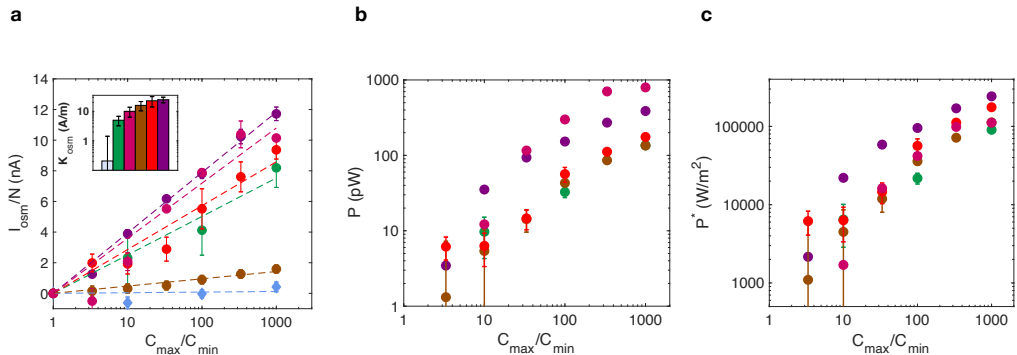


Figure 6.4

Osmotic energy performance of pristine and activated channels. **a**, Osmotic current vs concentration ratio for a pristine channel (System C, blue color diamonds, with channel height 5 nm), and activated channels (System D (green color filled circles), System E (brown color filled circles), System F (purple color filled circles), System G (pink color filled circles) and system H (red color filled circles) with channel heights 10, 3, 5, 13 and 8 nm, respectively) (pH5.5). Measurements are performed by varying $C_{\min} \in [1; 1000]$ mM, while keeping $C_{\max} = 1$ M. Dashed lines are best linear fit. Inset : osmotic coefficient, K_{osm} of, from left to right, pristine (5 nm) and activated (10, 13, 3, 5, 8 nm) channels. Produced osmotic net power (**b**) and single pore power density (**c**) vs concentration ratio. Legend is the same as in panel **a**. Error bars in panels **a**, **b** and **c** are standard deviations from two different measurements at each concentration ratio.

a strong contrast between pristine and activated channels. Within the experimental error, no significant osmotic current is measured for pristine channels. This is in contrast to activated channels, for which a very large osmotic contribution

to the current in the nanoampere range is measured for all investigated devices. We report in the inset the corresponding transport coefficient, K_{osm} , defined as $\frac{I_{\text{osm}}}{N} = \frac{w \cdot h}{L} K_{\text{osm}} \Delta \log[C_s]$. In the following, we will report this current as the 'epi-osmotic current' as it takes its root in a surface (diffusio-osmotic) contribution to the current; K_{osm} will be reported as the 'epi-osmotic mobility'. Diffusio-osmosis is the generation of a water flux occurring in the vicinity of a charged interface in the presence of a solute concentration gradient [57]. The water flux drags the Debye layer which results in the generation of an ionic "diffusio-osmotic" current. A key feature of charged nanopores promoting diffusio-osmotic current is that they do not require selectivity. Further, selectivity of such pores cannot be determined from concentration drop experiments as the fluid velocity is not neglectable. One may rationalize the epi-osmotic current using the same framework as above. According to [67], the epi-osmotic mobility is predicted as

$$K_{\text{osm}} = \left(\frac{1}{2}\right) \times \frac{-2\Sigma}{h} \frac{k_B T}{2\pi\eta\ell_B} \left(1 - \frac{\sinh^{-1}\chi}{\chi} + (1 - \alpha_{ion}) \frac{b_0}{\lambda_D} \frac{\sqrt{1 + \chi^2} - 1}{1 + \beta_s \times \frac{|\Sigma|}{e} \ell_B^2}\right) \quad (6.2)$$

where factor (1/2) applies to the activated surfaces only and stems from the contribution of the bottom layer only; as in the above analysis, the parameters α_{ion} and β_s are zero for the activated surface. For the pristine channels, $K_{\text{osm}} \approx 0$ within our experimental uncertainty. This is actually consistent with the predicted value for the epi-osmotic mobility for a pristine system: using Eq.(6.2) with previous charge and slippage yields $K_{\text{osm}} \approx 10^{-2}$ A/m, hence more than two orders of magnitude smaller than the values for the activated channels, in agreement with the experiments. This huge difference in epi-osmotic mobility between the channels can be understood from the limiting behaviors of Eq.(6.2), which scales as Σ for large charge but as Σ^3 for low charge (Section C.4.2), enhancing the differences between systems with different electrification. We use the previously obtained concentration-dependence of the charge and slip length of the various channels and report in Fig C.14 the predicted plot of the epi-osmotic mobility K_{osm} as a function of the conductivity K of the channels. The agreement between the experimental data for the activated channels and the prediction is good, even more that all parameters – for the charge and slip – were determined from the previous voltage and pressure drop measurements and in view of the sensibility of K_{osm} to small charge differences. This confirms the consistency of all measured mobilities characterizing the activated channels, conductivity, zeta potential and epi-osmotic mobility.

The maximum power generated is expressed as $P = I_{\text{osm}}^2/4G$ with G the channel conductance. Those values, extracted from the concentration gradient experiments, are displayed in Fig.6.4.b. Activated carbon nanochannels can generate almost 1 nW at maximum concentration gradient, only matched by atomically thin MOS_2 nanopore [55]. In order to get a proper sense of the performance of the activated channels in terms of osmotic power, a usual figure of merit corresponds to the generated electrical power per unit surface of the channel. The corresponding single pore power density (osmotic power per unit cross-sectional area) $P^* = \frac{P}{Nwh}$ as a function of the salinity gradient is shown in Fig.6.4.c. Single pore power density for activated channels can reach up to 100 kW/m², which is one to few orders higher than that of measured for boron nitride nanotubes and other single pore fluidic

devices [57, 76, 108, 109] and, comparable with what was obtained with atomically thin MoS₂ nanopores [55]; see comparison of single channel performances in Table C.15.

The phenomena at stake is of particular interest in the context of the energy conversion from the mixing of masses of water with different salinities. Although as much as 0.7 kWh of energy could theoretically be captured per cubic metre of water, the efficiency of energy extraction process remains as to now a fundamental and technical challenge.

6.5 Main insights

Here we show that harnessing epi-osmotic currents on activated carbon is a proper avenue to boost the osmotic energy harvesting from salinity gradients. The single pore figure allows to screen for novel nano-materials with enhanced performances in terms of osmotic energy conversion. One expects however that further factors will affect the osmotic performance when upscaling to macroscopic membranes for large-scale production of osmotic power, such as pore density, concentration polarization and entrance resistance [72, 73]. However, the mechanism of strong electrification of graphite under electron irradiation unveils new avenues to fabricate activated carbon-based membrane at large-scale. See appendix D for scaling of power with number of pores and measurements on GO membranes. Our results on a single or a few carbon channels allow to obtain fundamental insights into the detailed electrification of the surface and the resulting surface properties. One can accordingly reach a predictive framework to describe ionic transport across such channels. We demonstrate that carbon, when properly activated, promotes ionic transport of considerable magnitude. This sheds a new light on the peculiar water-carbon couple. The routes we developed to fabricate activated nanochannels, along with pristine nanochannels, enables the study of bidimensional ionic and molecular transport in nanoconduits with tunable interfacial properties.

Part III
Iontronics

Memristors: artificial memories

A memristor is a passive two-terminal device with a resistance depending on the applied voltage as well as the voltage applied in the past. The word "memristor" is the contraction for memory and resistor because such devices are variable resistors "remembering" their history. They were originally predicted theoretically by Leon Chua in 1971 [110] as the fourth missing electronic element along with resistors, capacitors and inductors. L. Chua concludes his first publication on memristors by writing : "Although no physical memristor has yet been discovered in the form of a physical device without internal power supply, the circuit-theoretic and quasi-static electromagnetic analyses [...] make plausible the notion that a memristor device [...] could be invented, if not discovered accidentally. It is perhaps not unreasonable to suppose that such a device might already have been fabricated as a laboratory curiosity but was improperly identified!" [110]. Thirty seven years later, D.B Strukhov et al. linked Chua's theory with hysteretic current/voltage characteristics displayed by a myriad of nano-electronic devices showing that physical devices behaving as memristors are a reality [111]. Since then memristor research has been growing at a fast pace in particular because of a strong potential for applications. In 2010, Jo et al. showed that memristors are able to store information and perform operations analogously to biological synapses [112]. Following this publication, they have become a major technology enabling brain-like, or neuromorphic, computing. Current computers are approaching their limit because of the separation between memory and processor units known as the Von Neumann bottleneck [113]. However with the development of technologies requiring the processing of very large datasets, like neuron networks, the need for computation power is ever more increasing pushing for a paradigm shift in in the architecture of our computers. Our brain requires an energy intake orders of magnitude lower than computers [114]. Brain like computations relying on memristors are expected to play a role in future's hardware and software technologies [115].

7.1 The fourth missing element

Let's focus briefly on Chua's theory from his 1971 paper [110]. Anyone who had followed an electrical engineering course knows the three fundamental circuits elements : the resistor defined as $R = di/dv$, the capacitor defined as $C = dq/dv$

and the inductor defined as $L = d\phi/di$. Those elements enable linking the four fundamental circuit variables : the current i , the voltage v , the charge q and the flux linkage ϕ . The charge is defined as :

$$q(t) = \int_{-\infty}^t i(\tau)d\tau \quad (7.1)$$

And the flux linkage writes :

$$\phi(t) = \int_{-\infty}^t v(\tau)d\tau \quad (7.2)$$

We thus have three elements and four variables which suggests that, for sake of completeness, one element linking ϕ and q is missing (Figure 7.1.a). This missing element is the memristor. A memristor is defined by the equation :

$$v(t) = M(q(t))i(t) \quad (7.3)$$

With $M(q) = d\phi(q)/dq$ the incremental memristance having the dimension of a resistance. If there is a linear relationship between ϕ and q , $M(q)$ is a constant and a memristor reduces to a simple resistor. However, if the relationship is non linear, one can see that the expression for the incremental memristance, being a function of q , will depend on the current integral (Eq 7.1). Hence, a memristor at $t = t_0$ will behave as a resistor but its instantaneous resistance value (or incremental memristance) depends on the current integral from $\tau = -\infty$ to $\tau = t_0$. Thus the device behaves as a resistor with a memory. In theory, the incremental memristance cannot change if no voltage is applied. Therefore a memristor system is able to retain information through the value of its incremental memristance. We will see in the next sections and in the chapter 9 that it can be slightly different for physical memristor devices.

In 1976, Chua generalized his concept of memristor to a broader class of dynamical systems called memristive systems [116], defined by the following set of equation :

$$y = g(w, u, t)u \quad (7.4)$$

$$\dot{w} = f(w, u, t) \quad (7.5)$$

With u an input variable, y an output variable and w the state variable of the system. Such systems possess memory and do not exhibit capacitive nor inductive effects. Hence no phase shift can be observed. The specificity of a memristive system is that the output is the product of the input and a transfer function meaning that a y - u curve must pass through the origin (Eq 7.4). Chua demonstrated that thermistors, discharge tubes and the Hodgkin-Huxley membrane model [117] are memristive systems.

In this work we focus on one port, time invariant, and electrical systems which allows to rewrite the memristive system equations as [116]:

$$v = R(w)i \quad (7.6)$$

$$\dot{w} = f(w, i) \quad (7.7)$$

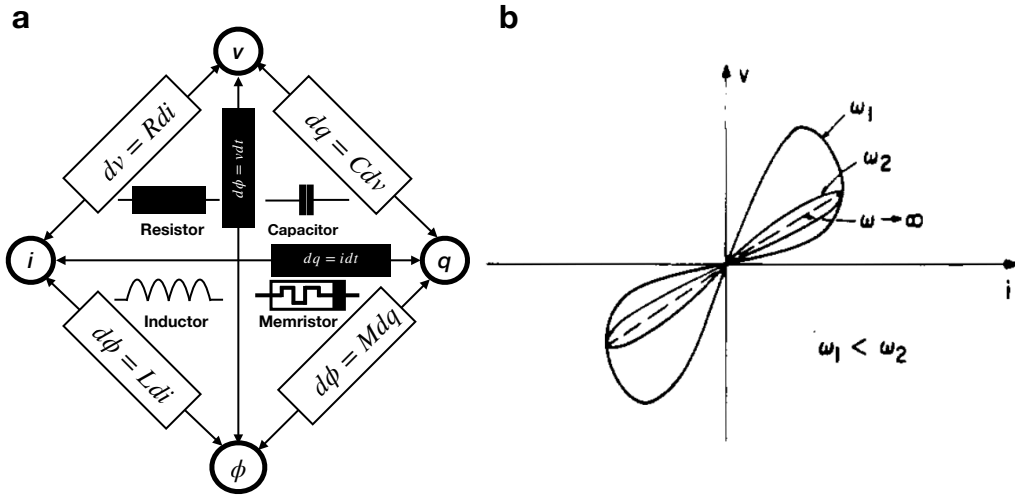


Figure 7.1

The theoretical memristor predicted by Leon Chua. **a**, The fourth missing element. The Four circuit variables as well as the four fundamental elements are represented. The memristor links the flux linkage(ϕ) and the charge(q). **b**, i - v characteristics of a bibs stable memristive device under periodic operation, from [116]. The curve has the form of a pinched loop collapsing on a line at high frequencies.

With i the current and v the voltage.

If we assume an applied periodic current of the the form $i = i_0 \cos(\omega t)$ inducing a voltage periodic function with the same period then, from equation 7.7, w has to be a periodic function with period ω . This implies that R is also and periodic function with period ω and therefore v is the product of two periodic functions. R being of the form $R = R_0 + A \cos(\omega t - \omega_0)$, R_0 and ω_0 being the initial state conditions. The representation of the IV curve is therefore a pinched loop with at most 2 distinct value of v for a given i . If the system has a bounded state variable w regardless of the initial state, the system is said bibs stable. In that case, Chua demonstrated that the loop's area increase with decreasing frequency (Figure 7.1b). At high frequency, the q -integration over time results in calculating an average value and the system's characteristics is linear.

We will now apply Chua's model to a real physical device, made of a biphasic nanometric film. This is the example given in 2008 by D.B Strukhov et al. that enabled linking hysteretic behavior of nanoscale electronic devices to chua's memristive systems [111]. Details about different physical mechanisms enabling memory will be given in the next section. Let's consider a thin semiconductor film device with thickness D placed between two metal contacts serving as electrodes (Figure 7.2.a). The film is divided into two regions: one with a high concentration of dopant and low resistance (R_{on}) and the other with a low dopant concentration and high resistance (R_{off}). The application of an external potential will cause the boudanry between the two regions to move because of the drift of dopant's charge. The boundary

position w is here the system's state variable. Equation 7.6 and 7.7 rewrite:

$$v(t) = \left(R_{on} \frac{w}{D} + R_{off} \left(1 - \frac{D-w}{w} \right) \right) i(t) \quad (7.8)$$

$$\frac{\partial w}{\partial t} = \mu_V \frac{R_{on}}{D} i(t) \quad (7.9)$$

With μ_V the ions (dopant) mobility. Equation 7.9 can be rewritten as :

$$w(t) = \mu_V \frac{R_{on}}{D} q(t) \quad (7.10)$$

And reinjected in equation 7.8 to obtain the memristance (assuming $R_{off} \gg R_{on}$):

$$M(q) = R_{off} \left(1 - \frac{\mu_V R_{on}}{D^2} q(t) \right) \quad (7.11)$$

The simulated response of this model device excited by a sinusoidal voltage is given in Figure 7.2.b. The authors measured experimentally similar behaviors on nanometric TiO_x films. Equation 7.11 implies that the thickness of the film D has to be small for having a non-constant memristance (a constant memristance is equivalent to a classical resistance). This explains why memory effects are mostly observed on nanoscale electronic devices.

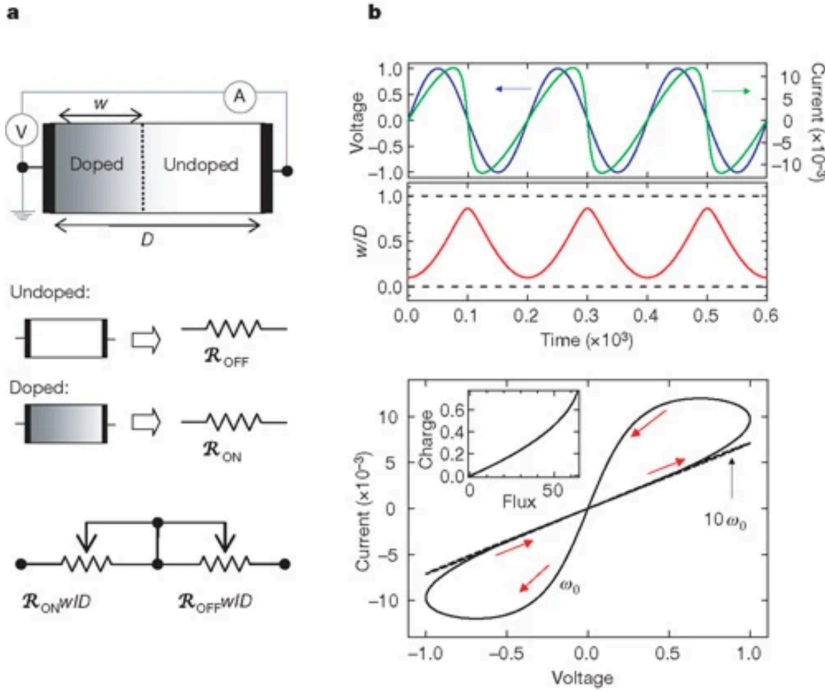


Figure 7.2

The first physical model of a nanoscale electronic device as a memristive dynamic system, from [111]. **a**, Schematic and equivalent circuit. The thin TiO_x film (up) is divided into two regions with a mobile boundary. A potential can be applied via two metallic electrodes and the current is measured with an amperemeter. Each region is equivalent to a resistor with different resistance values (middle). The equivalent electrical schematics is the two resistors in series with their value pondered by their spatial weight (w/D). **b**, System's behavior (simulated) under the application of a sinusoidal voltage. Up: applied voltage (blue) and resulting current (green) vs time. The chosen parameters are : $R_{off}/R_{on} = 160$, $D=10\text{nm}$, $\mu_V = 10^{-10}\text{cm}^2\text{V}^{-1}\text{s}^{-1}$, the applied voltage is of the form $v = v_0 \sin(\omega_0 t)$, with $v_0 = 1\text{V}$ and $i_0 = v_0/R_{on} = 10\text{mA}$. Middle: Boundary position normalized by film's thickness. We note that with the given parameters, w/D never reach 0 or 1. Down: current vs applied voltage for two frequencies. The arrow indicates the loops' direction in time. The curve collapses on a line at $w = 10w_0$. Inset: Charge vs flux linkage. The memristive effect is observed because the relationship is non-linear.

7.2 Solid state and nanofluidic memristors

In this section we describe briefly the operating principles of some relevant memristive devices. This list is far from being exhaustive. A key message of the publication by D.Strukhov et al. is that physical memristive systems are numerous; any dynamical system with an hysteretic response and having no output for a zero input could be part of the list. Such systems were well known even before 2008. For instance, the singing arc, an electromagnetic device used in the end of the 19th century for wireless telegraphy, has been retrospectively qualified as the oldest known

memristor [118]. Today's memristor research relies mainly on solid state devices. Many of them have a metal/insulator/metal (MIM) structure, meaning a thin layer of insulator separates two metallic parts used as electrodes [119]. As an example, we describe below the operation of a MIM memristor relying on the electrochemical metallization mechanism (ECM) presented by Jo et al. [120]. There exists many other kinds of solid state memristors mechanisms such as valence change mechanism (VCM) [121, 122], thermochemical mechanism (TCM) [123] or phase change mechanism (PCM) [124]. Also a couple of ionic nanofluidic memristive devices have been identified experimentally or theoretically predicted [125–128]. We will describe such ion-based memories in more details below.

An ECM memristive device consists of a layer of solid state electrolyte (SSE) insulating media sandwiched between two electrochemical cell electrodes (Figure 7.3.a). The SSE allows displacement of metallic ions and disable electronic transport. The I-V characteristics of such a device is a memristive hysteresis with two well-defined conductance states : an off state with low conductance and an on state with high conductance (Figure 7.3.a). This bipolar behavior is related to the reversible formation of conductive filaments made of silver ions (Figure 7.3.b). Those devices hence relies on a couple ion/electron dynamic and the system's state is related to the ionic spatial repartition (conductive filament formed or not) while electrons play the role of charge carriers.

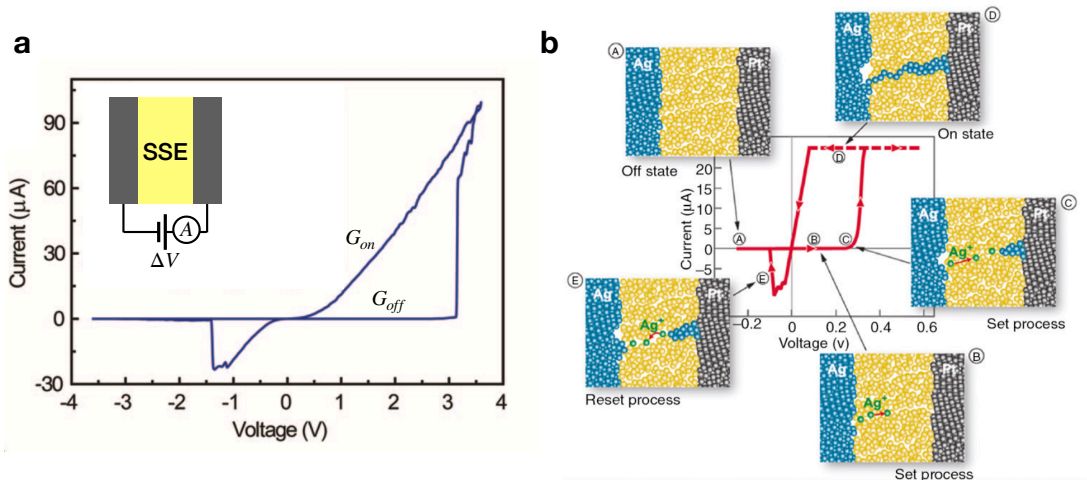


Figure 7.3

Dynamics of the ECM memristive device. **a**, I-V characteristics, from [120]. Inset : schematic of the device. **b**, Electrochemical metallization cell operation, from [129]. When a positive voltage is applied, Ag^+ ions migrate towards the cathode (set process). When a continuous conductive filament links both electrodes the conductance sharply increases (on state). When a negative voltage is applied the ions start moving back towards the anode (reset process). When the filament breaks, the conductance sharply decreases (off state).

We now focus on memristive behaviors observed in nanofluidic systems. It has been reported in a single nanochannel made of PDMS by Zhang et al. [130]. The

authors used immiscible KCl and ionic liquid solutions separated by a well defined mobile boundary to induce the memristive effect (Figure 7.4.a). This is pretty much equivalent to the example described in Figure 7.2. Bu et al. reported a concentration polarization induced memristive effect in an array of glass nanochannels [127] (Figure 7.4.b). Here the state's variable being the concentration gradient between the channel's inlet and outlet. Leong et al. observed a transient memristive effect in a single SiN micropore under 100 fold KCl solution salinity gradience (Figure 7.4.c) [125]. The authors attribute the effect to subtle change in salinity gradience during the voltage sweep. Finally, Sheng et al. observed a memristive effect in a single conical track-etched nanopore using diluted ionic liquid solutions (Figure 7.4.d) [126]. The authors do not provide any interpretation regarding the physical origin of the phenomenon.

Experimental conditions in those reports are slightly unusual. They either take benefit of a concentration gradient/polarization or mixed solutions made of complex salts. Another disturbing shared properties of those reports is the high magnitude of the applied voltages making plausible water splitting effects. An intrinsic nanofluidic memristive effect should be permanent and observable within water's electrochemical window ($V < 1.23V$), ideally on a single pore system, with simple salt solutions. This is relevant for making an analogy with voltage-gated K^+ or Ca^{2+} biological channels.

Recent theoretical predictions and numerical simulations by P.Robin et al. have shown that such an intrinsic memristive effect occurs in 1nm pristine carbon nanochannels (Figure 7.5.a) [128]. This effect takes its roots in the confinement induced enhancement of the ionic interactions' range. Under strong 1D confinement, because the dielectric permittivity of water is much higher than the confining medium's, the range of ionic interaction increases (Figure 7.5.b-up) [131]. At a given distance $r < \xi$, ξ corresponding to the distance over which the electric field remains confined, the interaction between cations and anions are stronger under confinement. This results in the formation of ionic pairs, named Bjerrum pairs, in 1D and 2Dconfinement and ionic strings, named Bjerrum polyelectrolytes, in 2D confinement only [128,132]. The existence of such nanoclusters is predicted to occur in well defined conditions (Figure 7.5.b-down). Pairs are neutral and do not contribute to the current in contrast with polyelectrolites. Above a given applied potential those structures tend to break with a dissociation time τ_d . The resulting single ions contribute to the current which results in an increases of the conductance. When the voltage decreases the pair reforms in an association time $\tau_a > \tau_d$. This means that pairs do not have time to reform and the current is higher for the positive increasing voltages than decreasing ones. This breaking/reformation mechanism is responsible for an intrinsic memory effect. To observe it, the voltage sweep's frequency has to be comprised between $1/\tau_a$ and $1/\tau_d$ roughly. If the sweep is too slow pairs have time to reform and if is too fast they do not have time to break. As shown in Figure 7.2.b the frequency window for observing the effect is 500Hz to 1Mhz. An experimental measurements at those frequencies is difficult because of capacitive effects that results in cuts-off frequencies lower than one hertz with our experimental setup (see appendix D). In my opinion, high frequency measurements are a real challenge and significant efforts in setup and device optimization are required to reduce capacitive effects and perform high frequency ionic transport measure-

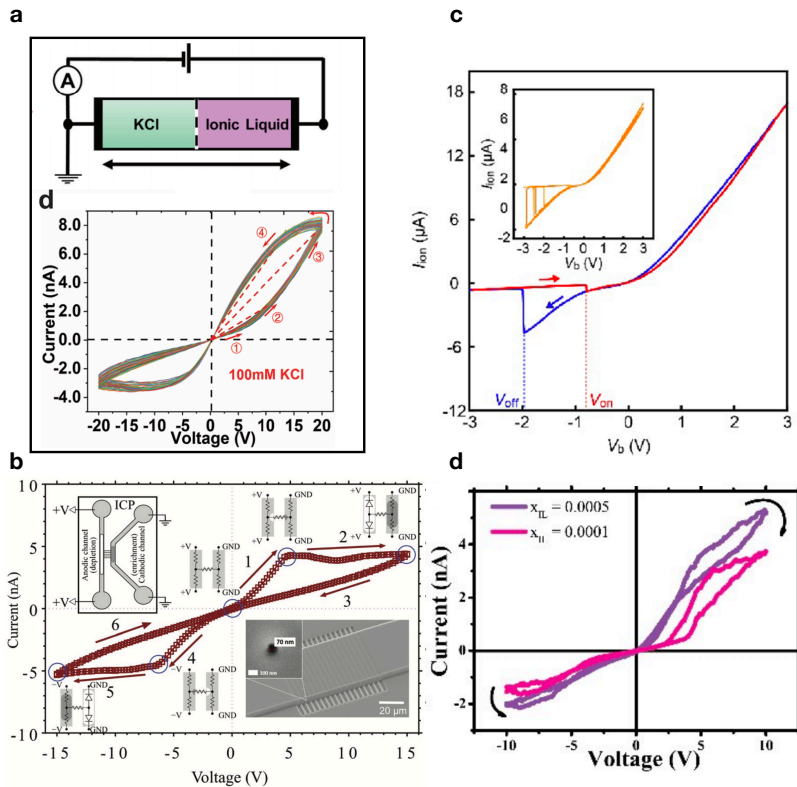


Figure 7.4

Nanofluidic memristive devices. **a**, Immiscible biphasic nanofluidic memristive device, from [130]. Up: sketch of the system. A PDMS nanochannel ($h \sim 100$ nm) is filled with a KCl solution from a reservoir and a solution of ionic liquid on the other. Down: I-V characteristics for 50 sweeps. The high conductance state corresponds to a maximum fraction of KCl solution inside the channel. This is verified by optical observation of the boundary motion using fluorescent dye. **b**, I-V characteristics of a glass nanofluidic channels array ($h \sim 100$ nm) memristive device relying on ion concentration polarization, from [127]. The arrows indicate the sweep direction. Segment 1: the ionic flux is the result of the voltage-induced current enhanced by diffusion flux related to a growing concentration gradient until saturation of the concentration/depletion zones growth at $V = 4$ V. Segment 2: Diffusion-induced current insensitive to the applied bias. Segment 3: relaxation of the ICP with high resistance. Segment 4 to 6 are symmetric to 1-3. The salt concentration is 1 mM KCl. **c**, I-V characteristics with the highest loop area of the SiN micropore (sweep 4), from [125]. The salt concentration gradient is 100 with KCl. Inset: sweep 1 to 5. The memristive effect can only be seen from sweep 2, 3 and 4. **c**, I-V characteristics of the fourth voltage sweep measured in a SiN micropore (1 micrometer diameter) under 100 fold KCl concentration gradient, from [125]. Inset: first to fifth voltage sweeps. The memristive effect transient can only be observed for sweeps 2, 3 and 4. **d** Memristive effect in a track-etched conical nanopore (tip=6 nm) for two mixed ionic liquid solutions (BMIM][BF₄]/water fraction, from [126].

ments with nanochannels. Nevertheless, following this work, we were expecting and looking for a memory effect in carbon nanochannels.

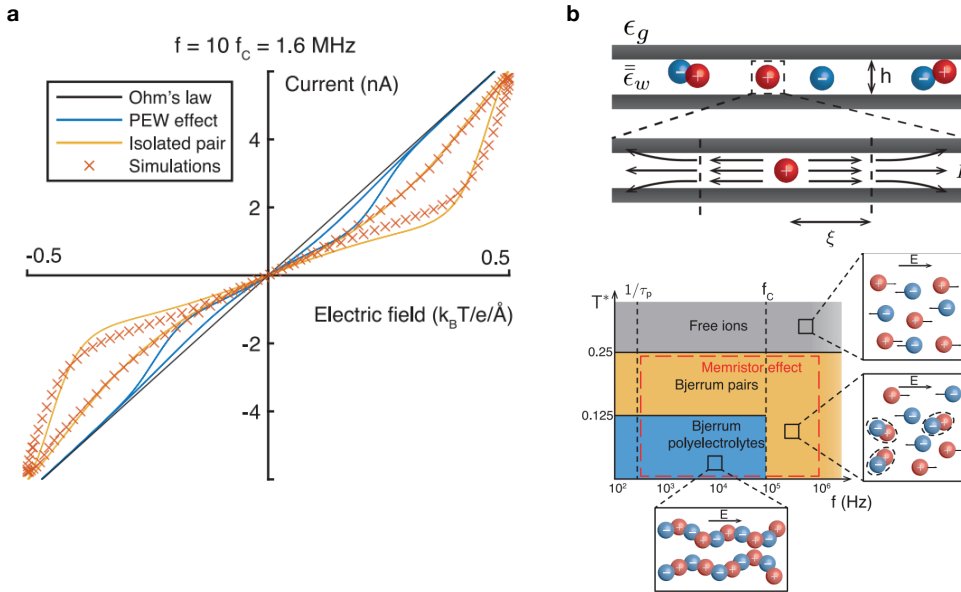


Figure 7.5

Memory effect (theoretical) in pristine carbon nanochannels and physical origin, from [128]. **a**, The memristive effect. The solid lines represent theoretical predictions using Ohm's law, isolated pair or polyelectrolyte Wien effect (PEW). The model for isolated pairs is in good agreement with molecular dynamics simulation at those frequencies. **b**, Formation of ionic nano clusters at high confinement. Up : Modified electric field lines under strong confinement. The lines are parallel to the channel over a distance ξ , meaning that ions of one sign have strong attractive interaction with their neighbor on that lengthscale. Down : Regime map for the existence of ionic nano clusters. The formation of Bjerrum pairs or polyelectrolyte is dependent on an adimensional parameter $T^* \propto \frac{hT}{Z}$ with h the slits height, T the temperature and Z the ionic valence, as well as the frequency of the voltage sweeps. Both type of nano clusters can induce a memory effect.

7.3 Application as artificial synapses

A key characteristic of some memristive devices is that they are in many ways analogous to biological synapses. We give here a (very simplistic) definition of a synapse and their functioning to illustrate their analogy with memristive devices taking inspiration from [133]. A synapse is a connexion between two neurons (Figure 7.6.a). Inside a neuron the information is transmitted via action potentials (or nerve impulse), that are controlled by fine regulations of voltage-gated ionic channels. Action potentials are rapid and localized rise and falls of the neuron's membrane potential that move along the neuron's axon. When a neuron starts emitting an action potential, the neuron is said to "fire". For the information to go from

a neuron to another, the information has to go through a synapse via biomolecules called neurotransmitters. When an action potential reaches a synapse, neurotransmitters are released and travel through the inter synaptic space, called synaptic gap or cleft. When they reach the post neurone, these neurotransmitters initiate various physiological processes in the postsynaptic neuron. For example, in the case of an excitatory synapse, they activate its ion channels, making the postsynaptic fire if it receives enough neurotransmitters.. The amount of neurotransmitters released for a given pre-neurone's action potential is not fixed in time and depends on the synapse's history. Synapses are dynamical systems and their ability to modulate their level of activity is referred to as synaptic plasticity. Synaptic plasticity is considered to be at the root of learning and memory. To give an example imagine a beginner skiing for the first time. During his day on the mountain he will activate some networks of neurons connected via synapses which will make these synapse's stronger (releasing more neurotransmitters for the same stimulation). The next day the neural information will be more efficiently transmitted because of the stronger synapses and the beginner will be more performant : he has learnt. One can make an electrical analogy to synapse (Figure 8.6.a) : they are like a variable resistor connecting two neurons with a resistance value depending on its past stimulations. Synapses can therefore be considered as some particular memristive systems. In 2010, Jo et al. used solid state memristors to mimick biological behaviors demonstrating that some memristors can behave as synapses and are now considered as artificial synapses (Figure 7.6.b) [112,133]. Numerous artificial synapses have since been realized with solid state devices using electrons as charge carrier [115] but the brain's machinery is purely electrolytic. Hence reproducing synaptic functionalities using an ionic system provides a closer analogy to biological synapses.

An important feature of synaptic plasticity is that it can occur on different timescales [133]. After a strong perturbation (stimulus), like the transmission of an action potential, a synapse's level of activity will be modified but takes time to stabilize. On a short time scale, from milliseconds to minutes, the synapse's change of activity level is referred to as short term plasticity (STP). Longer term modifications of synaptic activity, that can last years, are referred to as long term plasticity (LTP). *In vitro* electric current measurements on biological measurements showed that the many-timescale of synaptic plasticity can take the form of a relaxation regime followed by a constant regime, at a value different than its original one (Figure 7.7.a up). This is how biological synapses can keep track of their past stimulus and is a direct observation of what is synaptic plasticity. Hence to reproduce synaptic plasticity realistically an artificial device should show such memory one more than one timescale. This was achieved with solid state memristors (Figure 7.7.a down) [135].

Being able to reproduce LTP opens up many possibilities. This means that it is possible to program the memristor through the value of its conductance. Frequently, the programming capabilities of a memristive devices are highlighted by implementing a most basic learning algorithm (Figure 7.7.b). The device's conductance is permanently increased by applying a high amplitude positive voltage spike (write spike). This induces the long term potentiation mimicking stimulus received by biological synapse. By applying a high amplitude negative voltage spike (erase spike), the device's conductance can be permanently decreased, equivalent to biological long term depression . The device's conductance value can be accessed by applying a short

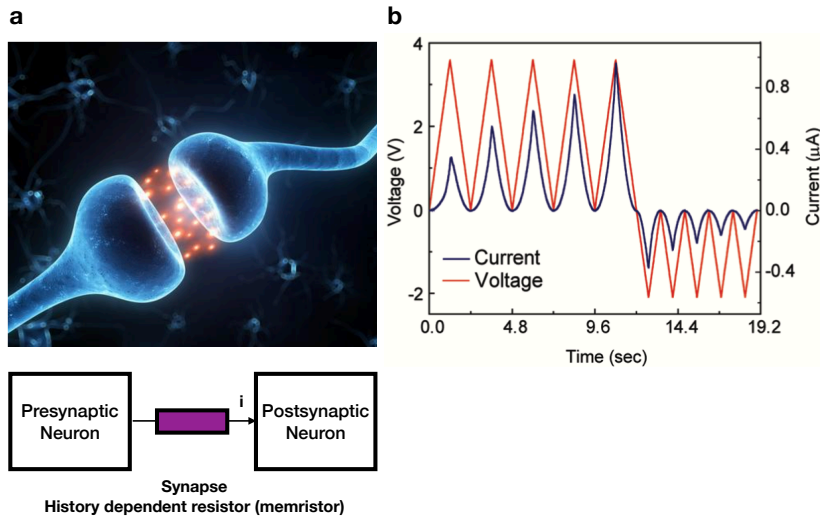


Figure 7.6

Application of memristive systems as artificial synapses. **a**, Up : Illustrative view of a biological synapse, from [134]. Two neurons communicate via a synapse. Neurotransmitters are represented in orange. Down : equivalent electrical schematic. Synapse, because of their plasticity, can be modeled as memristors. **b**, Input voltage and resulting current vs time measured in a Ag+Si/Si solid state memristor, from [112]. Under the application of repeated positive voltage pulses the device's conductance increases progressively (set/learning process). The devices can be reset to its initial state by applying a few negative pulses (reset/forgetting process).

and low amplitude voltage spike (positive or negative) that does not (or very limitedly) change the device's conductance. It is therefore possible to increase/decrease the device's permanent conductance via positive/negative high amplitude voltage pulses and access this value without modifying it with small voltages. A memristive device exhibiting LTP is therefore some kind of hard drive where information can be modified and accessed with voltage pulses. Current hard drive relying on classical Von Neumann architecture can store bits of information that can take the value of 0 or 1. To modify the value of a bit, a transistor located in the microprocessor is required. This is the reason why in traditional computers the memory and the processor are separated in contrast with memristors enabling reading and writing of information. We will see below that this way of storing informations enables to perform operations directly on the memristor device. This is referred to in-memory coding which is an important feature of brain-like computation or neuromorphic computing/engineering.

A very common proof of concept of the computing capacities of memristive devices is the implementation of Hebb's rule or spike timing dependent plasticity (STDP) [112, 133, 135]. Hebb's rule states "Neurons that fire together should wire

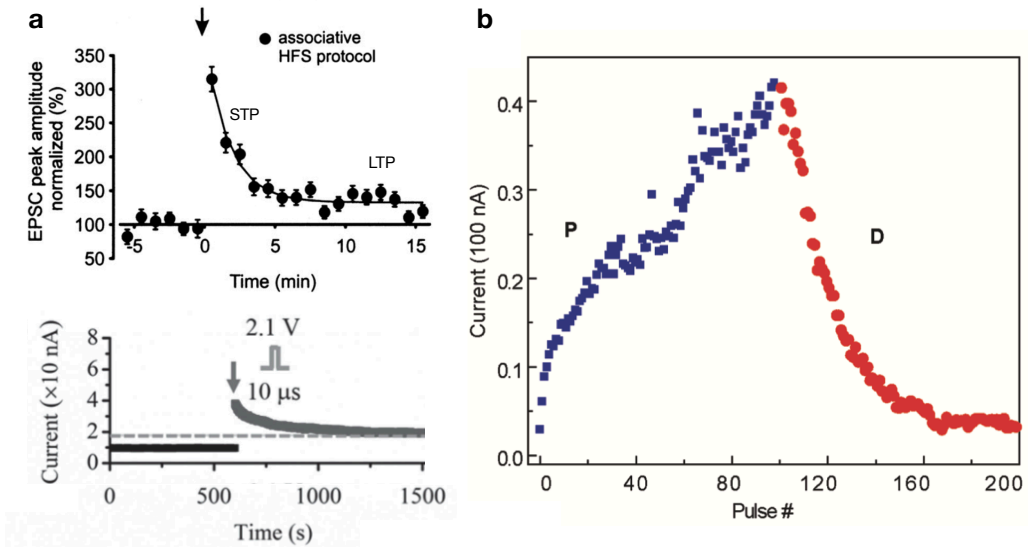


Figure 7.7

Plasticity timescales and use of LTP for learning applications. **a**, STP and LTP measured in a biological synapse and reproduced in an artificial memristive synapse. Up : Excitatory postsynaptic currents (EPSC) vs time in a rat synapse, from [136]. The synapse activity is recorded via patch-clamp amplifier. The current is read by voltage pulse of $1\text{-}8\text{V}\mu\text{s}$ and a duration of 200. At $t=0$ a stimulus consisting of a 200 high frequency voltage pulse of $1\text{-}8\text{V}$. Down : read current vs time in a Pt/WO₃/Pt solid state memristive device, from [135]. The current's value is read by applying a continuous potential drop of 0.05V . At $t \simeq 600\text{s}$ a strong pulse is applied. **b**, Read current vs number of write/erase pulse with a solid state memristive device, from [112]. The conductance is increased by applying 100 potentiating write pulses (in blue with 3.2V in amplitude). The current is read after each pulse with a 1V read pulse. Then the conductance is decreased by applying 100 depressing/erase pulses (in red, -2.8V). Similarly, the current is read between in each pulse with a 1V read pulse.

together". When two wired neuron spike within a short period of time, their synaptic connection is strengthened or weakened depending on the firing order (Figure 7.8.a). If a presynaptic neuron fires just before the postsynaptic neuron ($\Delta t > 0$ and close to 0) the synapse's level of activity is strongly decreased. If a presynaptic neuron fires long before the postsynaptic neuron ($\Delta t \gg 0$) the synapse's level of activity is weakly decreased or left unchanged. If the postsynaptic neuron fires just before a presynaptic neuron ($\Delta t < 0$ and close to 0) the synapse's level of activity is strongly decreased. If a presynaptic neuron fires long before the post neuron ($\Delta t \ll 0$ and small) the synapse's level of activity is weakly increased or left unchanged.

To implement such behavior on a memristive device, an algorithm has to be developed that models Δt into an input high amplitude voltage $U(t) = f(\Delta t)$ corresponding to an event (both neuron fires with a time interval Δt). The change of synaptic's level of activity, or $\Delta\text{Synaptic weight}$ is measured with read spikes (Figure 7.8.b). Jo et al. modeled the event as a single pulse of high amplitude

with a width (time duration of the pulse) being an exponentially decaying function of Δt (Figure 7.8.c) [112]. Since this publication, STDP have been reproduced many times, in particular efforts have been made to use more bio-realistic input voltages [137–139]. Yet implementation of STDP demonstrate the in-memory computing capabilities of a memristive device.

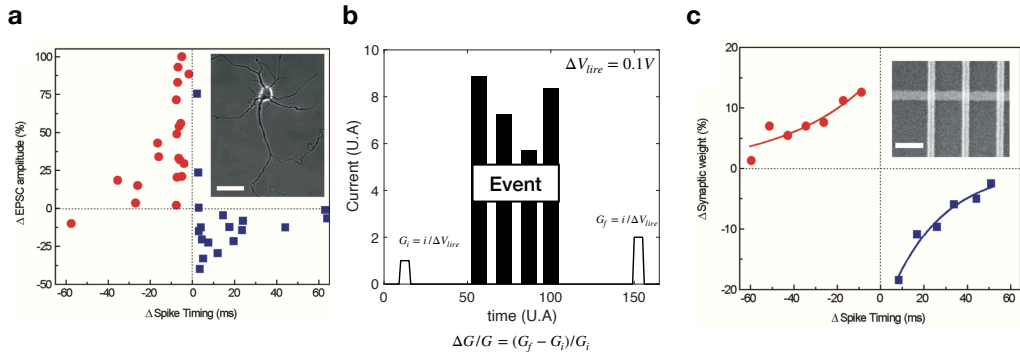


Figure 7.8

STDP and its implementation on a memristive device. **a**, "Measured change in excitatory postsynaptic current (EPSC) of rat hippocampal neurons after repetitive correlated spiking (60 pulses at 1 Hz) vs relative spike timing", from [112]. Scale bar: $50 \mu\text{m}$. **b**, Illustration of STDP implementation. The conductance $G = I/\Delta V_{read}$ is read before and after the input voltage is applied and is equivalent to $\Delta G/G$. The event is modeled with high amplitude spikes that modify the device's conductance. An algorithm has to be developed to emulate relative spike timing into voltage spikes. **c**, Change of synaptic weight ($\Delta G/G$) vs emulated spike timing in a solid state memristive device, from [112]. The event is modeled with a single pulse with a width (duration) being an exponentially decaying function of Δt . Hence when Δt is small the writing pulse has a long duration which modifies a lot the device's conductance and when Δt is large the writing pulse is short and the conductance is weakly modified.

For real world application purposes, memristive devices can be used as elementary brick of so-called cross bar arrays memristive chips (Figure 7.9.a-b) [133, 140–143]. In those chips electrodes play the role of a neurone and memristor elements are behaving as synapse adjusting the connectivity between two neurons. Such chips are sometimes referred to as artificial neural networks (ANN). They can performed complex tasks such as image processing (Figure 7.9.c). Those neuromorphic technologies do overcome the von Neumann architecture's limitations and are expected to play a role in the future for hardware technologies.

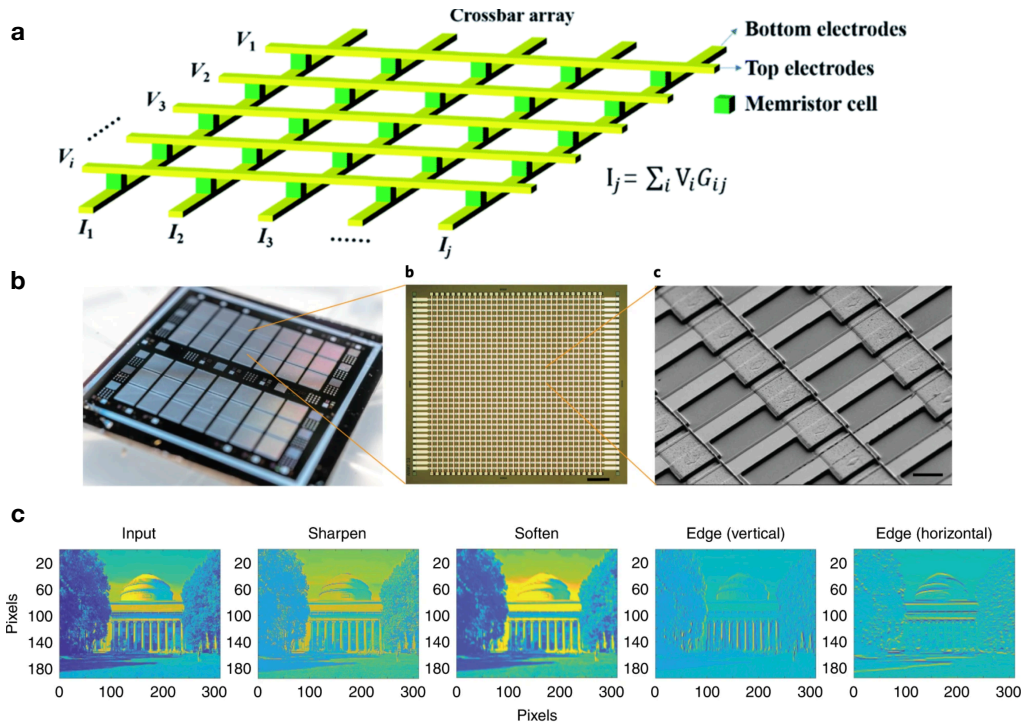


Figure 7.9

Artificial neural networks with memristors. **a**, Schematic of a crossbar array, from [143]. The equation, obtained from Kirchoff's law, gives the current on each bottom electrode, G_{ij} is the conductance of a given memristor cell. Such vector matrix multiplication is at the root of ANN computing [143]. **b**, Image of a Ag-Cu alloy memristor chip, from [141]. Left : photography. Middle : Optical microscopy. Scale bar : 240 microns. Right : SEM image with crossbar structures visible. Scale bar : 15 microns. **c**, Image processing with the memristor chip displayed in **b**, from [141]. The image is a photography of MIT Killian's court. An input image (left) is post-treated in four different ways.

Results: Memory effects in bidimensional carbon nanochannels

Memristors are electronic devices enabling both information storage and in-place processing. They are at the core of many recent, bio-inspired attempts of overcoming the challenges faced by modern computers, from energy consumption to computation time [112, 119, 139, 142]. However most of these devices relies on solid-state technologies to operate, in contrast with the brain's purely electrolytic machinery. Here we report a novel memristor effect in single-digit bidimensional ionic channels using simple salts solutions and low voltage. We show that these nanofluidic memristors have hour-long memory and rationalize our results in term of an accumulation of ions inside the channel due to its asymmetric entrance. Our results could serve as foundation for biomimetic iontronics applications.

8.1 Motivation and methods

Over the past decade, research in nanofluidics has shed the light on many unconventional phenoma arising in the transport of ions through nanometric channels [27, 32, 53, 132, 144, 145]. The field has grown at a fast pace, in particular because of its potential for a wealth of applications, from water desalination [146–148] to energy havesting [43, 44, 55, 57]. Most notably, the development of bidimensional carbon-based channels made by van der Waals assembly have enabled the study of nanoscale ionic transport with unmatched versatility in terms of geometry or surface properties [24, 26, 27]. Very recently, it was predicted that such systems exhibit short-term memory [128], a phenomenon known as memristor effect – but this has until now eluded experimental inquiry.

A memristor – short for memory resistor – is a resistor with an internal state that is susceptible to change depending on the history of voltage seen by the system, thereby modifying its conductance. As this makes them the analogues of biological synapses, they have drawn considerable attention, but most of existing examples

This part of the project is in collaboration with the angstrom-scale fluidic group of Manchester university. They also observe memory effects in pristine nanochannels. However those results are not displayed here regarding the stage of the work. The modeling is from P.Robin who also participated in the writing.

are based on a metallic-insulator-metallic (MIM) architecture and function with coupled ion and electron dynamics. While a handful of nanofluidic memristors were also designed, they all require high applied voltage to operate, above the water splitting threshold (1.23 V) [125–127, 130]. They also exceed the dimensions of biological systems, or use ionic liquids. Here, we report an intrinsic memory effect of carbon nanochannels below 10 nm, by using simple salts in water and applying voltage below 1 V (Fig 8.1.a).

In this work, we focus on recently developed bidimensional carbon nanochannels, which can be fabricated through two different protocols. For “activated” nanochannels, a through hole and one or a few trench connected to the hole are etched into a bottom graphite crystal (Fig 8.1.b). This is done by electron beam induced etching (EBIE) inside an environmental scanning electron microscope (SEM). Secondly, this pattern is covered by a top layer graphite crystal. Finally, this bilayer heterostructure is transferred above a Si/SiN window presenting a circular aperture in its center. On the other hand, “pristine” nanochannels are fabricated by separating two graphite crystals by an array of thin graphite nanoribbons called spacers. The latest are fabricated from a graphite crystal using electron beam lithography followed by reactive ion etching. This whole assembly being placed on a SiN window presenting a rectangular aperture. Further details regarding the fabrication of pristine and activated channels can be found in chapter 2 and 3, respectively. While similar in design, they differ on a few key properties. The height of pristine channels can be precisely controlled in increments of approximately 0.35 nm, and here down to 0.7 nm – The channel’s depth corresponding to the spacer’s thickness. Conversely, activated channel’s depth is controlled by EBIE with a resolution limited to a few nanometers. However they bear a much stronger surface relative to pristine channels following the exposure of their bottom wall to the electron beam (see Chapter 6 and Appendix C). Here, we use activated devices with 1, 3 or 4 channels of depths between five and thirteen nanometers.

The memristor effect is best probed with a sinusoidal voltage and measuring nonlinearities in the current response of the system, depending on frequency and other parameters. We use a voltage drop of amplitude 0.8 – 1 V and frequency between 1 and 100 mHz across a carbon nanochannel separating two reservoirs filled with an electrolytic solution (Fig 8.1.a). Measurements are performed with electrolytic solutions of potassium chloride (KCl), calcium chloride (CaCl₂) and aluminium chloride (AlCl₃) with concentrations varied between 1 mM and 1 M. Immersed Ag/AgCl electrodes connected to an amplifier (*KEITHLEY* 2400) are used to apply the voltage drop and measure the resulting ionic current. All our measurements are sampled at 2 Hz. All the raw data and analysis are presented in supplementary materials.

8.2 The memory effect

In sinusoidal regime, the IV characteristics of our devices take the form of loops pinched at the origin (Fig 8.2.a), a key feature of memristors. This can also be visualized as a hysteresis loop in conductance (Fig 8.2.b), showing the bistability of the devices. The conductance is found to increase at positive voltages and decreases at negative ones (Fig 8.2.a). When frequency is increased, the loop shrinks as the system spends less time under a voltage of a given sign.

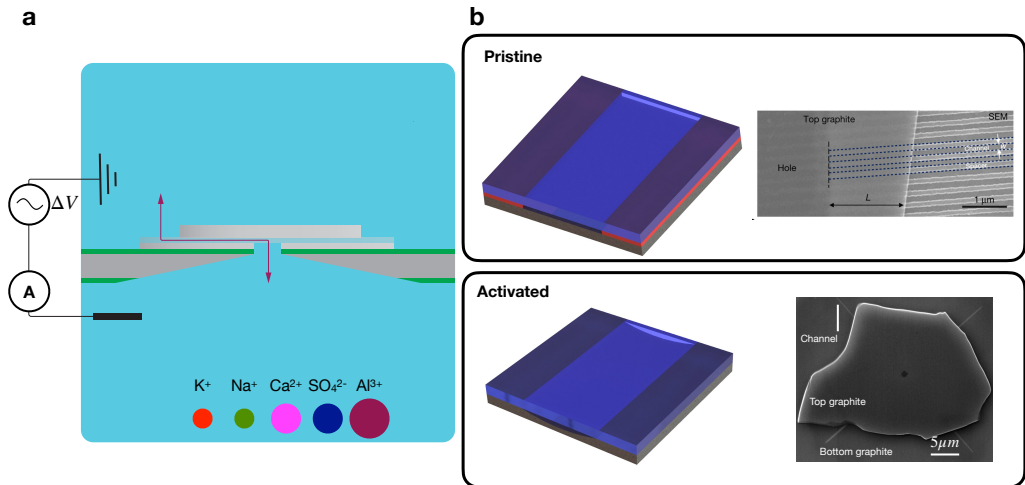


Figure 8.1

Experimental setup. **a**, Nanofluidics measurement cell and ionic library. A carbon nanochannel separates two reservoirs filled with an electrolytic solution. The red arrow indicates path taken by water molecules and ions. **b**, Carbon nanochannel devices. Left : Schematics (for pristine nanochannels spacer are drawn in red). Right SEM images (for pristine nanochannels from [23])

This loop is obtained by plotting the instantaneous conductance $G^*(t)$, defined as $G^*(t) = I(t)/U(t)$, versus the applied voltage $U(t)$ (Fig 8.2.b). Rather than giving an accurate physical value of the conductance, the use of the instantaneous conductance enables to quantify the strength of the memristive effect for various experimental conditions. Under the application of a sinusoidal voltage the system oscillates between an “on state”, corresponding to a high conductance and an “off state” corresponding to a low conductance. We use the instantaneous conductance ratio G_{on}^*/G_{off}^* as a metric to quantify the conductance range, or rectification. The normalized loop area $A^* = A_{loop}/G_{on}$ is also extracted as an indicator of the switching dynamics. A noticeable difference with many solid-state memristors is the absence of a voltage threshold above which the conductance change occurs. This is confirmed by single-pulse hysteresis loop that showed conductance ratio of up to thirty at frequencies lower than 1mHz (see supplementary information). Finally, the switching effect is observed down to very low frequencies, corresponding to memory timescales up to one hour and pointing to a lasting memory.

To obtain further fundamental insights on the phenomenon, we study the dependence of the instantaneous conductance ratio with ionic species, concentration and channel height. We notice a strong dependence of the memristive effect on ion concentration and nature of salt (Fig 8.3.a-b). The strongest effects can be observed with multivalent ions at low salt concentration (see also appendix D).

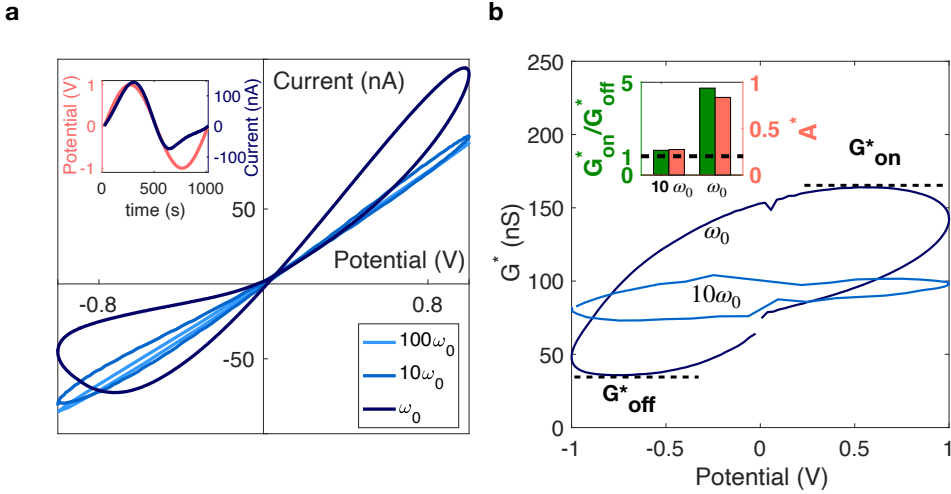


Figure 8.2

The memristive effect. **a**, Current-voltage characteristic at various frequencies. The frequency ω_0 is 1 mHz. Inset : Current and applied voltage as function of time at 1mHz. The salt used is AlCl_3 at 10mM. System A ($h \sim 5\text{nm}$). **b**, Instantaneous conductance as function of applied voltage extracted from **a**. Only sinusoidal voltage with frequency ω_0 and $10\omega_0$ are represented for greater clarity. The diverging points around $U = 0\text{V}$ have been manually removed. Inset : Instantaneous conductance ratio and normalized loop area for sinusoidal voltage with frequency ω_0 and $10\omega_0$. The area above the dashed line is where the memristor effect can be observed.

We now propose a simple model accounting for the observed long-term memory. See appendix F for the detailed derivations. The existence of rectification in the current-voltage characteristics (Fig. 8.3) shows that, depending on the sign of the applied voltage, an accumulation or depletion of ions can occur within the channel. Since positive voltage results in a high conductance (accumulation) and a negative one in a low conductance (depletion), this suggests there must be some asymmetry within the system. The simplest model accounting for this is a 3-state model where particles can either be in the left reservoir, the right reservoir, or inside the channel (Fig. 8.4.a). We assume that the concentrations of the two reservoirs are fixed to c_L and c_R , respectively, with $c_L \gg c_R$. Particles can hop from one site to the next through a diffusion process, or by being advected by an external force f . For a positive forcing, particles go from the concentrated side c_L to the dilute one, causing an accumulation of particles inside the channel, and vice-versa for a negative forcing. This model can be solved analytically, and the resulting current-voltage characteristic exhibits rectification (Fig. 8.4c). However, under time-varying forcing, the system does not display any kind of memory beyond diffusion timescales.

However, this picture changes sensibly when surface effects are considered. If one adds a fourth site to the model, where particles can be adsorbed with rate k and desorbed with rate λ (Fig. 8.4b), then the system is able to keep memory of its

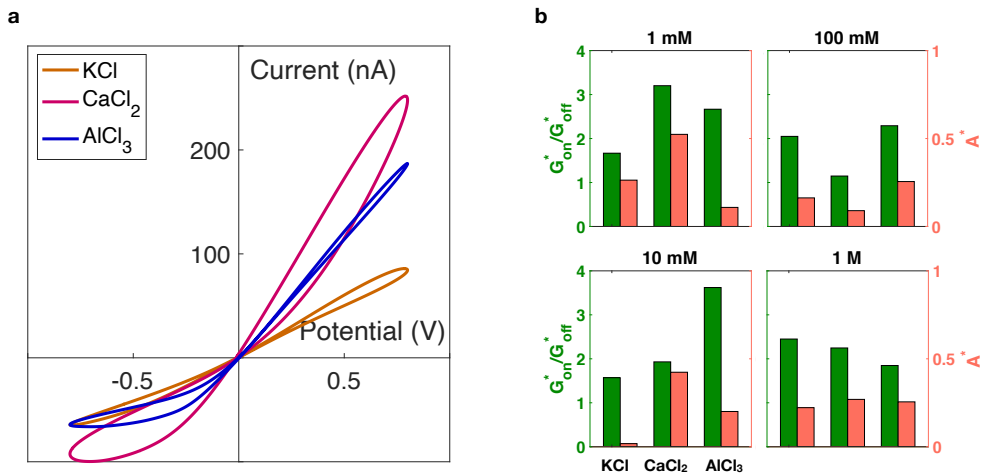


Figure 8.3

Influence of the nature of the salt. **a**, Current-voltage characteristic at 1mHz, for various types of ions. The salt concentration is 1mM, for a channel height of $h \sim 13$ nm. **b**, Instantaneous conductance ratio for various salts and concentrations, for the same nanofluidic system at frequency 1mHz.

past through the number of adsorbed particles at a given time. This model can again be solved analytically, and we show in the Supplementary Materials that, in the limit of large surface effects ($k \gg \lambda$) it behaves as a memristor with typical memory time:

$$\tau_m \sim 2\pi \frac{k}{\lambda} \tau_d, \quad (8.1)$$

where τ_d is the diffusion time across the system. In that case, the sinusoidal-regime characteristic opens up in a loop pinched at the origin (Fig. 9.4c), a hallmark of the memristor effect.

This minimal model can be used to clarify the mechanism behind the nanofluidic memristor. While we use reservoirs with same concentration c_0 , the entrances of the nanochannel are asymmetric. Schematically, one can assume that this geometrical asymmetry induces a difference in the energetic cost of going through either entrance: E_L to enter from the left, E_R from the right. One can then model our system with a 3- or 4-site model with reservoir concentrations $c_i = c_0 e^{-E_i/k_B T}$. Bidimensional nanochannels are known for very large surface charges (chapter 6), which can be quantified through the Dukhin number:

$$\text{Du} = \frac{\Sigma}{ech}, \quad (8.2)$$

with Σ the surface charge, e the elementary charge, c the concentration and h the channel height. For activated channels, one can typically find $\text{Du} \sim 10^3$ and $\text{Du} \sim 10^2$ for pristine channels. In the 4-site model, the Dukhin number can be

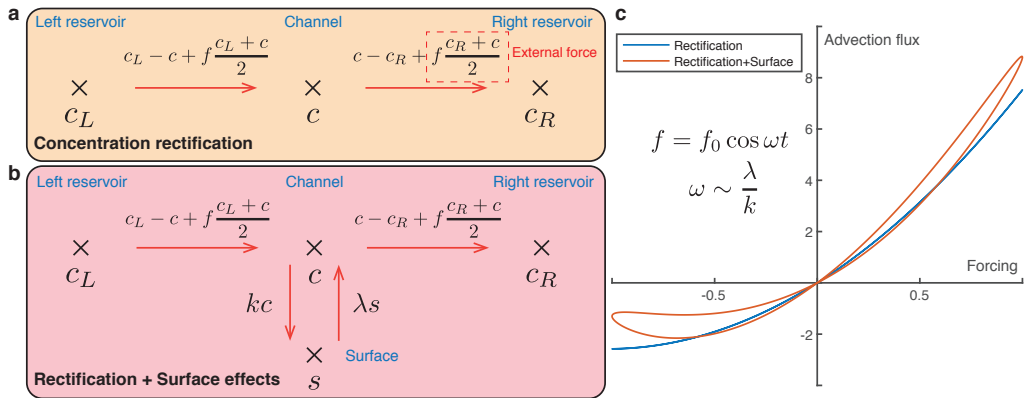


Figure 8.4

Massive surface charge as a source of long-term memory. **a**, Minimal model of concentration rectification inside a nanochannel. Two reservoirs impose concentrations c_L and c_R to the channel. Depending on the sign of the forcing f , the channel is either depleted or filled with particles. **b**, Minimal model of nanofluidic memristor effect. The surface of the nanochannel adsorbs particles at a rate k and frees them with rate λ . This process slows down the system's dynamics and induces a memory effects on a timescale of the order of λ/k times a diffusion timescale. **c**, Advection flux of particles across the system in absence or presence of an absorbing surface, as function of external forcing (dimensionless units). In the regime of massive adsorption ($k \gg \lambda$), long-term memory effects can be observed.

defined as:

$$Du = \frac{k}{\lambda}. \quad (8.3)$$

In other words, the 4-site model suggests that the memory timescale of 2D nanochannels is:

$$\tau_m = 2\pi Du \frac{L^2}{D}, \quad (8.4)$$

with D the diffusion coefficient of ions and $L \sim 10 \mu\text{m}$ the length of the channel. For activated nanochannels, we thus obtain $\tau_m \sim 10 \text{ min}$, accounting for our observations of the nanofluidic memristor.

8.3 Main insight

Bidimensional carbon nanochannels exhibit persistent memory, resulting in a hysteretic conductance known as memristor effect. We rationalized this phenomenon as arising from current rectification due the systems' asymmetry and the specific surface properties of these systems, and proposed a minimal model reproducing their phenomenology. Notably, we find that slow dynamics and long memory timescales emerge as soon as surfaces dominate the bulk. In addition, the properties of our nanofluidic memristors can be varied through the use of different ionic species, concentration and channel heights, offering great tuneability. Their ability to function using ions only, within the electrochemical window of water and with a total volume

below $10^{-1} \mu\text{m}^3$ paves the way for manifold developments in iontronics, and allows to take inspiration from biological systems.

Results: Long-term memory and synapse-like plasticity of activated carbon nanochannels

Fine-tuned ion transport across nanoscale pores is key to many biological processes such as the process of information in the brain [12, 149, 150]. Such advanced functionalities are still far outside the reach of bio-inspired nanofluidic systems. However, a milestone has been reached very recently with the design of nanoscale carbon-based slits whose conductance exhibits long-term memory (Chapter 8). Here, we show that their plastic memory properties can be harnessed to mimick that of biological synapses. We found that their conductance can be reversibly increased or decreased by application of short voltage spikes, reproducing the long-term potentiation and depression of neuron connexions. In addition, we designed a experiment implementing a basic form of Hebbian learning, where the system's conductance is updated according to the relative activation times of two neurons. We anticipate these results will allow for the implementation of more complex learning tasks and in-memory computing using ion-based nanofluidic devices.

9.1 Motivations and methods

In recent years, major advances have been made in the control of both water and ion transport at the nano-, and even subnano-scale. Novel nanofluidic systems now allow to reproduce some of the basic functionalities of biological channels, such as ion selectivity [151, 152] or mechanosensitivity [32, 144]. While artificial membranes still cannot compete with their biological counterparts, high hopes have been placed in carbon-based channels, such as carbon nanotubes and graphite slits, which harness the peculiar interaction of water with carbon surfaces [81]. Notably, two-dimensionnal channels built through the van der Waals assembly of graphite crystals have been found to exhibit a history-dependent conductance that can be modulated by applying a time-varying voltage (chapter 8).

This part of the thesis was done with Paul Robin who designed the algorithm for the implementation of Hebb's rule and participated in the writing.

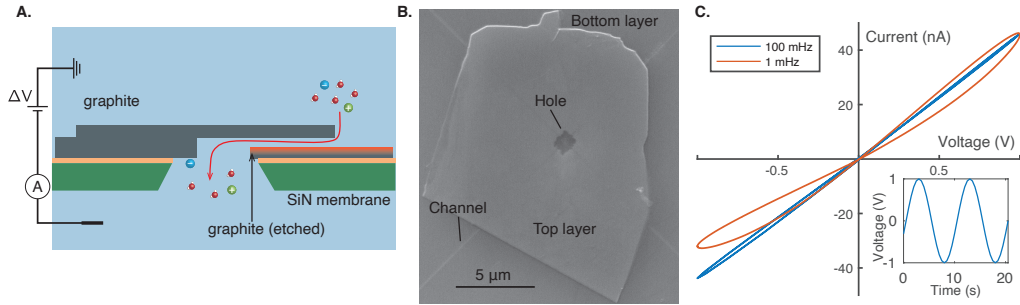


Figure 9.1

Memristor effect in activated carbon nanochannels. **A.** Experimental setup, as detailed in Chapter 6-8: the nanofluidic device is clamped between two reservoirs filled with a 1mM calcium chloride aqueous solution. **B.** SEM image of an activated carbon nanochannel. Four perpendicular trenches of 8 nm in depth are visible in white. The hole pierced in the bottom layer is visible through the top layer. **C.** Current-voltage characteristic of the nanofluidic device under a sinusoidal voltage $\Delta V = U_0 \sin 2\pi ft$. At frequencies lower than 100mHz, the curve forms a self-crossing loop at the origin, a phenomenon known as a memristor effect. Inset : applied voltage.

Such systems, known as memristors (short for memory resistors), serve as elementary components to build new computing devices inspired by the brain. One of their key properties is their ability to store information in the value of their conductance. Another is the possibility of performing a basic operation (ie., the multiplication of a conductance with a voltage through Ohm's law: $I = GU$) without the need of transporting data to an external processor, a principle referred to as in-memory computing. These two qualities make them the electronic analogues of synapses, which play a central role both in learning and information processing. However, memory effects in synapses take place on a wide range of timescales from milliseconds to years – with for example the build up of calcium fluxes in the short term and structural changes over long times. While some memristors are able to emulate these multi-timescale dynamics [135, 137, 153], they are made of solid-state devices, relying on the transport of electrons rather than ions like biological neurons.

This calls for the implementation of basic learning tasks using carbon-based nanochannels, demonstrating the computing capabilities of nanofluidic systems. Here, we show that two-dimensionnal graphitic channels introduced in chapter 3 can serve as artificial synapses, in that they reproduce some basic properties found in biological neuron networks.

These systems consist of a bilayer van der Waals heterostructure (Chapter 3) where four trenches have been etched into a pierced graphite crystal ('bottom layer', of thickness in the range 50 – 100 nm), and covered by a second graphite flake ('top layer', of thickness around 50 nm). The trenches are obtained via electron beam induced direct etching (EBIE) using an environmental scanning electron microscope (SEM) and are typically 5 to 10 nm in height. This assembly is deposited onto a pierced silicon nitride (SiN) membrane separating two reservoirs filled with an electrolytic solution of CaCl_2 (1mM), see Fig. 9.1A and B. They contain sub-

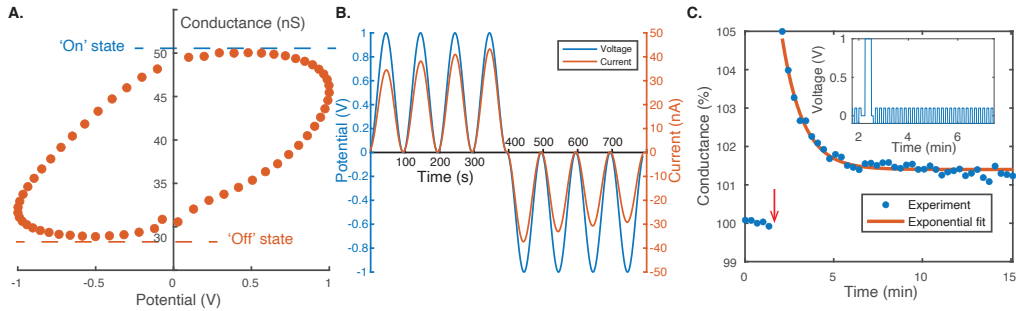


Figure 9.2

Conductance plasticity and short- and long-term memory effects. **A.** Hysteretic conductance cycle under a sinusoidal voltage, corresponding to the red curve in Fig. 1C. **B.** Evolution of the ionic current (red) under voltage pulses of constant sign (blue). Positive (resp. negative) pulses result in a increase (resp. decrease) of conductance. **C.** Conductance change following a positive voltage pulse, exhibiting both short- (< 2 min) and long-term (> 15 min) memory. The conductance is read by applying a weak square voltage wave that has no sensible impact on the state of the system. Inset: applied voltage as function of time. A strong positive voltage drop is applied for 15 seconds, and then the evolution of the conductance is tracked by measuring ionic current while a weak square voltage wave of zero mean is applied. The red arrow indicates the beginning of the voltage spike. The red curve is a fit of experimental data with an exponential decay (with the end of the spike as origin of time). The decay time is found to be 1.2 minutes, setting a scale for short-term memory effects.

merged Ag/AgCl electrodes, connected to an amplifier (KEITLHEY 2400) inducing a controllable voltage drop and measuring the resulting ionic current. Further details concerning the nanofabrication and nanofluidic measurements can be found in appendix G.

Owing to their unique properties combining a very high surface charge and the low carbon-water friction (Chapter 6), activated carbon nanochannels exhibit novel transport phenomena, and most notably behave like nanofluidic memristors when a time-varying voltage is applied. The ionic current is stronger when the potential drop is ramped down from $+1$ V to -1 V than when it is ramped up between the same two values. This causes the current-voltage characteristic to open up in a eight-shaped loop pinched at the origin (see Fig. 9.1C), a hallmark of memory effects [116, 154].

9.2 Characterizing the ionic memory

At the microscopic level, this effect can be seen as the system switching between two conducting states in a hysteretic cycle (see Fig. 9.2A). Applying a pulse of positive voltage shifts the system towards an 'on' state of high conductance, and a negative pulse towards a low-conductance 'off' state (Fig. 9.2B). The device thus keeps track of past voltage through its conductance state, which acts as an internal memory.

However, contrary to most existing, solid-state memory devices, our nanofluidic

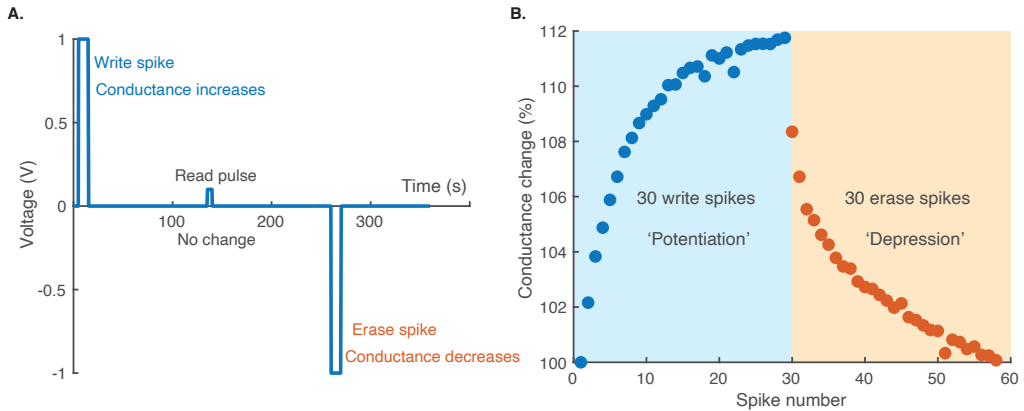


Figure 9.3

Reversible, long-term strengthening of a nanochannel’s conductance for in-memory coding. **A.** The system’s conductance can be increased by applying a ‘write’ spike (+1 V, 10 seconds) or decreased with an ‘erase’ spike (−1 V, 10 seconds). It can be read off through a weak, non-intrusive ‘read’ pulse (+0.1 V, 5 seconds) that does not modify the conductance value. **B.** Long-term modification of a nanochannel’s conductance. 30 write spikes are applied, followed by 30 erase spikes which bring back the system to its initial state. Between each spike, the conductance is let to stabilize during two minutes and is then measured with a read pulse.

memristor exhibits both short- and long-term memory, as shown on Fig. 9.2C. After a short positive voltage pulse, the system’s conductance abruptly switches to a high transient value, before relaxing within a few minutes to a value slightly above its initial state. This conductance change is then stable over hour-long timescales, but is fully reversible by applying a voltage pulse of opposite sign.

These features are remindful of some of the basic functionalities of biological synapses. These neural connections act as resistors whose conductance can be tuned during learning processes, with reversible modifications both on short (on timescales from milliseconds to minutes [155]) and long (from minutes to years) timescales [156]. The latest, known as long-term potentiation (or depression, when the conductance is lowered) enables the storage of information through the synapse’s conductance state as a form of in-memory coding.

9.3 Programming the conductance

Taking inspiration from these traits, we design a protocol to implement in-memory computations with our nanofluidic channel (Fig. 9.3A). We increment the system’s conductance by applying a ‘write’ voltage spike (+1 V during 10 seconds). The conductance can then be accessed to via a ‘read’ pulse (+0.1 V during 5 seconds), which does not perturb sensibly the value of the conductance. It can also be reseted to its original value with an ‘erase’ spike (−1 V during 10 seconds). This allows for the easy, reversible modification and access to the stored value for computational applications. As a proof of concept, we show in Fig. 9.3B that the modification process

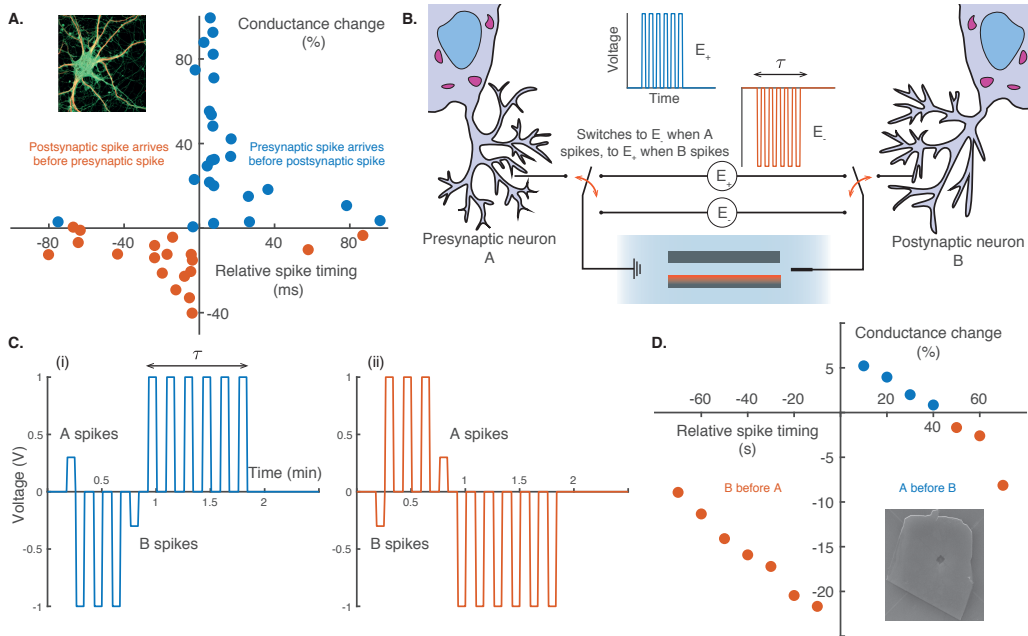


Figure 9.4

Implementation of Hebb's law using carbon nanochannels. **A.** Hebb's law in biological synapses: a synapse's conductance is increased (resp. decreased) when its presynaptic neuron fires just before (resp. after) the postsynaptic one, adapted from REF. This implements a form of causality detection, known as spike-timing-dependent plasticity (STDP). Inset: rat hippocampal neuron, from [157]) **B.** Hebb's law with nanofluidic memristors: voltage spikes are applied to a nanochannel, mimicking the activation of two neurons A and B. After each spike from the presynaptic (resp. postsynaptic) neuron, a series of erase (resp. write) spikes is applied. **C.** Example of voltage spikes series depending on whether the presynaptic (i) or postsynaptic (ii) neuron activates first. **D.** Conductance change after 8 successive activations of the two neurons, in percentage of the initial conductance and as function of the relative activation timing of the neurons. Inset: see Fig. 9.1B.

is indeed fully reversible and allows to store an analog variable over long timescales, by applying a series of 60 write and erase spikes. We thus demonstrate that carbon nanochannels can be 'programmed' through the tuning of their conductance, enabling the implementation of in-memory operations with ion-based nanofluidic systems.

9.4 Implementation of Hebb's rule

Building on the similarities between our nanofluidic system and synapses, we also implement a basic form of Hebbian learning. In biological neuron networks, this process consists in the modification of synaptical weights depending on the relative activation timings of two neurons connected by a given synapse (see Fig. 9.4A). If the presynaptic neuron repeatedly emits an action potential just before the ac-

tivation of the postsynaptic neuron, the synapse is strengthened, as this suggests a form of causality between the two activation events. Conversely, the synapse is weakened if the firing order is reversed, as this would point at some anticausality relation. Importantly, these modifications occur even if the presynaptic neuron only causes a mild response (that is, too weak to initiate an action potential by itself) of the postsynaptic one. Altogether, this process implements a form of principal component analysis of the inputs received by the network REF, and is believed to play a major role in learning.

To mimick this mechanism, we designed the experiment presented on Fig. 9.4B: a nanochannel is connected via the electrodes to a program which emulates the behavior of two neurons. Whenever the presynaptic neuron A emits a voltage spike, a flip-flop mechanism connects the system to a generator E_- that applies negative voltage spikes. This lasts for a time $\tau = 1$ min (at which point the flip-flop resets and the system is again connected to the two neurons), or until the presynaptic neuron B activates and the system is branched on another generator E_+ applying positive spikes instead, again for a time τ or until any of the two neurons fires again. The opposite chain of events occurs if neuron B activates first.

If neuron A activates just before neuron B, then the system receives a few negative spikes during a short time, followed by many positive spikes (during a long time τ), see Fig. 9.4C, left panel. Its conductance is thus globally increased. When the firing order is reversed, conversely, more negative than positive spikes are applied on the system (Fig. 9.4C, right panel), whose conductance is therefore lowered.

We applied this protocol as follows: we first measure the system's conductance, and run the program which consists in 8 successive activations of neurons A and B, with tuneable relative activation timing. Then, we measure any change in the conductance. The result is shown on Fig.9.4D: when the presynaptic spike is followed (within a 40 seconds window) by a postsynaptic spike, the connection is strengthened. Otherwise, if the delay is too great or if the order is reversed, the connection is weakened. This phenomenology is the same as the one observed in biological synapses.

9.5 Main insights

Carbon-based two-dimensional channels exhibit both short- and long-term memory, with an inherent plasticity that makes them qualitatively similar to biological synapses. Our artificial devices also have equivalent dimensions: our nanochannels typically occupies a volume of $1 - 10 \mu\text{m}^3$ (see Fig. 9.1B), compared to that of $1 \mu\text{m}^3$ for a human synapse. They differ, however, by the timescale over which they operate. Synapses are modified when they detect action potentials (voltage drops of roughly 50 mV that last a few milliseconds) separated by 10 ms, while in the current implementation our system reacts to voltage spikes (± 1 V during a few seconds) with relative timing delays in the range of 10 s. We expect, however, that the discrepancy can be reduced by using slightly shorter systems (with typical length 100 nm), for example, as it would allow to operate at smaller voltage (the relevant value being the electric field, which is the ratio of the voltage drop by the system's length). Despite these differences, our nanochannels allow us to implement basic

learning algorithms like Hebb's rule in a non-electronic architecture. Our findings open the way for manifold perspectives for the design of bio-inspired computing devices using nanofluidic building blocks.

Conclusion and perspectives

Nanofabrication. The initial goal of the thesis was reached with the development of activated carbon nanochannels. By taking benefit from EBIE we are now able to fabricate bidimensional channels by Van der Waals assembly without relying on the heavy EBL+RIE process. In the future one could think of coming out of the straight channel configuration. For instance, patterning conically shaped 2D channels to study bidimensional asymmetry has never been done. Another direction could be scale reduction in width. Helium FIBs like the *Orion nanofab* have a spatial resolution below 10 nm [158]. Hence such platforms could enable etching very small channels very close to each other and eventually see couplings through the solid. Finally considerable progress could be made by coming out of the transmembrane configuration relying on SiN windows. One could dream of integrating activated carbon nanochannels into microfluidic PDMS chips. This would enable connecting three or more reservoirs to perform operations such as molecular sorting as well as giving an optical access to the device during an experiment.

Ionic transport and osmotic energy harvesting. By comparing pristine and activated nanochannels, we discovered that making nanochannels by etching graphite rather than relying on spacers results in considerable enhancement of nanofluidic transport. We were able to extract activated carbon's surface properties using a unified theoretical framework. We found that it combines high surface charge with significant slippage. This is an important progress that overcomes the traditional trade-off between surface charge and slippage. Activated carbon nanochannels therefore enable to get *the best of both worlds*. This unique combination favors efficient osmotic energy harvesting with measured single pore power density only matched by atomically thin pores. A research direction may be to perform ionic sieving driven by surface charge, as Esfandiar et al. showed that steric interaction alone cannot sieve ions [27]. As mentioned in appendix D, another direction would be to study experimentally the scaling of produced osmotic power with pore number. The nanofabrication protocol, because it allows us to choose precisely the pore number and locations, may be a useful platform to understand the giant gap between single pore and macro scale membrane. Such an understanding would provide guidelines for the design of efficient osmotic energy harvesting membranes beyond the choice of a material.

Iontronics. We discovered a memory effect in activated carbon nanochannels. We could then leverage those results to show that activated carbon nanochannels exhibit a synapse-like plasticity. Finally, we implemented Hebb's rule to demonstrate, for the first time, that it is possible to perform computing operations using ions. These advanced responses are a novelty for nanofluidics which mainly focuses on material characterization or more basic applications such as osmotic energy harvesting. As stated in the end of chapter 8 and 9, our results open up many perspectives, the road being already well paved by solid state memristors. A particularly interesting direction would be the realization of an ionic artificial neural networks that would be structurally closer to the human brain than electron-based ones. An in-depth reflexion on the advantages and drawbacks of ions against electrons for real world applications also has to be conducted.

As stated in the introduction, three reasons for studying nanofluidics are the fundamental understanding of solid/liquid interfaces, the environmental needs coming from the water energy nexus, and the exceptional functionalities displayed by biological channels. Here we unveiled a new material combining surface charge and slippage allowing efficient harvesting of osmotic energy as well as a memory effect related to a synapse-like plasticity. Those advances are direct consequences of the development of a new technology: activated carbon nanochannels.

Appendices

Development of a new technology :
Activated carbon nanochannel (full
protocol)

—

Nanofabrication : additional images of the devices

We provide here additional SEM and AFM images of the pattern, with and without top layer (Figure A.1-2). In particular zoomed AFM images shows that there is now roughness nor additional pathways adjacent to the channel that would explain enhanced transport. In Figure A.3, we display some of the finalized devices used in that work.

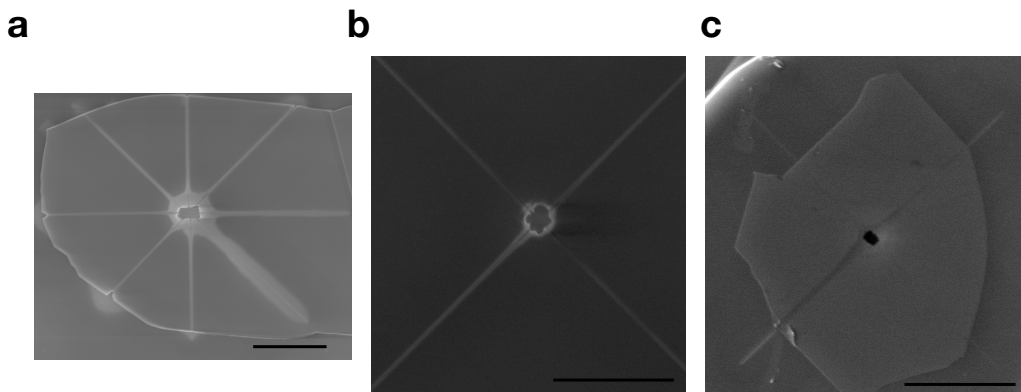


Figure B.1

Additional SEM images. **a**, Image of a pattern with 8 channels in a "star" configuration. Scale bar is 5 microns. **b**, Image of a pattern with 4 perpendicular channels. Scale bar is 5 microns. **c**, Pattern in **b** covered with a top layer graphite crystal.

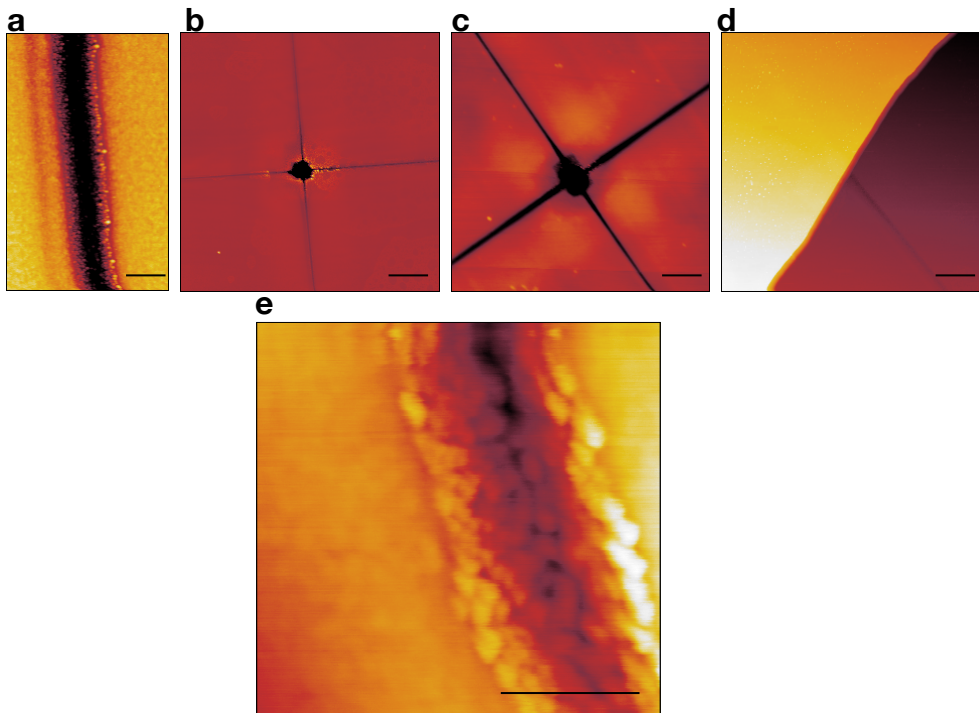


Figure B.2

Additional AFM images. **a**, High magnification image of an EBIE activated channel. Scale bar is 200 nm. **b**, Image of a pattern with 4 perpendicular channels etched by EBIE . Scale bar is 2 microns. **c**, Another image of a pattern with 4 perpendicular channels etched by EBIE . Scale bar is 2 microns. **d**, Image of a channel covered with a top layer. Scale bar is 2 microns. **e**, High magnification image of an EBIE activated channel. Scale bar is 200 nm.

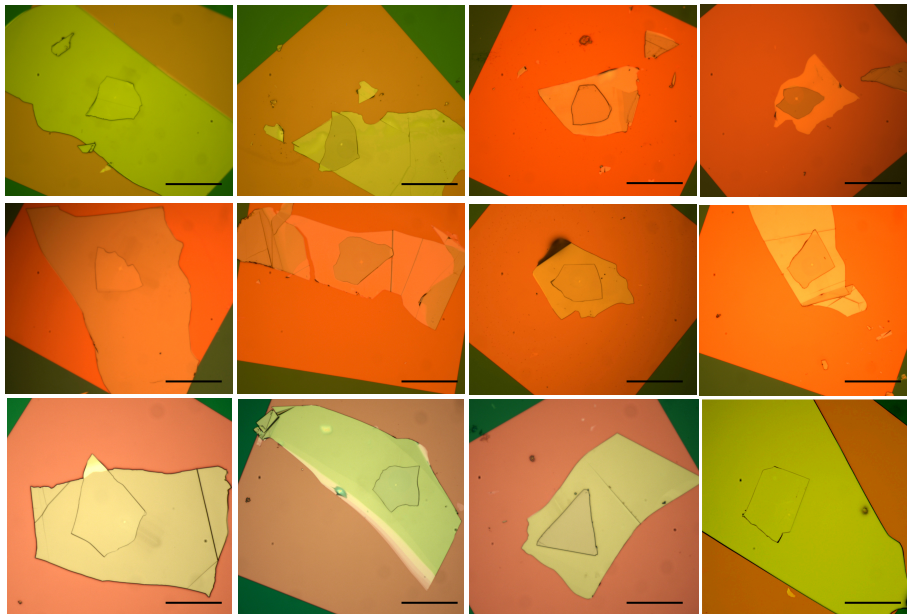


Figure B.3

Optical microscopy images of various finalized devices. Scale bars are 10-20 microns

Enhanced nanofluidic transport :SI

C.1 O₂ activated channels and characterization

C.1.1 Fabrication protocol of O₂ activated channels

The fabrication protocol of EBIE-H₂O nanochannels has been extensively described in chapter 3-4. The fabrication of O₂-etched channel has been described in the chapter 7 and is analogous to the pristine channels as it relies on the same patterning technique (RIE). The process flow is given in Figure B.1.

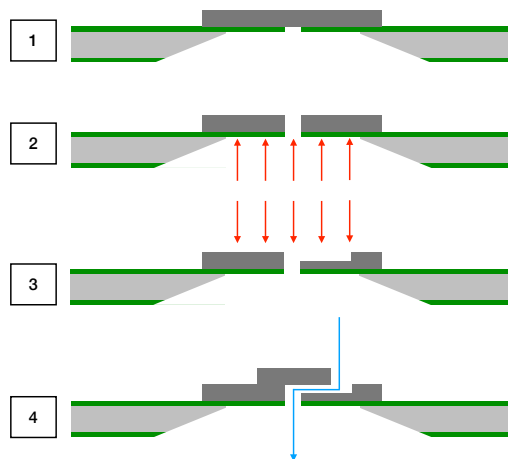


Figure C.1

O₂ activated channels nano fabrication process flow. **1,** Step 1 : Wet transfer of the bottom layer above a SIN membrane with a rectangular aperture of 20x3 microns. Bottom layers have a thickness of 50-100 nm. **2,** Step 2 : Etching of the bottom layer from the back by RIE. The crystal is covered from above with a protective PMMA layer and deposited upside down inside the RIE chamber. **3,** Step 3 : Etching of one channel by Electron beam lithography and RIE. The etching is done using an O₂ reactive plasma. **4,** Step 4 : Wet transfer of the top layer. The top layers have around 50 nm thickness.

C.1.2 Activated carbon characterization

Atomic force microscopy (AFM) characterization, Figure B.2, is carried out after patterning to gain better insights of the device fabrication. The height profiles measured from the AFM images (left and middle panels of Supplementary Figure B.2) of the bottom layer graphite crystal after activated nanochannel patterning confirm that the square aperture is completely etched along its thickness making a passage-way for molecules flowing through the nanochannel. The roughness of activated nanochannel wall is measured as approximately 1.1 nm from the height profile of AFM image in the right panel of Figure B.2, which is significantly higher than the pristine channel walls. AFM imaging and height profile measurements, middle panel of Figure 7.1.c in Main text, after transferring the top layer onto this patterned bottom layer have shown a certain but trivial sagging of the top layer into the square aperture in the bottom graphite crystal which substantiates a good adhesion between top and bottom layer graphite crystals.

After transferring this graphite-graphite heterostructure onto the silicon nitride membrane, we have used the optical microscope in transmission mode to confirm the alignment of circular opening in silicon nitride membrane with square aperture in the bottom layer. Figure B.2.b shows an optical image of one of our devices which clearly confirms the location of square aperture (red dotted circle) in bottom layer graphite inside the circular opening (white dotted circle) of silicon nitride membrane. Further, to understand the nature of activated nanochannel, we performed Raman spectroscopy. To this end, we have done electron beam induced etching of graphite for 2 nm in a square area of $1\ \mu\text{m} \times 2\ \mu\text{m}$. This is required because the laser spot (approximately 700 nm) and spatial resolution (350 nm) of our Raman spectrometer are larger than the channel width in our devices. We then acquire the spectra from one point inside the etched square (red dot) and one point outside (blue dot), Supplementary Figure B.2.c.d. The activated region has shown increased D-band intensity, Figure 7.1.d in Main text, suggesting the defected graphitic surface after electron beam induced etching.

To further understand the difference between nature of pristine and EBIE etched graphitic surfaces, we have performed lift mode electrostatic force microscopy (EFM) measurements on a EBIE etched graphite sample (with etched area of $2\ \mu\text{m} \times 4\ \mu\text{m}$) using Bruker Dimension Icon AFM. From the topography image and height profile shown in Figure in B.3.a and B.3.b, it is clear that the etched area is 3 nm deep and shows a roughness of 800 pm (r.m.s value), 4 times higher than the roughness (200 pm, r.m.s value) of pristine graphite. To understand surface charge distribution on this sample, we have lifted the tip 100 nm above the sample and obtained the EFM phase image by applying 3V between the tip and sample. Since the tip hovers 100 nm above the sample surface during EFM phase imaging scan, essentially the electrostatic force between the tip and sample contributes to the changes in phase of the cantilever oscillations. It is noteworthy from the phase signal profile (Figure B.3.d) that the change in phase of the cantilever oscillations during the scan on pristine region is found to be negligible whereas it is considerably increased when we scan on the EBIE etched region, suggesting an increased electrostatic interaction between the tip and etched region. This indicates the surface charge enhancement in the EBIE etched region compared to pristine. This is further reflected in EFM

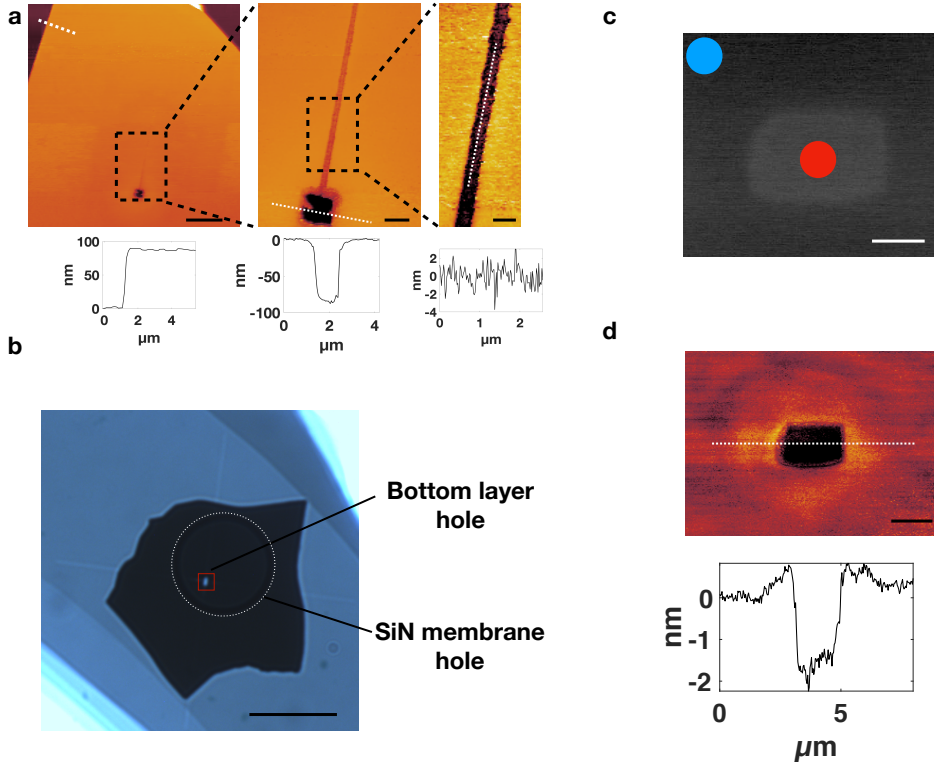


Figure C.2

Activated device characterization. **a**, Atomic Force Microscopy control of the patterning after step 1. Left: AFM image of the flake after the patterning and cross-section to control the flake thickness. Scale bar : 5 micrometers. Middle : AFM image of the pattern with control of the through hole depth. We verify that the depth is equals to the flakes' thickness. Scale bar: 1 micrometer. Right : AFM image with cut along the channel to measure the roughness. Scale bar: 250 nanometers. **b**, Transmitted light Optical microscopy of a device from below after step 3. The bottom layer appears in light blue and the top layer is black. The transfer was successful as the bottom layer has landed inside the membrane hole. The device has four perpendicular channels visible in white. Scale bar: 10 micrometers. **c**, SEM image of a etched square by EBIE for Raman characterization of milled graphite. The laser is pointed at the red spot to obtain the spectrum of functionalized graphite and at the blue spot to obtain the pristine graphite spectrum. Scale bar : 1 micrometer. **d**, AFM scan of the etched square for Raman characterization. Scale bar: 2 micrometers.

phase signal image (Figure B.3.c) with an evident contrast between etched portion (dark color region) and the pristine one (bright color region). Thus, our EFM experiments, despite being qualitative, provide a direct evidence for the surface charge enhancement on graphite due to EBIE etching.

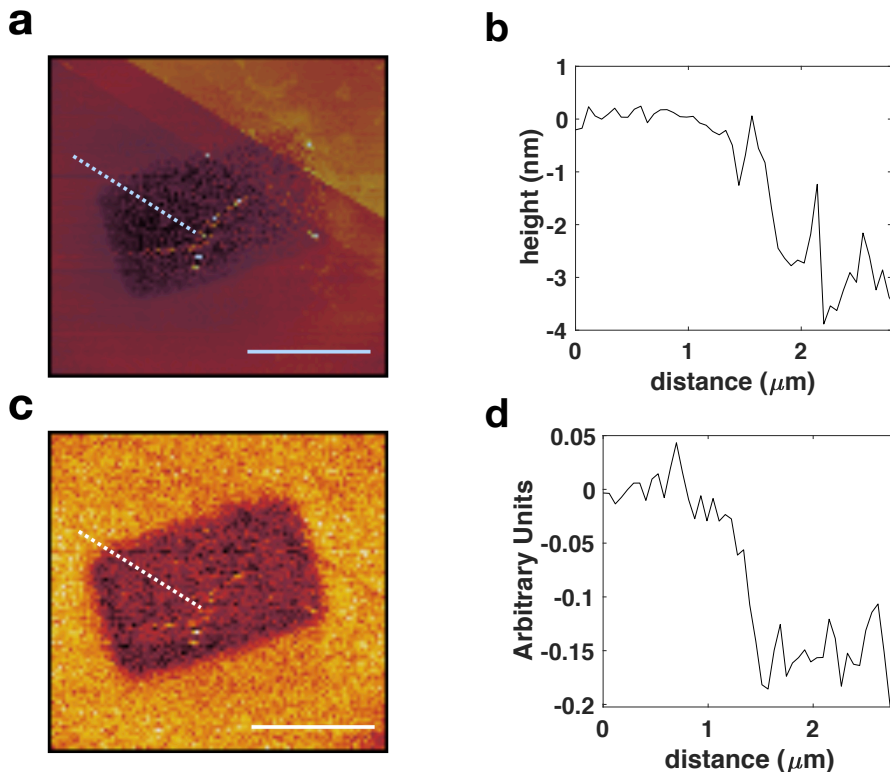


Figure C.3

EFM characterization (a-d). **a**, Topography, **b**, height profile, **c**, EFM phase image and **d**, phase signal profile of EBIE etched graphite sample. Scale bar : 2 micrometers. The height and phase signal profiles are recorded along the white dashed lines shown in **a** and **c**.

C.2 XPS analysis

It is not yet possible to realize the chemical analysis of a small activated carbon area on a bidimensional graphite crystal. Spatial resolution of XPS is in the hundred microns range, much larger than H₂O etched channels leading to insufficient resolution to determine chemical composition of etched zone. Therefore it is not possible to differentiate the oxygen and carbon present on the crystal from the one that unavoidably contaminates the substrates. The chemical analysis of EBIE, that only enables the etching of small area (a few micron square) on 2D crystals is not feasible. Hence to demonstrate the carbon oxidation following activation, we performed the chemical analysis of HOPG exposed to 1 min O₂ plasma inside a Reactive Ion Etching (RIE) reactor. This was done with the same parameters (30 W power) used to etch the O₂ activated channel that also shows enhancement of nanofluidic transport (see section 3.7). The widening of the oxygen O1s peak points to the appearance of interfacial -OH groups, likely C-OH and COOH (Figure B.4.a). This comes along with an increase of intensity of the carbon C1s peak at 288 and 289 eV which characterizes C=O and O-C=O bonds [?] (Figure B.4.b).

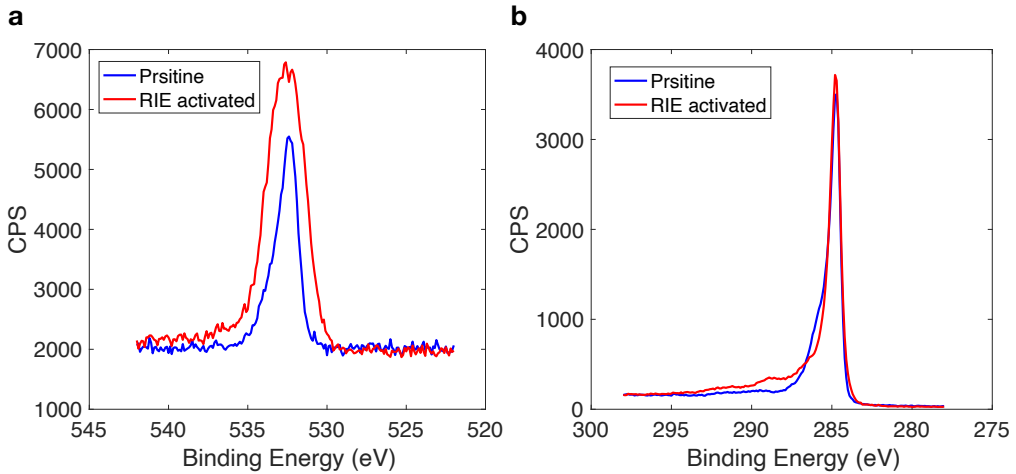


Figure C.4

XPS Analysis of HOPG after RIE activation. **a**, Oxygen O1s Peak. The ratio of oxygen to carbon increases from 5%O-95%C to 10%O-90%C following RIE exposure. **b**, Carbon C1s peak showing an increase of intensity at 288 and 289 eV.

C.3 Nanofluidics measurements

Here, we provide the as-measured experimental data for conductance, streaming and osmotic current measurements. The fluidic devices with pristine/activated nanochannels are clamped between two macroscopic reservoirs filled with KCl solutions and the electrical current is measured using chlorinated Ag/AgCl electrodes placed in the reservoirs. We note that we conducted a number of checks allowing us to assess the stability of the devices. All responses in terms of current under voltage, pressure, concentration drops, as investigated in this work, were found to be linear in the driving force. Furthermore we do not observe any conductance change after the application of pressure, nor concentration drop. Measurements at a given concentration and pH are reproducible over the lifetime of the devices. Also, as highlighted in the main text and below, the measured conductance, electro- and diffusio- osmotic mobility were consistent between each other and moreover consistent between the various channels investigated (for both the pristine family and activated family). Finally, direct checks using optical microscopy do not show any visible alteration of the device can be observed after two weeks of operation, see Supplementary Figure 15, ruling out mechanical instability of the device such as lift-off or delamination.

C.3.1 Conductance

For conductance measurements, a dc bias was applied between Ag/AgCl electrodes to perform voltage sweeps from $0\text{ V} \rightarrow 0.1\text{ V} \rightarrow -0.1\text{ V} \rightarrow 0\text{ V}$ with a step of 0.01 V and, measured the resulting current, Figure B.5.a. We observed a sharp and instant increase in the current with increase in voltage for both pristine, Figure B.5.b,

and activated, Figure B.5.c, nanochannel devices which allowed us to measure the current only for 5 sec at each voltage step. This can be understood for the pristine channel device as it contains 200 nanochannels. However, in the case activated nanochannel device, this is attributed to high conductivity of the activated channels at all concentrations. Thus, the last current value (I) of each step is extracted (red circles in the Figure B.5.b,c) and plotted as a function of applied voltage (V) to extract the conductance which is the slope of I-V curve.

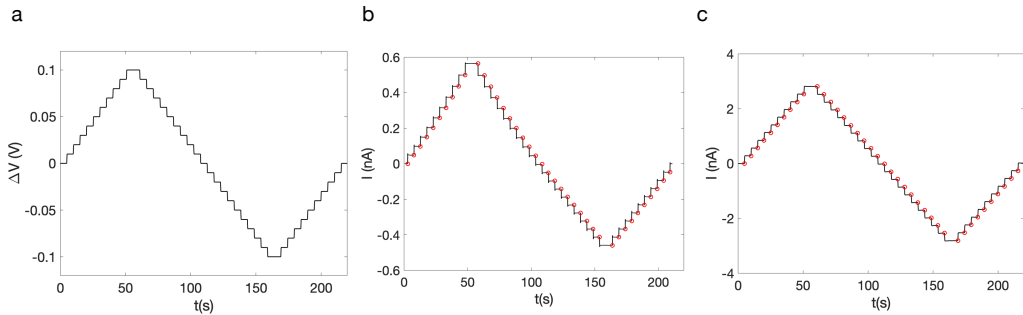
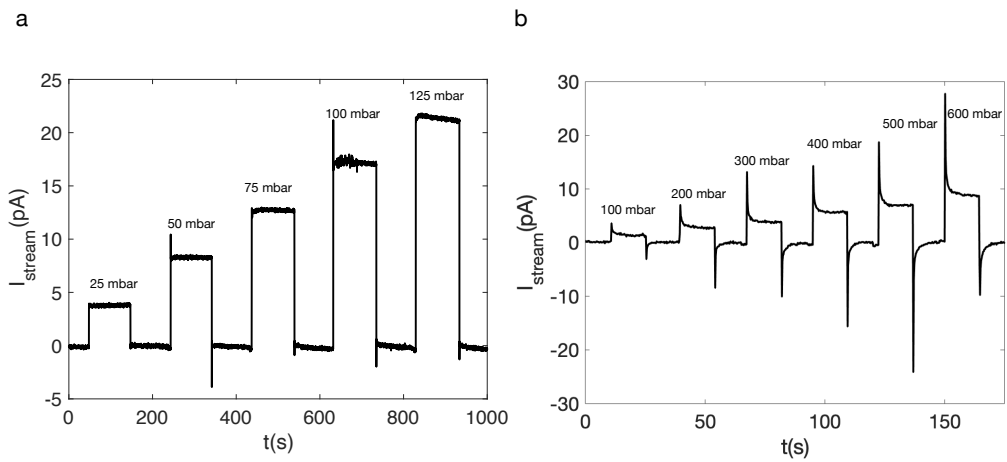


Figure C.5

Conductance raw data at pH 5.5 and $C=1\text{mM}$. **a**, Applied voltage vs time. **b**, Measured current vs time for pristine channels (System A, $h=15\text{nm}$, $N=200$ channels). **c**, Measured current vs time for activated channels (System E, $h=3\text{nm}$, $N=4$ channels).

C.3.2 Pressure driven current

For pressure driven (streaming) measurements, a pressure difference (from 0 to 600mbar) is applied between two reservoirs using a microfluidic pump (*ELVESYS* AF1). The voltage difference between the two reservoirs is set to zero during the streaming measurements for both pristine and activated nanochannel devices. A typical streaming measurement is carried out by first stabilizing the current to a constant value and then gradually applied the pressure difference to measure the streaming current, Figure B.6. These measurements are carried out depending on the streaming response of the device, for example, 5 to 15 measurements (with each measurement for 10 to 15 sec) are performed at each pressure difference in the case of activated nanochanel device. The streaming current is extracted as the difference between steady-state value of measured current in the presence and absence of applied pressure.

**Figure C.6**

Streaming current raw data. **a**, Current vs time when step of pressure are applied in pristine channels at $C=3\text{mM}$, Ph5.5 (System A, $h=15\text{nm}$, $N=200$ channels). **b**, Current vs time when step of pressure are applied in activated channels at $C=1\text{mM}$, Ph5.5 (System E, $h=3\text{nm}$, $N=4$ channels).

C.3.3 Osmotic current

For osmotic current measurements, we filled the two reservoirs with different concentrations (C_{max} , C_{min}) of KCl and, measured the I-V curves as mentioned in the Section B.3.1. In our experiments, the C_{max} to C_{min} ratio is varied from 1 to 1000. At each concentration ratio, we have extracted the channel conductance, G , under the salinity gradient and, the current value I_{meas} at $\Delta V=0$, Supplementary Figure B.7. Because of the unequal concentration at the electrodes a redox Nernst potential builds up. To obtain the osmotic current, the Nernst current written $I_{Nernst} = G * \Delta E_{redox}$ resulting from the redox potential has to be subtracted to I_{meas} . Therefore the osmotic current I_{osm} is expressed as $I_{osm} = I_{meas} - G * \Delta E_{redox}$. The redox potential values are obtained or interpolated from [57]. When $C_{max} = C_{min}$, we find $I_{meas} \approx 0$ A.

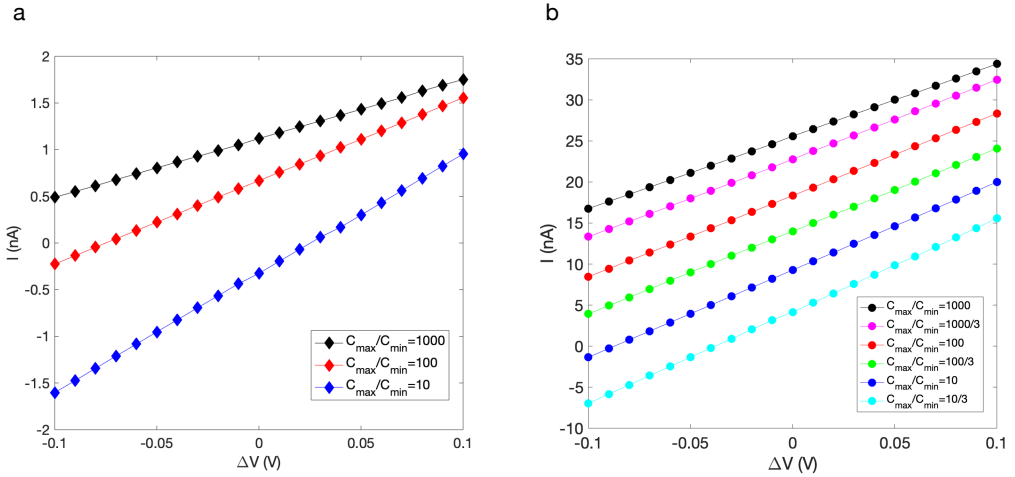


Figure C.7

Osmotic current raw data at pH5.5. **a**, Current vs voltage for various concentration drops across a pristine channel (System C, $h=5\text{nm}$, $N=1$ channel). **b**, Current vs voltage for various concentration drops across an activated channel (System F, $h=8\text{nm}$, $N=1$ channel).

C.3.4 Additional measurements for electro-osmotic mobility

We provide additional streaming currents experiments for various salt concentration at pH5.5 on 10nm pristine and activated channels, Figure B.8.a-a'. The corresponding zeta potentials as a function of the salt concentration are in fair agreement with the theoretical predictions, Figure B.8.b-b'.

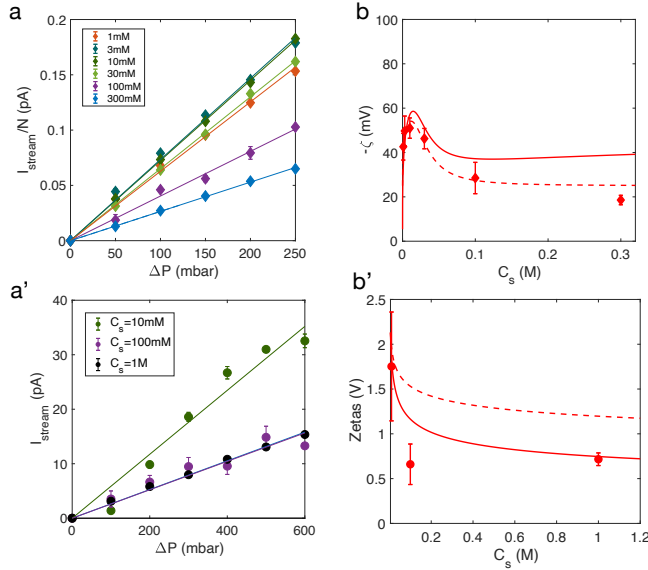
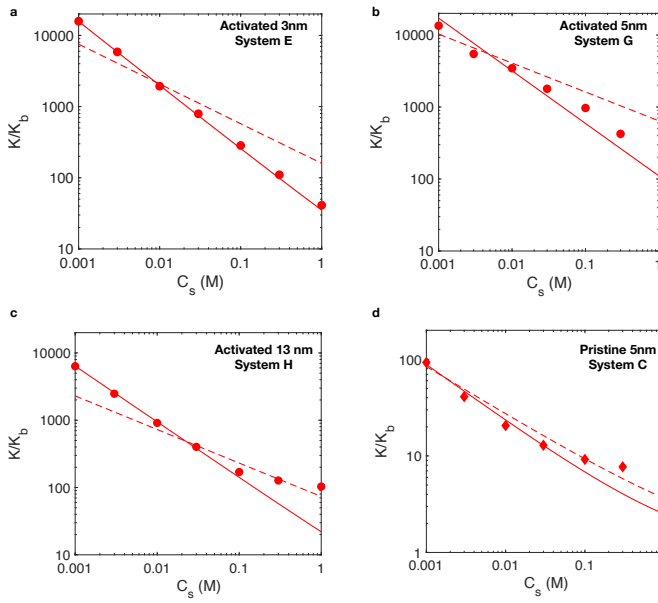


Figure C.8

Additional streaming measurements for various salt concentrations at pH5.5. Pristine channel (System B, $h=10\text{nm}$, $N=30$ channels): **a**, Streaming current vs applied pressure for various salt concentrations. **b**, Zeta potential vs salt concentration. **Activated channel (System D, $h=10\text{nm}$, $N=4$ channel):** **a'**, Streaming current vs applied pressure for various salt concentrations. **b'**, Zeta potential vs salt concentration. The solid line is the model assuming a functional surface charge $-\Sigma_{(m)} \propto C_s^\alpha$ and the dashed line is the constant surface potential model.

C.3.5 Additional measurements for conductivity enhancement

We provide additional conductivity experiments for various salt concentration at pH5.5 on three activated channel and one pristine channel, Figure 9.a-d. The measured conductivity enhancement as a function of the salt concentration is in good agreement with the theoretical predictions.

**Figure C.9**

a-d, Additional conductivity vs salt concentration measurement, normalized by bulk conductivity. The solid line is the surface charge model and the dashed line is the constant surface potential model, see Section 4. $\text{Ph}=5.5$.

C.3.6 Measurements with varying pH

We explore the surface reactivity of nanofluidics channels by performing measurements at various pH. Pristine channels exhibit a sensibility towards basic pH (Figure B.10.a), in good agreement with previous measurements in thinner slits [?]. For activated channels a higher sensitivity to acidic pH is noted at low concentration (Figure B.10.b). This is consistent with osmotic current measurement at various pH, showing neglectable current generation at pH3 while no significant increase is noted at basic pH. (Figure B.10.c). At high concentration, activated channels show minimum conductance at low pH and zeta potential appears to be sensitive to pH (Figure B.10.d-e)

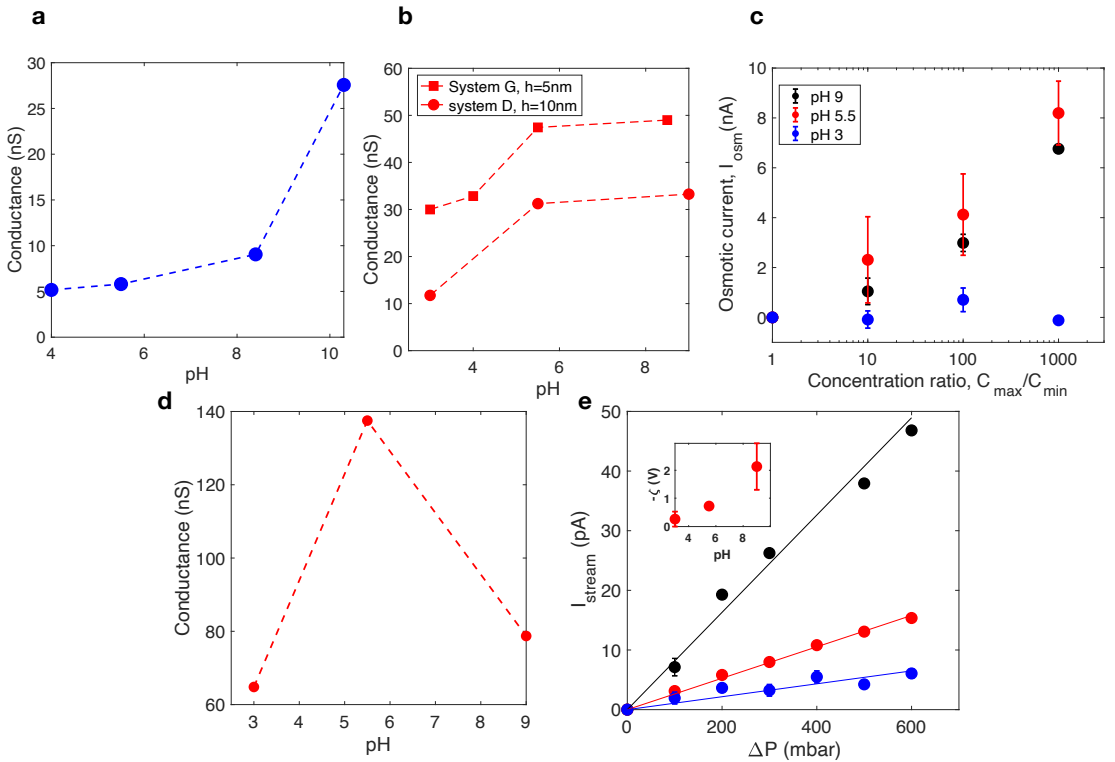


Figure C.10

a, Conductance vs pH in pristine channels (systeme B, h=10nm) at 30mM KCl. **b**, Conductance vs pH in two activated channels pH at 1mM KCl. **c**, Osmotic currents vs concentration ratio at various pH in an activated channel (system D). **d**, Conductance and corresponding streaming currents **e**, at 1M in an activated channel (system D).

C.3.7 Measurements with varying etching environments

In this section we compare O₂-etched (RIE), H₂O-etched (EBIE) and pristine channels. As displayed in Figure B.11.a-b, both first routes induce activation of the graphitic channel. We notice good agreement between measurements and theoretical predictions. Both H₂O and O₂ etched channels can produce high amounts of osmotic currents (Figure B.11.c). This further indicates the presence of C/O species in channels etched in oxygen-rich environments along with our XPS analysis.

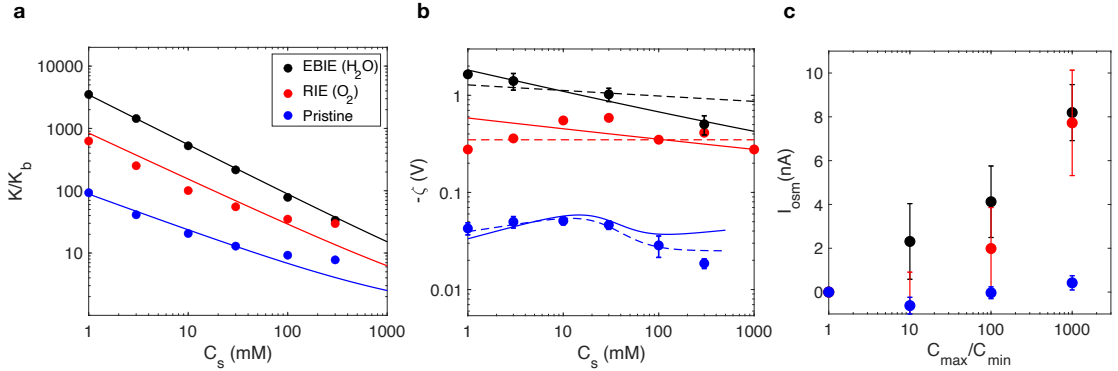


Figure C.11

a, Enhanced conductivity vs salt concentration in a H₂O etched channel (system D, h=10nm), a O₂ etched channel (system I, h=7nm) and a pristine channel (system C, h=5nm). All systems have a single channel. Ph=5.5. Solid lines are fit using surface charge model. **b**, Zetas potential vs salt concentration for a H₂O etched channel (system E, h=3nm), a O₂ etched channel (system I, h=7nm) and a pristine channel (system B, h=10nm). Ph=5.5. Solid lines are fit using surface charge model and dashed lines are fit with constant surface potential model. legend is the same as in previous panel. **c**, Osmotic current vs concentration gradience in a H₂O etched channel (system D, h=10nm), a O₂ etched channel (system J, h=5nm) and a pristine channel (system C, h=5nm). All systems have a single channel. pH=5.5. legend is the same as in previous panels.

C.3.8 Measurements with varying top layer material

We compare in Figure B.12 O₂-etched channels using RIE with a top layer made of different materials (graphite and boron nitride) and also pristine channels as a reference. We find little difference between activated devices. This signify that slippage from the top layer does not contribute significantly to the transport and can be neglected, in agreement with our model for activated surfaces.

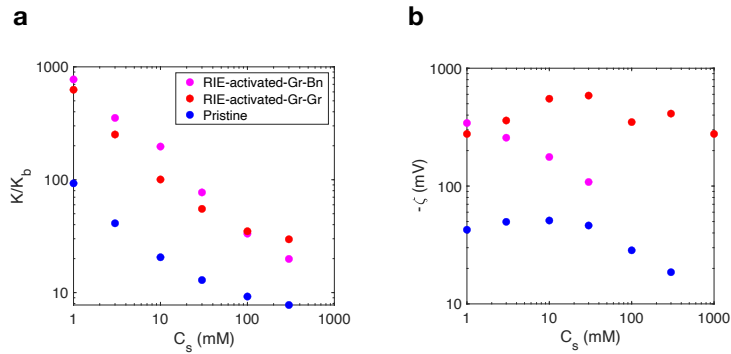


Figure C.12

a, Enhanced conductivity vs salt concentration for one O_2 etched channel with graphite top layer (system I, $h=7\text{nm}$), one O_2 etched channel with h-BN top layer (system K, $h=7\text{ nm}$) and a pristine channel (system C, $h=5\text{nm}$). All systems have a single channel. $\text{Ph}=5.5$. **b**, Zeta potential vs salt concentration for one O_2 etched channel with graphite top layer (system I, $h=7\text{nm}$), one O_2 etched channel with h-BN top layer (system K, $h=7\text{ nm}$) and a pristine channel (system B, $h=10\text{ nm}$). $\text{Ph}=5.5$.

C.3.9 Post-mortem microscopy

As shown in supplementary Figure C.13, no visible alteration, such as lift off or partial delamination **delamination**, of the device can be seen after two weeks of operations.

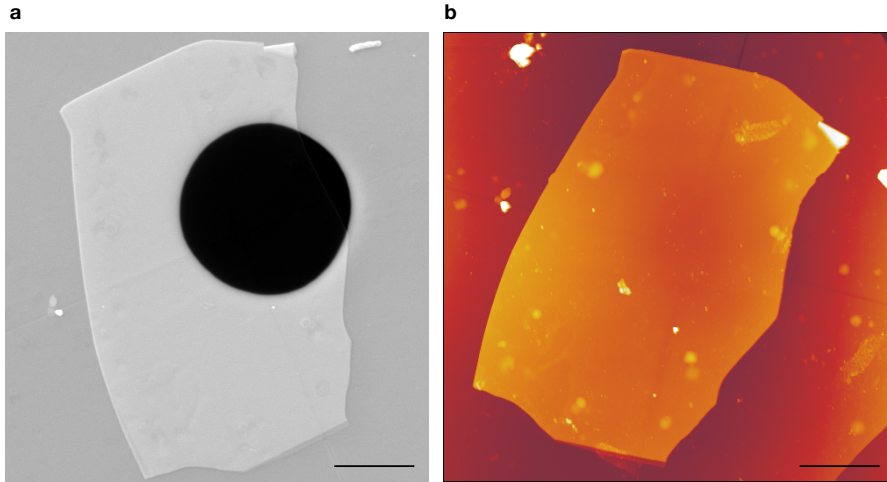
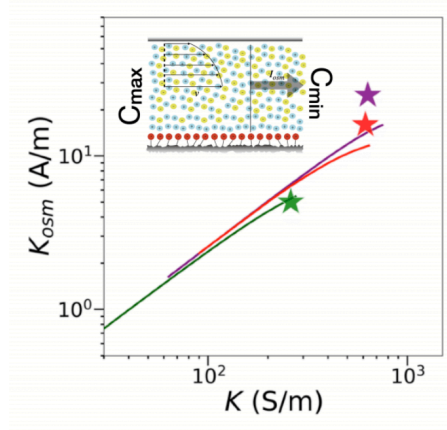


Figure C.13

Activated channel device after operation. **a**, SEM image of a device after operation. The suspended part of bottom and top layer are not visible. Scale bar : 5 micrometers. **b**, AFM scan of the same device. Scale bar : 5 micrometers.

C.3.10 Modeling for diffusio-osmotic experiments

Here we provide theoretical predictions vs experimental values for the diffusio-osmotic experiments in activated channels. Good agreement is found between experiments and theory (Figure B.14). No fitting parameters are used as the surface charge and slippage are obtained from previous conductivity and zeta potential measurements.


Figure C.14

Diffusio-osmosis in activated carbon nanochannels : experiment vs modeling. The star symbols correspond to the corresponding experimental value for K and K_{osm} . for K we use the experimental value measured during the osmotic measurements, averaged over the various concentration contrasts, as it barely changes when C_{min} is varied while fixing $C_{max} = 1M$. Solid lines are theoretical predictions. The inset shows velocity profile inside an activated channel.

C.4 Channels characteristics and modelling

C.4.1 Supplementary Tables

Table C.1

System A: Data extracted from measurements at pH 5.5: pristine channel with height $h = 15nm$, width $w = 120nm$, length $l = 9600 nm$, $N=200$ channels.

C_s (mM)	K/K_{bulk}	ζ (mV)	V_0 (V)	Σ_m (C/m ²)	b_0 (nm)
1	9.08	-41	–	–	–
3	5.2	-65	-0.040	-0.005	31
10	3.5	-75	-0.042	-0.010	30
30	2.8	-70	-0.050	-0.023	15
100	2.3	-61	-0.060	-0.054	1.7
300	2.2	-46	–	–	–

Table C.2

System B: Data extracted from measurements at pH 5.5: pristine channel with height $h = 10\text{nm}$, width $w = 200\text{nm}$, length $l = 10000\text{ nm}$, $N=30$ channels.

C_s (mM)	K/K_{bulk}	ζ (mV)	V_0 (V)	Σ_m (C/m ²)	b_0 (nm)
1	6	-43	-0.021	-0.0016	63
3	4.6	-48	-0.025	-0.0033	37
10	2.8	-53	-0.024	-0.0056	36
30	2.6	-43	-0.034	-0.0145	8
100	1.9	-26	-	-	-
300	1.5	-18	-	-	-

Table C.3

System C: Data for the conductivity enhancement pH 5.5: pristine channel with height $h = 5\text{nm}$, width $w = 150\text{nm}$, length $l = 6000\text{ nm}$, $N=1$ channel.

C_s (mM)	K/K_{bulk}
1	93
3	41
10	21
30	13
100	9
300	8
1000	7

Table C.4

System D: Data extracted from measurements at pH 5.5: H₂O activated channel with height $h = 10\text{nm}$, width $w = 150\text{nm}$, length $l = 3000\text{ nm}$, $N=1$ channel.

C_s (mM)	K/K_{bulk}	ζ (mV)	V_0 (V)	Σ (C/m ²)	b_0 (nm)
1	3508	-	-	-	-
3	1439	-	-	-	-
10	525	-1750	-0.205	-0.310	7.7
30	215	-	-	-	-
100	78	-640	-0.219	-1.29	0.60
300	33	-	-	-	-
1000	15	-720	-0.183	-2.0	0.45

Table C.5

System E: Data extracted from measurements at pH 5.5: H₂O activated channel with height $h = 3\text{nm}$, width $w = 100\text{nm}$, length $l = 10000\text{ nm}$, $N = 4$ channels.

C_s (mM)	K/K_{bulk}	ζ (mV)	V_0 (V)	Σ (C/m ²)	b_0 (nm)
1	15818	-1640	-0.263	-0.304	7.2
3	5867	-1400	-0.249	-0.398	4.6
10	1932	–	–	–	–
30	791	-1022	-0.221	-0.733	1.8
100	283	–	–	–	–
300	109	-503	-0.215	-2.0	0.27
1000	40	–	–	–	–

Table C.6

System F: Data for the conductivity enhancement pH 5.5: H₂O activated channel with height $h = 8\text{nm}$, width $w = 200\text{nm}$, length $l = 10000\text{ nm}$, $N = 1$ channel.

C_s (mM)	K/K_{bulk}
1	19280
3	7714
10	2719
30	1034
100	339
300	129
1000	47

Table C.7

System G: Data for the conductivity enhancement pH 5.5: H₂O activated channel with height $h = 5\text{nm}$, width $w = 200\text{nm}$, length $l = 8000\text{ nm}$, $N = 1$ channel.

C_s (mM)	K/K_{bulk}
1	13460
3	5465
10	3455
30	1794
100	970
300	324

Table C.8

System H: Data for the conductivity enhancement pH 5.5: H₂O activated channel with height $h = 13\text{nm}$, width $w = 160\text{nm}$, length $l = 7000\text{ nm}$, $N = 3$ channel.

C_s (mM)	K/K_{bulk}
1	6340
3	2477
10	400
30	279
100	170
300	123
1000	100

Table C.9

System I: Data for the conductivity enhancement pH 5.5: O₂ activated channel with height $h = 7\text{nm}$, width $w = 300\text{nm}$, length $l = 10000\text{ nm}$, $N = 1$ channel.

C_s (mM)	K/K_{bulk}
1	627
3	251
10	100
30	55
100	34
300	30

Dimensions for O₂ activated channel (System J) : height $h = 5\text{nm}$, width $w = 120\text{nm}$, length $l = 6000\text{ nm}$, $N = 1$ channel)

Table C.10

System K: Data for the conductivity enhancement pH 5.5: O₂ activated channel with h-BN top layer with height $h = 7\text{nm}$, width $w = 300\text{nm}$, length $l = 7000\text{ nm}$, $N = 1$ channel.

C_s (mM)	K/K_{bulk}	ζ (mV)
1	773.62	342.75
3	352.92	257.26
10	196.73	176.47
30	77.19	108.24
100	33.30	-
300	19.8	-

C.4.2 Summary of the modelling procedure

Conductance and electro-osmotic mobility (or zeta potential), are obtained from voltage and pressure drop experiments respectively. Using our model (Eq.(1) in the main text) for each salt concentration, the slip length $b_0(C_s)$ and surface charge $\Sigma_m(C_s)$ are extracted. Finally we use curve fitting to obtain the constant parameters α , γ , β , ω , B_m and B of the functional dependence of the slip length $b_0(C_s)$ and surface charge $\Sigma_m(C_s)$ with concentration. In an alternative description, we replaced the functional dependence of the charge $\Sigma(C_s)$ with a constant surface potential Ψ_0 assumption (independent of salt concentration). This prediction is shown in the main text (dashed line in Figs. 2 and 3). Note that in this description the surface charge is related to Ψ_0 according to

$$\Sigma_m(C_s) = \frac{e}{2\pi\lambda_D(C_s)\ell_B} \sinh\left[\frac{e\Psi_0}{2k_B T}\right]$$

with $\lambda_D = (8\pi\ell_B C_s)^{-1/2}$ the Debye length and $\ell_B = 0.7\text{nm}$ the Bjerrum length (with C_s in number of ions per cubic meter in this expression).

C.4.2.1 Pristine channels

For the pristine channels, we used the following parameters $\alpha_{ion} = 0.8$, $\beta_s = 50.0$. The charge is described as a scaling law $-\Sigma_m = \gamma \times C_s^\alpha$ in C/m^2 , with the parameters γ and α reported in the Supplementary Table 7 for each pristine device A, B, C. The slip length is described as $b_0(C_s) = B_m \times (1 + \omega C_s^\beta)^{-1}$ with $B_m = 35\text{nm}$, $\omega = 3.10^{-4}$, $\beta = 2.4$, with b in nanometers and C_s is in millimolar. We use the same expression for $b_0(C_s)$ for all three pristine channels A, B, C. The values for Ψ_0 for the ‘constant surface potential’ predictions are provided in the Supplementary Table 11 for each pristine device A, B, C.

C.4.2.2 Activated channels

For the activated channels, we used the following parameters $\alpha_{ion} = \beta_s = 0$. The functional dependence of the charge and slip length are described as a scaling laws

Table C.11

Summary for charge modelling parameters for the pristine systems: $-\Sigma_m = \gamma \times C_s^\alpha$ in C/m^2 ; Ψ_0 (in V) C_s is in mM; pH 5.5.

System	γ	α	$\Psi_0(V)$
A	0.0022	0.68	-0.05
B	0.0015	0.62	-0.025
C	0.0112	0.42	-0.09

according to $\Sigma = \gamma \times C_s^\alpha$ in C/m^2 , and $b_0(C_s) = B \times C_s^{-\beta}$ with b_0 in nanometers and C_s is in millimolar. The parameters γ , α , B and β are described in the Supplementary Table 12 for each activated device D, E, F,G,H.

Table C.12

Summary for modelling parameters for the activated systems: $-\Sigma = \gamma \times C_s^\alpha$ in C/m^2 ; $b_0 = B \times C_s^{-\beta}$ in nanometers; C_s is in mM; pH 5.5

System	γ	α	B	β
D	0.125	0.40	31	0.61
E	0.283	0.32	8.4	0.56
F	0.30	0.33	24	0.55
G	0.25	0.33	20	0.4
H	0.22	0.33	25	0.5
I	0.112	0.37	6	0.5

C.4.2.3 Epi-osmotic mobility

From Eq. (2) in the main text, it is obvious that χ , which is a ratio between debye length and Gouy-Chapman length, is a key parameter in calculating the predicted osmotic mobility. As defined in the Eq. (1) in the main text, $\chi = 2\pi\lambda_D\ell_B\frac{|\Sigma_m|}{e}$, which shows $\chi \propto |\Sigma_m|$. Therefore, we can discuss two regimes in this case when $\chi \gg 1$ (high surface charge) and $\chi \ll 1$ (low surface charge).

In the present study, for the pristine channels we enter into small surface charge regime ($\chi \ll 1$) but it is important to note that the surface charge on pristine channel is mobile surface charge. Hence, we have non-zero values for α_{ion} and β_s . Since $\chi \ll 1$, the numerator of the last term in the bracket of Eq. (2) in the main text becomes small and could reach to zeroâmaking the contribution from this term as negligible. Further, the remaining term in the bracket scales as Σ^2 . Thus, the epi-osmotic mobility K_{osm} for pristine channel scales like Σ^3 .

For the activated channels, we enter in high surface charge regime ($\chi \gg 1$) and, the charge here is fixed which makes $\alpha_{ion} = \beta_s = 0$. Since $\chi \gg 1$, the last term in the bracket of Eq. (2) in the main text scales as $b_0 \times \Sigma$ and, the remaining term approaches to 1. This results in K_{osm} to scale as $\Sigma + (b_0 \times \Sigma^2)(1 - \alpha_{ion})/\lambda_D$ for activated channels. However, from the transport frame work analysis of conductance and zeta potential measurements for activated nanochannels, we know that b_0 scales as $\Sigma^{-\theta}$ with $\theta = 1.5$ to 1.7 . This in turn results in K_{osm} to scale as Σ for activated nanochannels.

C.4.3 Assumptions and conclusions of the modeling procedure

Table C.13

Main assumptions for the modeling procedure

Assumptions	Reference
Non-linear Poisson-Boltzmann electrostatics	[67]
Carbon low friction	[26]
Surface charge regulation	[58]

Table C.14

Main conclusions of the study

Insights	Consistent reference
Formation of C/O species after oxygen rich exposure of carbon	[99]
Physisorption (mobile charge) on pristine graphitic surfaces	[101]
Enhanced nanofluidic transport by combination of low friction and surface charge	[106, 107]

C.5 Analysis of the surface properties

In this section we analyze the surface properties of pristine and activated carbon presented in Figure 7.2. Activation increases the surface charge by 1-2 orders of magnitude (Figure B.15.a) and reduces the slip length by one order of magnitude (Supplementary Figure B.15.b). We observe a strong decrease of the slip length with the surface charge for activated carbon surfaces (Supplementary Figure B.16). This behavior was recently attributed to a heterogeneous charge repartition using molecular dynamic simulations [68].

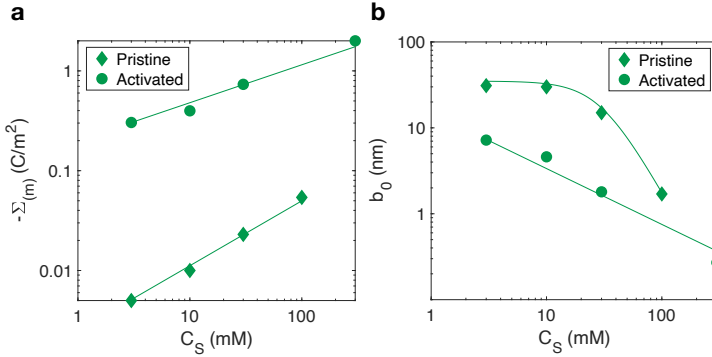


Figure C.15

a, Surface charge vs salt concentration for pristine (system A, $h=15\text{nm}$) and activated (system E, $h=3\text{nm}$) channels. Those values are extracted from Equation 1 of the main using combined conductivity and electro-osmotic mobility measurements presented in Figure 7.2. Solid lines : fit of the form $-\Sigma_{(m)}(C_s) = \gamma C_s^\alpha$. The fitted coefficients γ and α are displayed in table B.11 (pristine) and B.12 (activated). **b**, Slip length vs salt concentration for pristine (system A) and activated (system E). Those values are extracted from Equation 1 of the main using combined conductivity and electro-osmotic mobility measurements presented in Figure 2. Solid lines : fit of the form $b_0(C_s) = B_m/(1 + \omega C_s^\beta)$ for pristine carbon and $b_0(C_s) = B C_s^\beta$ for activated carbon. The fitted coefficients B_m , ω , B and β are displayed in table B.11 (pristine) and B.12 (activated).

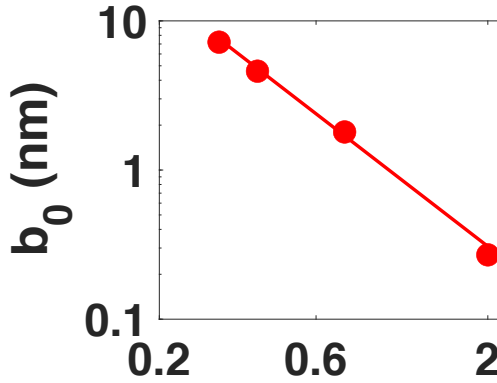


Figure C.16

Surface charge repartition with activated carbon. Slip length vs surface charge for activated carbon (System E). Data plotted from Figure B.15. The points with high slip length/low surface charge are at low salt concentration and the points with high charge low slip length/high charge are at high salt concentration. Solid line is a fit of the form $b_0 \sim \Sigma^{-\theta}$ with $\theta = \beta/\alpha \simeq 1.7$.

C.6 Benchmark activated carbon nanochannels performances

We report in Table B.15 the energy harvesting performances of other single pore as presented by the authors. We report in Supplementary Figure B.17 the surfaces properties against the 1D (nanotubes) and 2D nanopores reported in the literature.

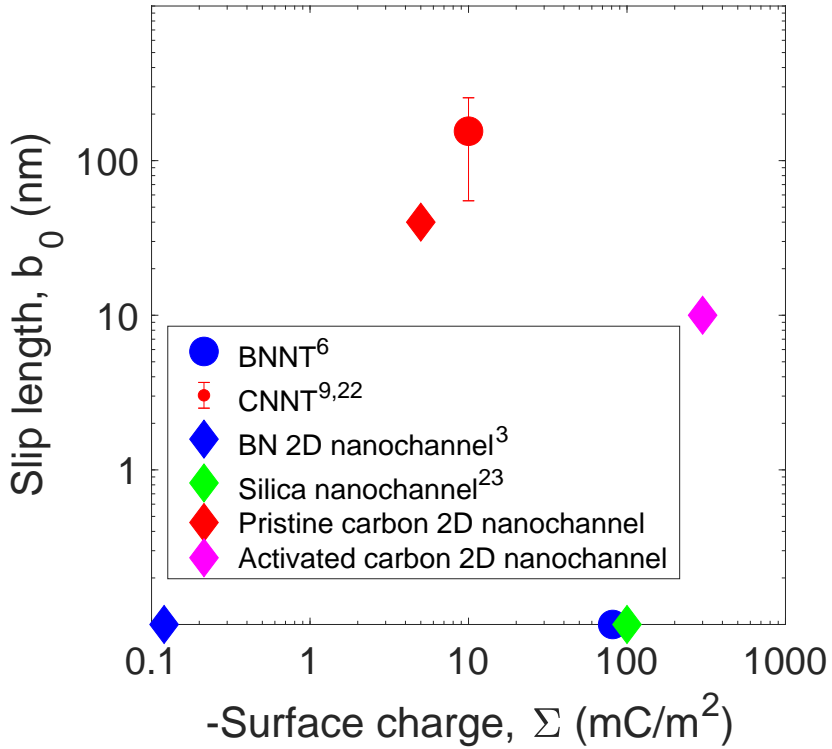


Figure C.17

Surface charge vs slip length of pristine and activated carbon nanochannels as well as other 1D and 2D nanopores. The experimental conditions are KCl (1-10mM) and pH5.5.

Table C.15

Osmotic energy performances and geometry of activated carbon nanochannels relative to other single pore devices

Material	Section dimension	Length (μ m)	pH	C_{max}/C_{min}	osmotic current (nA) maximum value	Power (pW)
Conical Nanopore	1.2 μ m (d_{base}) -41nm (d_{tip})	12	5.6	1000	1.28	\sim 100
h-BN Nanotube	d=80nm	1.2	11	1000	1	20
MoS_2 Nanopore	d=10nm	0.6 nm	11	1000	11	810
Functionalized PET Nanopore	750 nm (d_{base}) -12nm (d_{tip})	6	7.6	1000	0.8	26
PET poly-L-lysine mesocone	2 μ m (d_{base}) -400nm (d_{tip})	11	6	500	6	120
Hydrogel Nanopore	d=100 nm	13	7	1000	0.2	20
PET bullet Nanochannel	1 μ m (d_{base}) 15 nm (d_{tip})	12	10	100	3	80
Ultra charged Mesopore	920 nm(d_{base}) 405 nm (d_{tip})	11.5	11	1000	27	660
Activated carbon nanochannels	200 nm(width) 8nm(depth)	10	5.5	1000	12	370

Up-scaling of energy harvesting

D.1 Multichannel devices

As pointed in the end of the previous chapter, up-scaling of energy harvesting devices from a single channel to membranes generating power at levels usable for the industry is a considerable challenge. A first step towards up-scaling is studying the effect of increasing the number of channel onto the power generation. The power generated is supposed to scale sub linearly with the number of pores/channel because of increasing entrance resistance and eventual polarization concentration which is a consequence of the pore's ionic selectivity [72, 73]. Activated carbon channels, because they have a high conductivity and relies on the diffusio-osmosis mechanisms that does not require selectivity, are supposed to be less problematic for up-scaling.

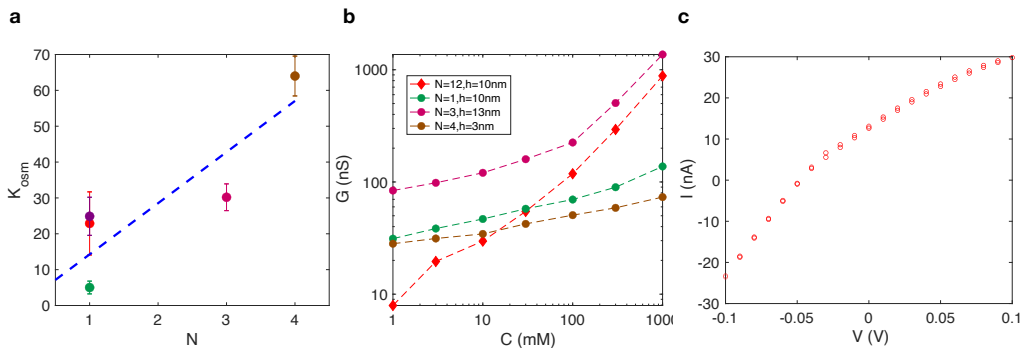


Figure D.1

Study of multichannel devices for power generation. **a**, Scaling with the number of channels, N of results presented in Figure 6.4. The blue line is a obtained by linear fitting. **b**, Conductance vs concentration of single and multichannel devices. The devices with 3 and 4 channels have a perpendicular configuration while for the devices with 12 channels have a parallel configuration (see figure 3.2). **c**, Current vs voltage for the device with 12 parallel channels at a concentration gradient of 1M vs 100mM.

This part of the thesis was done with Javier Perez who fabricated the GO membranes.

For a perpendicular channel configuration and $N < 4$, there seems to be a Linear correlation between osmotic coefficient and the number of channel (Fig D.1.a). This tends to indicate that there is no inter-pore effect for a small number of channel furthermore having inlets spaced by a distance of several microns (see Fig.3.3.b). However for a multichannel device with 12 parallel channels, spaced by roughly 100 nanometers (see Fig.3.3.c), results point to inter-pore effects reducing ionic transport and impeding efficient harvesting of osmotic energy. The conductance for such a device has a different scaling with the salt concentration than other single and perpendicular multichannel devices, reaching very low values at low salt concentration (Fig D.1.b). Under the application of a concentration gradient, the current induced by a voltage drop exhibit a rectification (Fig D.1.c). This behavior was never seen on other devices that always displays linear I vs V response in similar experimental conditions (see appendix C).

These results may be a signature of an unexplored inter-pore effect impeding efficient ionic transport. Activated carbon nanochannels by their versatility in fabrication and high surface charge may be used to study fundamental aspects of inter-pore effects. In particular, knowing the distance below which pore starts to interfere could be a useful information for the design of energy harvesting membranes at higher scales.

D.2 Measurements of macro-scale membranes

Another and more direct way of leverage the results obtained in chapter 6 may be the improvement of already existing macro-scale membranes, in particular Graphene Oxide. We learned that activated carbon is a suitable material for power generation because it promotes efficient diffuse-osmosis by a combination of high surface charge and low friction. Those are the elements we tried to translate to the next scale.

A first step in this direction was done by improving the setup used in the lab for the measurement of macro-scale membranes (Fig D.2.a). The equivalent resistance R_{eq} is defined as $R_{eq} = R_m + 2R_r$, with R_m being the effective membrane resistance and R_r the reservoir's resistance (Fig D.2.b). Hence one can see that if $2R_r \gg R_m$ the resistance will be dominated by the reservoirs and it will not be possible to measure the membrane's conductivity and differentiate a membrane from another. This is never a problem for single or multi-channel ($N \leq 200$) Van Der Waals heterostructure devices but becomes problematic with macro-scale membranes having numerous pores. This was confirmed by a control test without a membrane loaded that showed no noticeable difference with a cell loaded confirming that only the reservoirs were measured.

To overcome this issues we increased the effective membrane resistance by placing it on a pierced SiN window and reduced the reservoir's resistance by measuring it in the "small cell" similarity to Van der waals nanofluidic devices (Fig D.2.c). This way the membranes are placed on a micrometric aperture instead of a centimetric aperture. After the membrane fabrication by vacuum deposition on a nylon or equivalent substrate, it is deposited faced down onto the window. Then we wet it with water before removing the excess water. Finally the substrate is gently removed to obtain a self supported membrane (Fig D.2.d). Finally the cell is closed with o-ring as for the case of Van der waals nanofluidic devices.

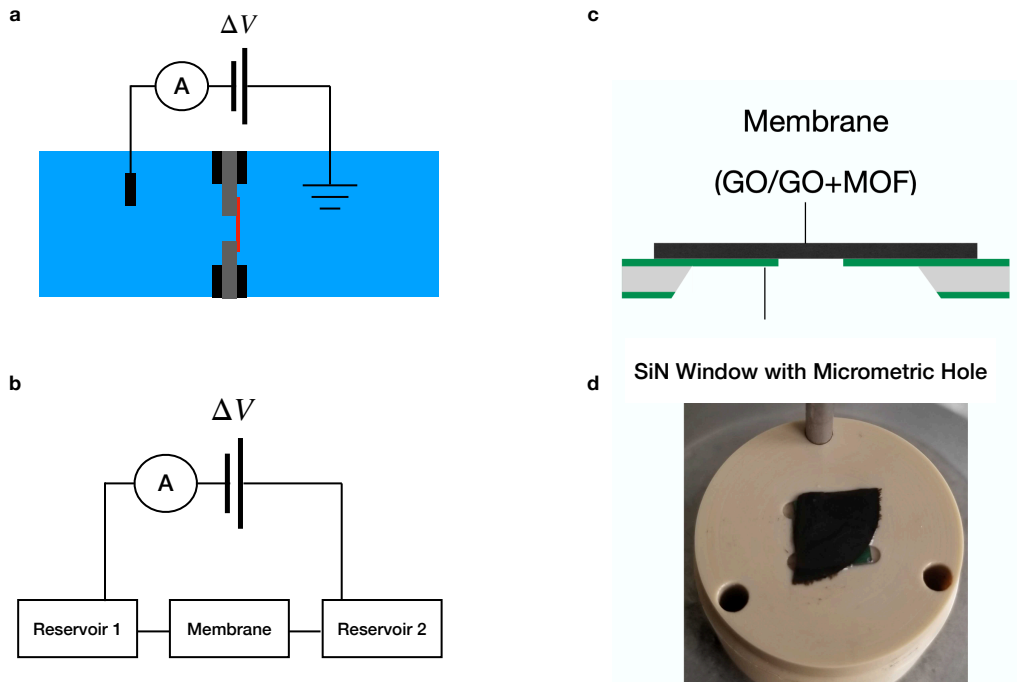


Figure D.2

Measurements of GO membranes on SiN windows with micro-metric apertures. **a**, Schematic of previous setup for measuring GO membranes. A membrane (red) is glued on a plexiglas part with a centimetric aperture (in grey). The plexiglas is sandwiched between two reservoirs using o-rings (in black). **b**, Equivalent diagram of a measurement cell. **c**, Schematic of the new configuration where a membrane is deposited on a SiN window with micrometric aperture. **d**, Photography of a GO piece deposited above a SiN window. The cell is the same used for electrokinetic measurement of VdW heterostructure devices.

To verify the validity of our hypothesis and benchmark our new experimental setup we performed conductance measurements at various concentrations with and without graphene oxide membranes (10 micrometers in thickness) on SiN windows with varying aperture lengthscales (Figure D.3.a). We note a contrast in conductance if the GO membrane is loaded for apertures smaller than 7 microns at low concentrations. This shows that for such windows $R_m > 2R_r$, here R_m being the resistance of the SiN pierced window with or without a GO membrane. Thus the membrane/bare pore conductance can be measured with SiN windows having a smaller aperture. To further confirm that we are now able to measure conductance of macro-scale membranes, we compare GO with two other composite membranes (Figure D.3.b). A clear contrast at low concentration is observed. We thus now have at our disposal a simple process to compare macro-scale membranes of different composition. Measuring on SiN windows has several other advantages. First, measuring on such

a small aperture enables to study very fragile composite membrane that cannot withstand being self-supported on centimetric apertures. Second, Pressure drop measurements can be made (see appendix) without breaking the membrane which is not possible with centimetric aperture. Lastly, the small-cell in which the SiN windows are loaded enables changing the reservoir's solution without moving the membranes which makes the measurements easier.

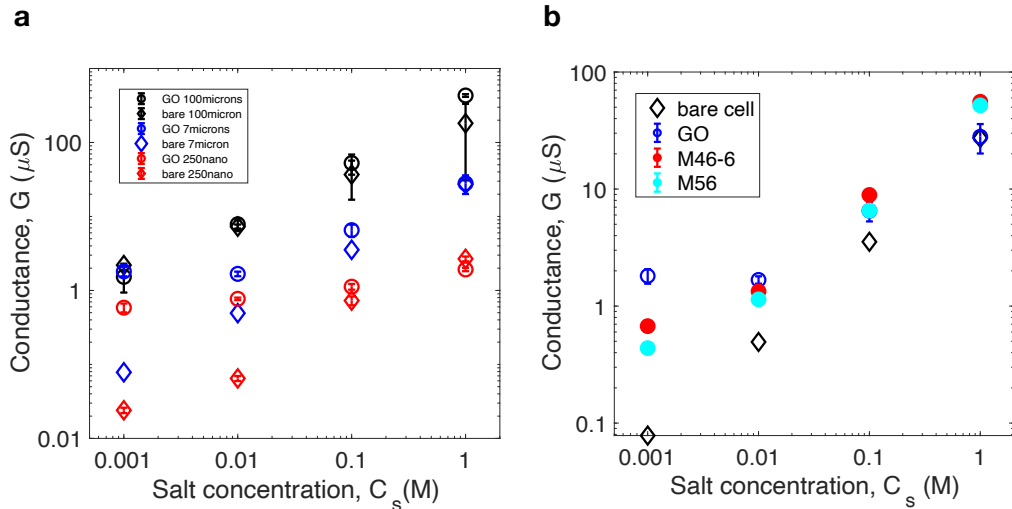


Figure D.3

Measuring macro-scale membrane conductance using SiN windows. **a**, Benchmarking. The diamonds are measurements without GO membranes and the circles are a measurements with a GO membranes. Each color indicate a different SiN window aperture. **b**, Comparing different membranes using SiN windows of 7 microns. We compare GO membranes, GO with titanium titanium (M56) and GO with titanium and anatase (M46-6).

A main drawback of measuring on micrometric aperture is that the effective membrane area is unknown. For centimetric aperture the ratio between suspended membrane area and total membrane area is close to one but for the case of a micrometer aperture it is much lower than one. Hence the effective area for a centimetric aperture can be safely taken as the aperture's but for a micrometer area, as there is likely transversal conduction further away from the aperture this assumption can not safely be made. Therefore this methods of measuring can be used to compare membranes between each other but would require further improvements and rationalization to perform modeling and extract conductivity and eventually surface properties' values.

We test power generation using graphene oxide membranes deposited on a SiN windows. As shown in Figure D.4.a, it is possible to generate power using this setup. The generated power is of maximum 37nW. This corresponds to power densities ranging from $1e-3$ to 1 W/m² depending on the considered effective area (Considering the full membrane area or only the suspended area). This is 5 to 8 orders of magnitude lower than what was obtained with activated carbon nanochannels.

As stated above, the setup needs further rationalization to estimate the effective membrane area to avoid having a three orders of magnitude uncertainty range. Regardless of this aspect, 10 microns-thick GO *per se* cannot be used to upscale activated carbon nanochannels. Further efforts are required in membrane architecture as well as cell development to reduce the loss. Interestingly the osmotic's current negative sign suggests that the power generation in graphene oxide may be caused by a forward osmosis mechanism where the flux of water goes the opposite way as diffuse-osmosis (In forward osmosis water goes from the diluted to concentrated reservoir). This is consistent with direct water flow measurements showing a depletion of water volume in the low concentration reservoir (Figure D.4.b).

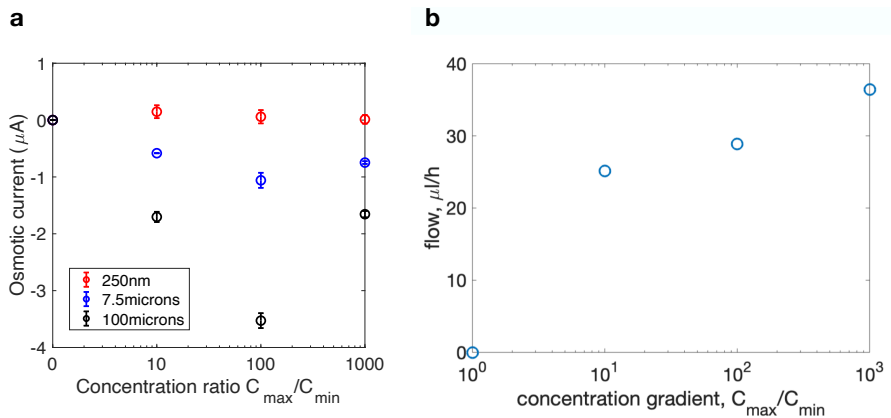


Figure D.4

Power generation with graphene oxide deposited on SiN membranes a, Osmotic current vs concentration gradient for various aperture lengthscales. We use the same expression than in chapter 7 to obtain the values of the osmotic current : $I_{osm} = I_{offset} - \Delta V_{Nernst} \times G$. **b**, Flux obtain at various concentration gradient for a graphene oxide membranes (10 microns thickness) deposited on a SiN window with aperture of 100microns. The flow is read by connecting graduated capillaries to the cell's reservoirs and performing in-time volumetric measurements.

Data for the memory effect

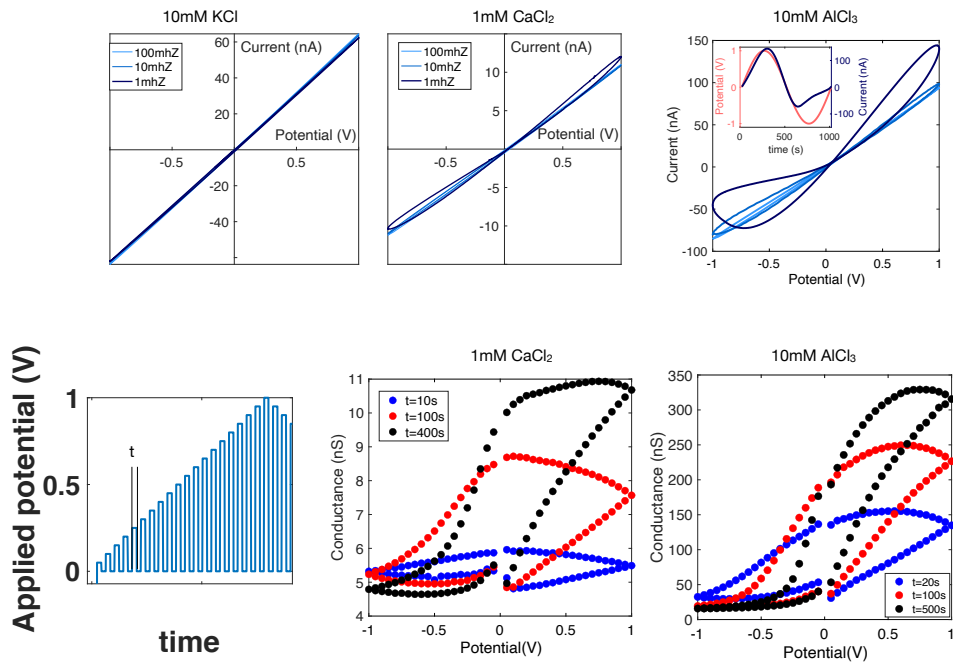


Figure E.1

System A ($N=4$, $h \simeq 5nm$)

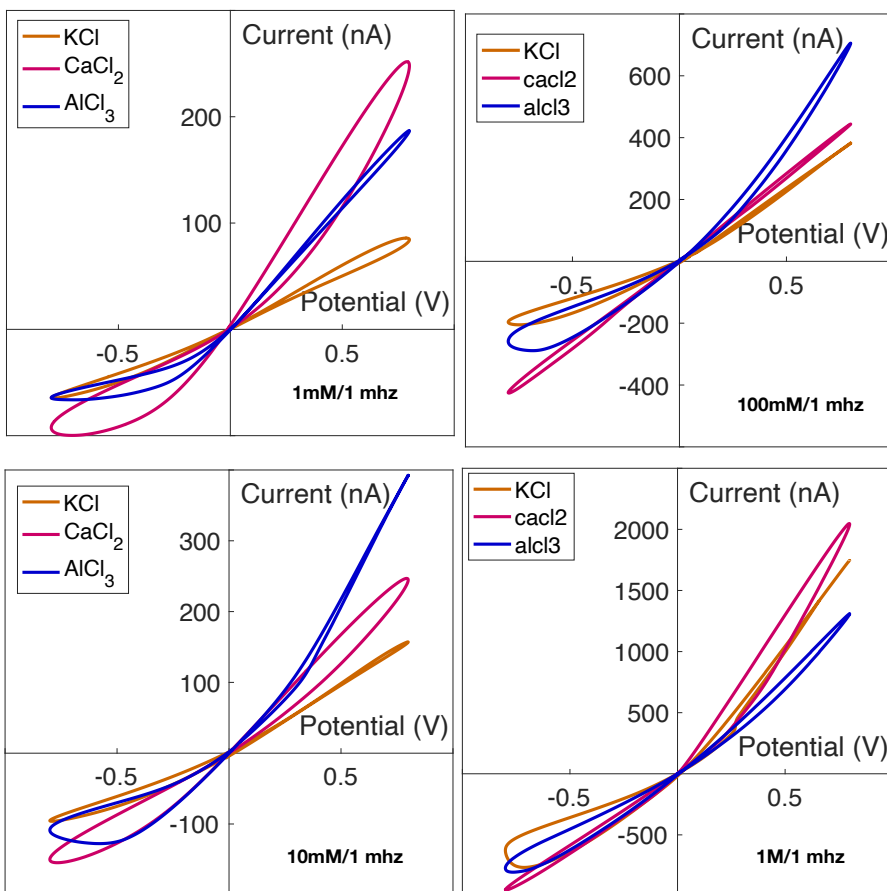
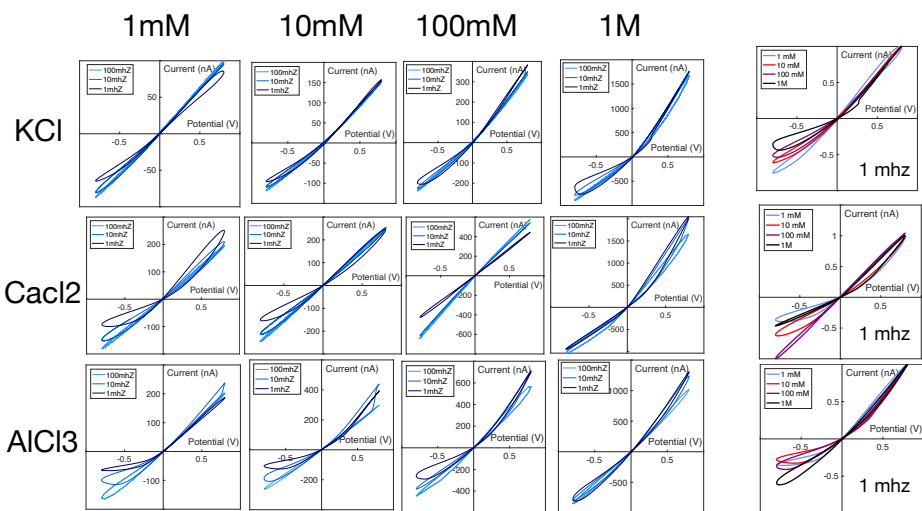


Figure E.2

System B ($N=3$, $h \approx 13nm$). The concentrations master plot are normalized

CaCl₂

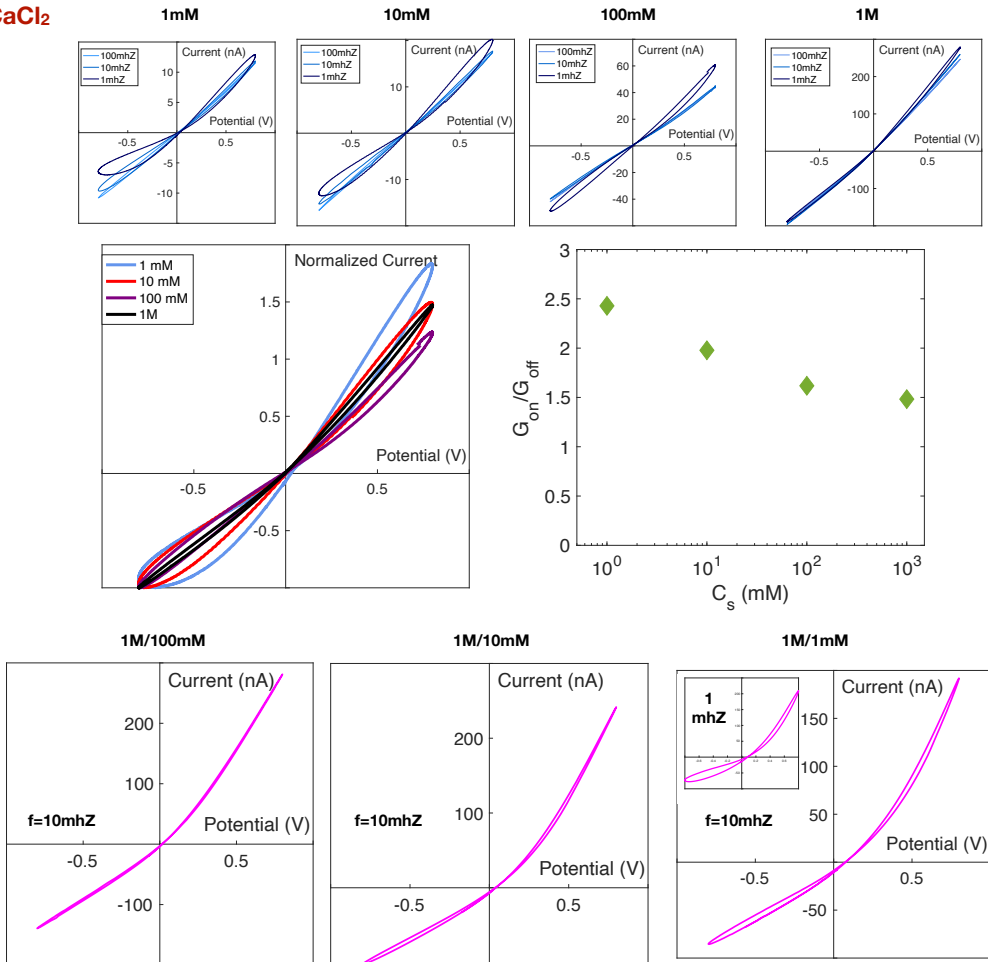


Figure E.3

System C ($N=1$, $h \approx 12\text{nm}$)

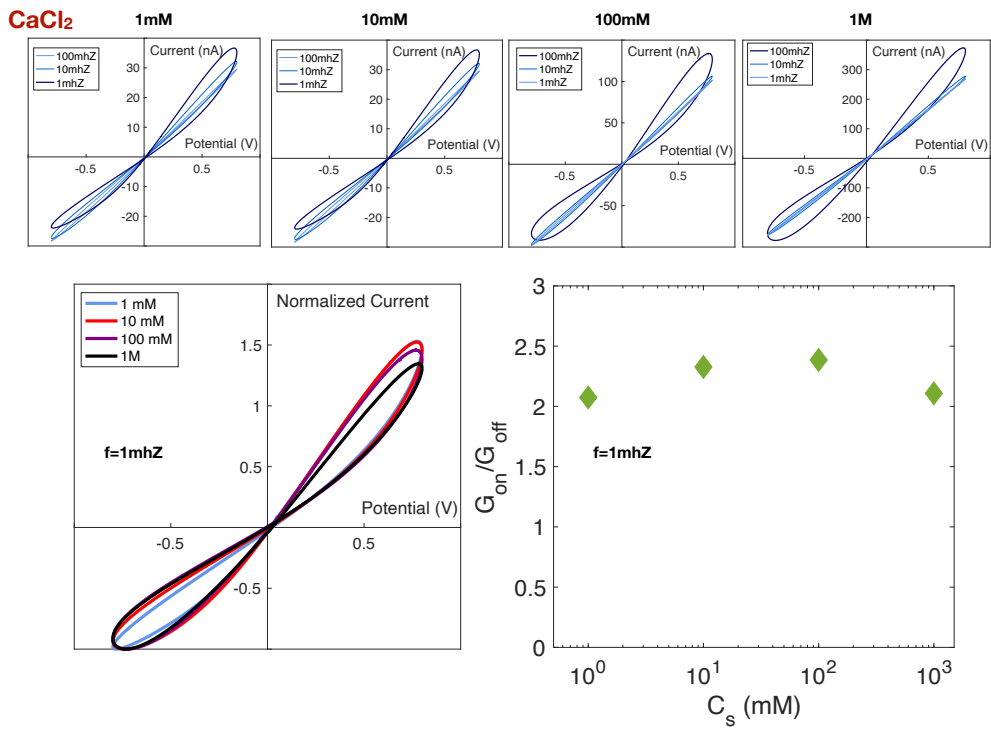


Figure E.4

System D ($N=4$, $h \simeq 5\text{nm}$)

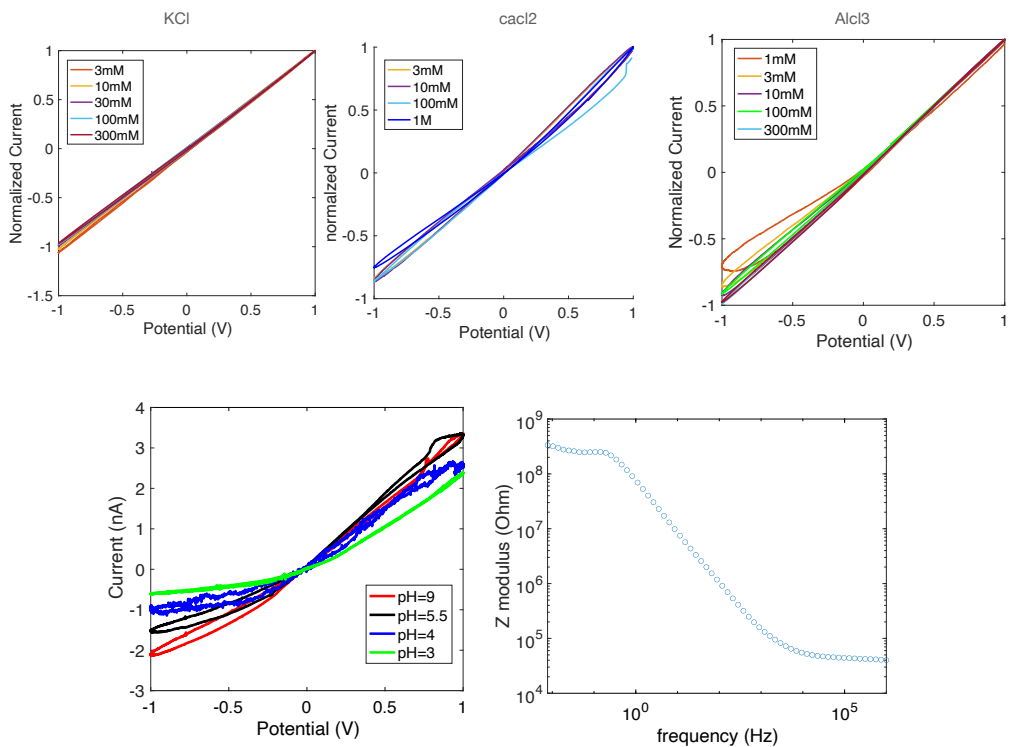


Figure E.5

Additional graphite device (System E) ($N=4$, $h \simeq 10nm$). pH and impedancemeter measurements: 1mM $AlCl_3$

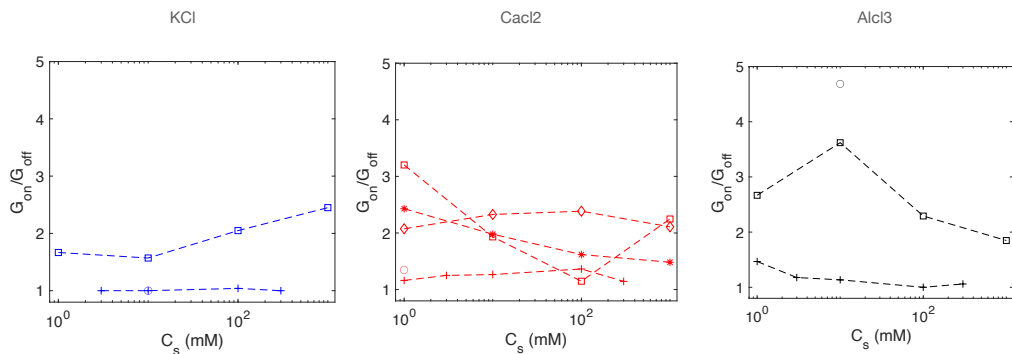


Figure E.6

Masterplot. System A: circles, System B : squares, System C : Diamonds, System D : stars, System E: cross

Model for the memory effect (by P.Robin)

Here we try to find a minimal model accounting for the low-frequency memristor effect found in graphitic nanochannels. We first show how asymmetric entrance effects can be at the source of the conductance switching, and then how surface effects can slow the process down, giving rise to long-term memory.

F.1 Qualitative discussion

Nanofluidic memristors exhibit current rectification: when a positive voltage is applied, the conductance tends to increase, and conversely for a negative voltage. One usually refers to this as the ‘polarity’ of the memristor. This indicates that there is some asymmetry at the source of the memristor effect. Since it is also observed in atomically smooth (and thus perfectly symmetric) nanochannels, the only possible source of asymmetry is the connections between the reservoirs and the device (which are asymmetric by design: the SiN membrane is only on one side). This raises two points:

- Do all nanofluidic memristors have the same polarity (ie. have their conductance increased for a positive voltage, with the ground electrode on the side of the SiN membrane)?
- What about non-2D channels with the same asymmetry?

If this picture holds, then one can explain the memristor effect qualitatively. The system bears a very high negative charge, and its entrances are asymmetric. Due to the geometry, ions have a harder time flowing through the entry on the side of the SiN membrane. When we apply a positive voltage with the ground on the side of the membrane, the electric field is in the direction of the membrane. Due to the high negative charge, conduction occurs through the motion of positive ions mainly. They flow in easily, but have a hard time flowing out: they accumulate and the average concentration inside the system rises, and with it the conductance. For the same reasons, the conductance is lowered for a negative voltage as the system is depleted instead.

Note that the above discussion does not explain why the accumulation/depletion is stable over long timescales once the voltage is removed.

A first remark is that this picture is very general as long as there is some kind of asymmetry. Another asymmetry source, which is much easier to control, would be

to impose different concentrations in the reservoirs. Entrance effects are notoriously hard to model, and actually we do not need a very precise description to understand what is going on. All that matters is the fact that for the same electric field, the currents at both entrance are not equivalent. This motivates the minimal model introduced in next section.

F.2 1D model

In this section, we consider a 1D channel of length L , with diffusion coefficient D . It is connected to two infinite reservoirs at $x = 0$ and $x = L$. They contain an average concentration c_L and c_R , respectively. An external forcing (eg. a voltage drop) creates a flux across the system.

The concentration profile $c(x, t)$ follows the Fokker-Planck equation:

$$\partial_t c = D \partial_{xx} c + \frac{D}{k_B T} \partial_x [c \partial_x \mathcal{U}], \quad (\text{F.1})$$

where $\mathcal{U}(x, t)$ is the external potential (eg. electrical potential). For the sake of simplicity, we assume $\mathcal{U}(x) = -fx$, with f a force. We first assume it is constant, then look at time-dependent effects.

In the following, we work in dimensionless units, where $D = L = k_B T = 1$.

F.2.1 Model discussion

To come up with this model, we made several important simplifications. First, we discarded any interaction between particles, and considered only one type of particles (no positive/negative ions). We also simplified the geometry to a 1D model, and replaced the entrance effects to a simple boundary condition of the form $c(x = 0) = c_L$.

This can be motivated in the following fashion. Let us assume that the entrances are asymmetric, such that an ion has to pay an energy E_L for entering from the left and E_R from the right. Then, if both reservoirs contain a concentration c_0 , the boundary condition will read:

$$c(x = 0) = c_0 e^{-E_L/k_B T} = c_L \quad ; \quad c(x = L) = c_0 e^{-E_R/k_B T} = c_R. \quad (\text{F.2})$$

What we lose, however, in applying such boundary conditions, are the diffusion effects in the reservoirs.

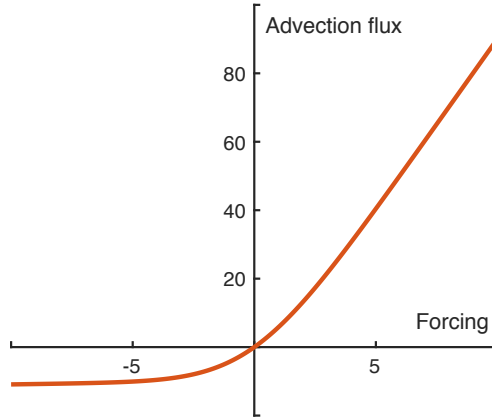
F.2.2 Constant forcing: current rectification

Here we assume that f is a constant. The solution can be obtained by direct integration of the Fokker-Planck equation, yielding:

$$c(x \in [0, 1]) = \frac{c_R - c_L}{e^f - 1} e^{fx} - \frac{c_R - c_L e^f}{e^f - 1}, \quad (\text{F.3})$$

The resulting current is:

$$j = -\partial_x c - c \partial_x \mathcal{U} = \frac{c_L e^f - c_R}{e^f - 1} f. \quad (\text{F.4})$$


Figure F.1

Drift part of the particle flux $j_f = j - j_D$ as function of external forcing f , exhibiting current rectification for $c_L = 10$ and $c_R = 0.1$.

This result is plotted on Fig 1 for $c_L > c_R$. The conductance of the system has two states: for $j > 0$, particles flowing through the system come from the high concentration side: the channel is filled (for large j , $c \simeq c_L$). For $j < 0$, particles come from the low concentration side and $c \simeq c_R$: the channel is depleted.

Note that j contains two terms: a purely diffusive term (which vanishes if $c_L = c_R$), and a drift term (which vanishes for $f = 0$). It can be made apparent in the following form:

$$j = \left(\frac{c_L e^f - c_R}{e^f - 1} - \frac{c_L - c_R}{f} \right) f + (c_L - c_R) = j_f + j_D. \quad (\text{F.5})$$

One can also rewrite the drift flux j_f in the following way:

$$j_f = c_x f, \quad (\text{F.6})$$

with c_x the spatial average of the concentration. This is the component of the current we are interested into, so in what follows we always subtract j_D to results to retain the drift part of the flux only.

F.2.3 Time-varying forcing: qualitative discussion

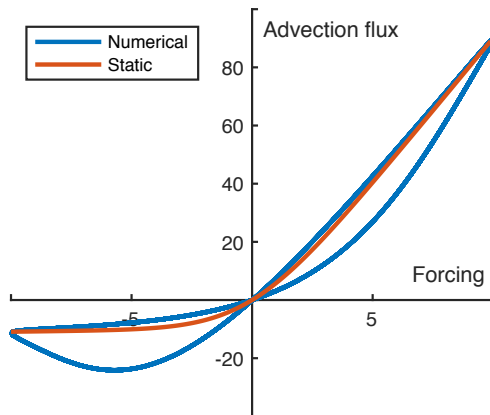
We now assume that the forcing depends on time, for example:

$$f = f_0 \cos \omega t. \quad (\text{F.7})$$

We thus have to solve:

$$\partial_t c = \partial_{xx} c - f_0 \partial_x c \cos \omega t. \quad (\text{F.8})$$

Sadly, there is no closed-form solution, even in the simple case where we only consider the permanent regime. However, a qualitative discussion can help us to get some quantitative estimates.

**Figure F.2**

Pinched IV curve for time-varying curve, from numerical simulations. Blue curve: time-dependent solution, from finite-volumes numerical integration. The drift flux is obtained by computing the spatial average of the concentration at each time step. Red curve: static solution. Remark: we subtracted the constant diffusion flux j_D , which simply shifts the curve upwards. Dimensionless units ($k_B T = D = L = 1$) with $f_0 = 10$ and $\omega = 2\pi$.

The first remark that needs to be made is that, in a time-varying regime, there is no flux conservation a priori and one cannot define a global flux j . An important question is thus: what do electrodes measure? Since there is one electrode on each side, we probably measure something like:

$$I \sim \frac{1}{2}(j_{\text{left}} + j_{\text{right}}), \quad (\text{F.9})$$

ie., a mean of the two currents at the entries. For the sake of simplicity, we assume:

$$I \sim j(x, t)_x = -\partial_x c - c \partial_x \mathcal{U}_x = (c_L - c_R) + c(x, t)_x f(t). \quad (\text{F.10})$$

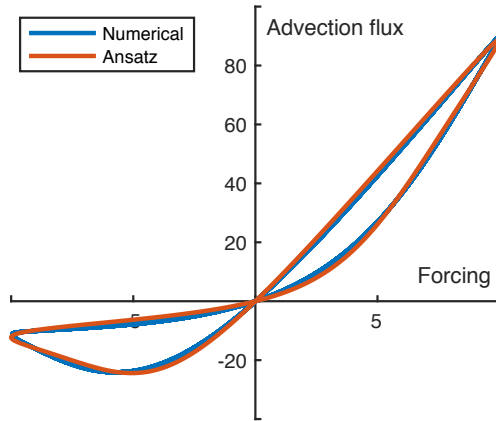
We now solve the advection-diffusion equation using a home-made finite volumes codes. Numerical results show that these two definitions of the ionic current I give the same results with very good precision.

Now, again using numerical simulations, we plot $I(t) - j_D$ as a function of $f(t)$, see Fig. 2. We see that the two conductance states tend to “pollute” each other, opening the IV curve. This is easily understandable, as depleting or populating the system with particles takes time, and thus the system’s state is lagging behind the forcing.

F.2.4 A simple ansatz

The above remark gives us an intuition of what should be the correct expression of the ionic current:

$$I_{\text{time dependent}} = f(t) \frac{1}{\tau} \int_0^t e^{-\frac{t-s}{\tau}} c[f(s)] ds, \quad (\text{F.11})$$


Figure F.3

Numerical solution versus simple ansatz, here with $\tau = 0.08$ and other parameters like in Fig. 2.

where by $c[f]$ we mean the average concentration in the static case with a forcing f . The time τ is a memory parameter. See the Appendix.

We compare this ansatz to the numerical solution (Fig. 3) by fitting a value for τ . The agreement is excellent, but it is hard to theoretically predict the correct expression for τ . I tried to do a perturbative expansion in Fourier space, but it did not yield good results.

Note that τ depends on ω . One can define a universal (frequency-independent) memory time T_m with the following:

$$T_m = \frac{2\pi}{\omega^*} \quad ; \quad \omega^* = \operatorname{argmax}_{\omega} \omega\tau(\omega). \quad (\text{F.12})$$

While useful in numerical simulations, this definition does not help theoretical understanding. In order to make progress, we turn to an even simpler model.

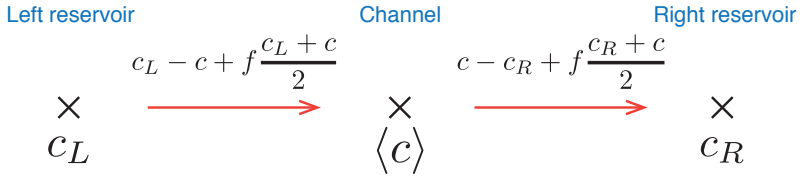
F.3 Minimal model: 0D model

We now consider an even simpler model consisting of three “sites”: the left reservoir (concentration c_L), the middle of the channel (concentration c) and the right reservoir (concentration c_R), see Fig. 4. For the sake of simplicity, we drop the brackets around c . Note that this model corresponds to a finite-volumes scheme with just one point. Following this representation, we obtain a simple differential equation:

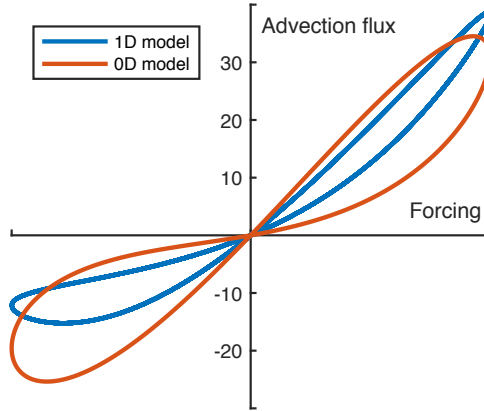
$$\frac{1}{2}\dot{c} + c = \frac{c_L + c_R}{2} + f(t)\frac{c_L - c_R}{4}. \quad (\text{F.13})$$

This equation is so simple that there is an exact analytical solution for $f(t) = f_0 \cos \omega t$:

$$C \equiv c - \frac{c_L + c_R}{2} = f_0 \frac{c_L - c_R}{2} \frac{2 \cos \omega t + \omega \sin \omega t}{4 + \omega^2}. \quad (\text{F.14})$$


Figure F.4

Schematic representation of the 0D model.


Figure F.5

Numerical solution of the advection-equation versus the 0D model, for the set of parameters as other figures, except that $f_0 = 5$.

The result is plotted on Fig. 5.

Let us now extract an analytical memory time from this result. The concentration C presents an hysteresis cycle when f varies. The effect of the memory can be quantified by computing the area of the circle:

$$\mathcal{A} = - \oint C df = \int_0^{\frac{2\pi}{\omega}} \omega C(t) \sin \omega t dt = f_0 \frac{c_L - c_R}{2} \frac{\omega}{4 + \omega^2}. \quad (\text{F.15})$$

Then we define the memory time as follows:

$$T_m = \frac{2\pi}{\omega^*} \quad ; \quad \omega^* = \operatorname{argmax}_{\omega} \mathcal{A}(\omega). \quad (\text{F.16})$$

In other words, the memory time corresponds to the frequency that maximizes the area of the hysteresis cycle. We obtain:

$$T_m = \pi. \quad (\text{F.17})$$

In dimensional terms, this means:

$$T_m = \frac{\pi L^2}{D}. \quad (\text{F.18})$$

This result is of course trivial: that is the diffusion timescale. For ThÃ©o's devices, with $L = 5 - 10 \mu\text{m}$, we obtain:

$$T_m = 0.3 \text{ s}. \quad (\text{F.19})$$

In other words, there is no memory on experimental-relevant timescales.

F.4 Dukhin slowdown

We now present a slightly modified model that accounts for the long memory timescales in activated channels. We consider a 4-site model, with the fourth site describing the surface of the channel, where particles may adsorb, see Fig. 6. The absorption rate is k , and the desorption rate is λ . We assume that adsorbed particles do not move and thus do not yield any particle flux.

Intuitively, doing this introduces two new timescales k^{-1} and λ^{-1} . But, as we will now show, the memory time can actually be much larger than π (diffusion-limited regime), k and λ ! Let s be the concentration of adsorbed particles. One has:

$$\dot{c} + 2c = c_L + c_R + f(t) \frac{c_L - c_R}{2} - kc + \lambda s, \quad (\text{F.20})$$

$$\dot{s} = kc - \lambda s. \quad (\text{F.21})$$

$$(\text{F.22})$$

Introducing $C = c - c_\infty$ and $S = s - s_\infty$, one obtains:

$$\dot{C} + 2C = -kC + \lambda S + f(t) \frac{c_L - c_R}{2}, \quad (\text{F.23})$$

$$\dot{S} = kC - \lambda S. \quad (\text{F.24})$$

This model can again be solved analytically:

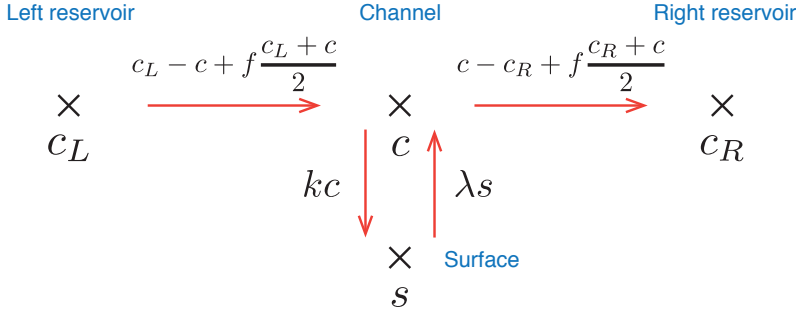
$$C(t) = f \frac{c_L - c_R}{2} \frac{[4\lambda^2 + (2+k)\omega^2] \cos \omega t + \omega [\lambda(k+\lambda) + \omega^2] \sin \omega t}{4\lambda^2 + [(2+k)^2 + 2k\lambda + \lambda^2] \omega^2 + \omega^4}, \quad (\text{F.25})$$

$$S(t) = kf \frac{c_L - c_R}{2} \frac{(2\lambda + \omega^2) \cos \omega t + \omega(2+k+\lambda) \sin \omega t}{4\lambda^2 + [(2+k)^2 + 2k\lambda + \lambda^2] \omega^2 + \omega^4}. \quad (\text{F.26})$$

The area of the hysteresis cycle is given by the sine term of the first equation. The memory frequency ω^* verifies:

$$\{\lambda(k+\lambda) + \omega^2 + 2\omega^2\lambda(\lambda+k)\} [4\lambda^2 + \{(a+k)^2 + 2k\lambda + \lambda^2\} \omega^2 + \omega^4] \quad (\text{F.27})$$

$$\dots = \omega \{\lambda(k+\lambda) + \omega^2\} [2 \{(a+k)^2 + 2k\lambda + \lambda^2\} \omega + 4\omega^3] \quad (\text{F.28})$$


Figure F.6

Schematic representation of the 0D model with surface effects.

There is no closed form solution to this equation in general. However, we can extract interesting limiting cases. Notably, we consider the limit where surface effects are predominant, that is $k \gg 1 \gg \lambda$. Assuming $\omega^* \ll 1$ yields the scaling law:

$$\omega^* \sim 2^{-1/2} \frac{\lambda}{k} \sim \frac{c_\infty}{s_\infty}. \quad (\text{F.29})$$

In other words, the (dimensional) memory time is:

$$T_m = 2\pi \text{Du} \frac{L^2}{D}, \quad (\text{F.30})$$

where $\text{Du} = s_\infty/c_\infty$ is the analogue of the Dukhin number. We see that the predominance of surface effects induces a slowdown of the dynamics, the memory time being increased by a factor 2Du .

Activated channels have a length $L \sim 10 \mu\text{m}$, with surface charge $\Sigma \sim 1 \text{ C/m}^2$ and concentration $\sim 1 \text{ mM}$. This yields $\text{Du} \sim 10^3$. We obtain:

$$\boxed{T_m \sim 10 \text{ min}} \quad (\text{F.31})$$

Appendix: An approximation method

Consider:

$$\dot{y} = -a(t)y + b(t). \quad (\text{F.32})$$

Quasi-static solution:

$$y_{\text{qs}}(t) = \frac{b(t)}{a(t)}. \quad (\text{F.33})$$

Homogeneous solution:

$$y_h(t) = \lambda e^{-A(t)}, \quad (\text{F.34})$$

with A the primitive of a such that $A(0) = 0$. Permanent regime solution:

$$y(t) = e^{-A(t)} \int_0^t e^{A(s)} b(s) ds. \quad (\text{F.35})$$

If A grows sufficiently fast, then this last integral is dominated by terms such that $s \simeq t$. Then,

$$A(s) - A(t) \simeq -(t - s)a(t), \quad (\text{F.36})$$

and values of s that contribute are localized between $t - \tau$ and t , with:

$$\tau = \frac{1}{a(t)}. \quad (\text{F.37})$$

We then obtain:

$$y(t) \simeq \frac{1}{\tau} \int_0^t e^{-\frac{t-s}{\tau}} y_{\text{qs}}(s) \, ds. \quad (\text{F.38})$$

Data for the synaptic plasticity

Here the voltages input are programmed via *MATLAB* and read as a vector by *LABVIEW*.

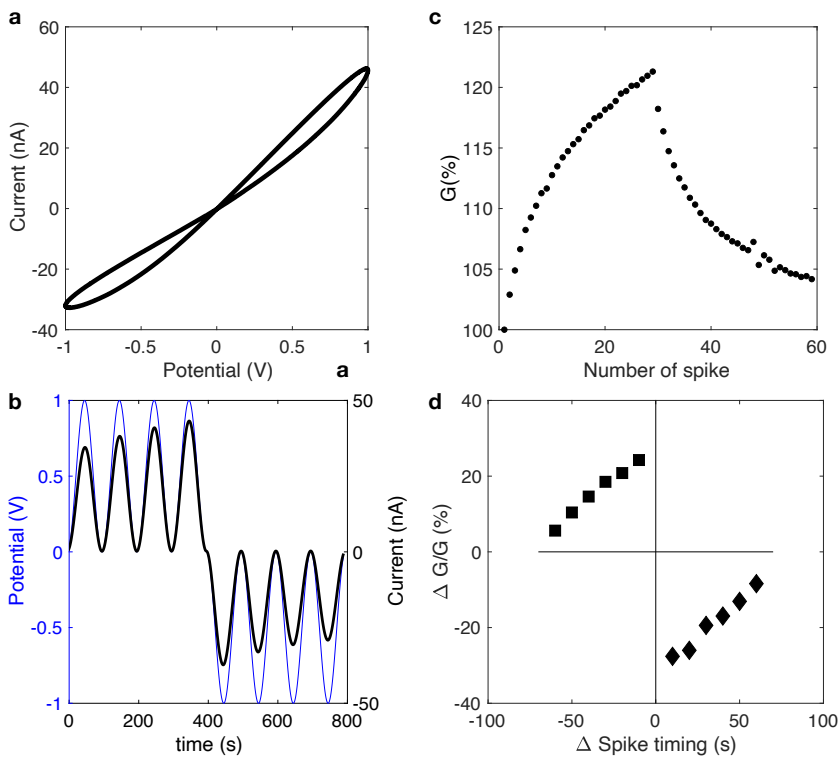


Figure G.1

System A ($N=4$, $h \simeq 5nm$). **a**, IV characteristics. **b**, Synaptic behaviour. **c** Reversible strengthening of the nanochannel. **d**, Hebb's rule. Everything is measured with $CaCl_2$ at 1mM

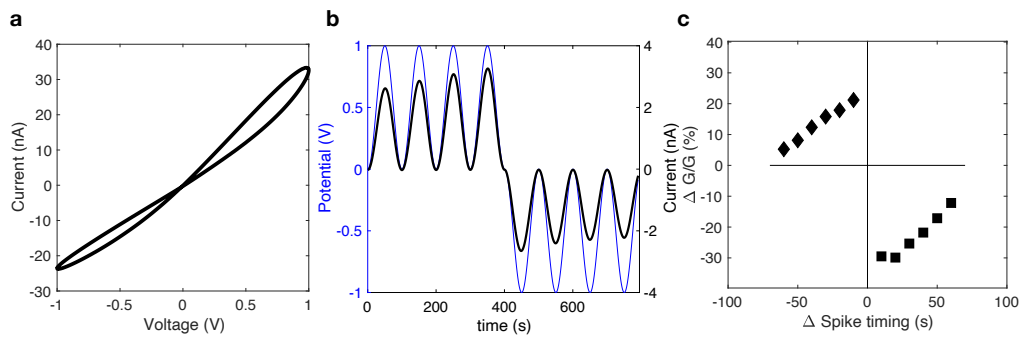


Figure G.2

System B ($N=4$, $h \simeq 5nm$). **a**, IV characteristics. **b**, Synaptic behaviour. **c**, Hebb's rule. Everything is measured with $CaCl_2$ at 1mM.

Bibliography

- [1] Kavokine, N., Netz, R. R. & Bocquet, L. Fluids at the nanoscale: From continuum to subcontinuum transport. *Annual Review of Fluid Mechanics* **53**, 377–410 (2021).
- [2] Bocquet, L. & Charlaix, E. Nanofluidics, from bulk to interfaces. *Chemical Society Reviews* **39**, 1073–1095 (2010).
- [3] Ali, A., Tufa, R. A., Macedonio, F., Curcio, E. & Drioli, E. Membrane technology in renewable-energy-driven desalination. *Renewable and Sustainable Energy Reviews* **81**, 1–21 (2018).
- [4] Shenvi, S. S., Isloor, A. M. & Ismail, A. A review on ro membrane technology: Developments and challenges. *Desalination* **368**, 10–26 (2015).
- [5] Ersahin, M. E. *et al.* A review on dynamic membrane filtration: materials, applications and future perspectives. *Bioresource technology* **122**, 196–206 (2012).
- [6] Pronk, W. *et al.* Gravity-driven membrane filtration for water and wastewater treatment: a review. *Water research* **149**, 553–565 (2019).
- [7] Kim, J., Jeong, K., Park, M. J., Shon, H. K. & Kim, J. H. Recent advances in osmotic energy generation via pressure-retarded osmosis (pro): A review. *Energies* **8**, 11821–11845 (2015).
- [8] Marbach, S. & Bocquet, L. Osmosis, from molecular insights to large-scale applications. *Chemical Society Reviews* **48**, 3102–3144 (2019).
- [9] Lee, K. P., Arnot, T. C. & Mattia, D. A review of reverse osmosis membrane materials for desalination—development to date and future potential. *Journal of Membrane Science* **370**, 1–22 (2011).
- [10] Kang, G.-d. & Cao, Y.-m. Development of antifouling reverse osmosis membranes for water treatment: a review. *Water research* **46**, 584–600 (2012).
- [11] Deshmukh, A. *et al.* Membrane distillation at the water-energy nexus: limits, opportunities, and challenges. *Energy & Environmental Science* **11**, 1177–1196 (2018).
- [12] Gouaux, E. & MacKinnon, R. Principles of selective ion transport in channels and pumps. *science* **310**, 1461–1465 (2005).

-
- [13] Lynch, C. I., Rao, S. & Sansom, M. S. Water in nanopores and biological channels: A molecular simulation perspective. *Chemical Reviews* **120**, 10298–10335 (2020).
- [14] Murata, K. *et al.* Structural determinants of water permeation through aquaporin-1. *Nature* **407**, 599–605 (2000).
- [15] Dodson, P. D. & Forsythe, I. D. Presynaptic k^+ channels: electrifying regulators of synaptic terminal excitability. *Trends in neurosciences* **27**, 210–217 (2004).
- [16] Catterall, W. A. Voltage-gated calcium channels. *Cold Spring Harbor perspectives in biology* **3**, a003947 (2011).
- [17] Li, J. *et al.* Ion-beam sculpting at nanometre length scales. *Nature* **412**, 166–169 (2001).
- [18] Huh, D. *et al.* Tuneable elastomeric nanochannels for nanofluidic manipulation. *Nature materials* **6**, 424–428 (2007).
- [19] Xie, Y. *et al.* Electric energy generation in single track-etched nanopores. *Applied Physics Letters* **93**, 163116 (2008).
- [20] Liu, S. *et al.* Fast and controllable fabrication of suspended graphene nanopore devices. *Nanotechnology* **23**, 085301 (2012).
- [21] Holt, J. K. *et al.* Fast mass transport through sub-2-nanometer carbon nanotubes. *Science* **312**, 1034–1037 (2006).
- [22] Karnik, R. *et al.* Electrostatic control of ions and molecules in nanofluidic transistors. *Nano letters* **5**, 943–948 (2005).
- [23] Radha, B. *et al.* Molecular transport through capillaries made with atomic-scale precision. *Nature* **538**, 222–225 (2016).
- [24] Gopinadhan, K. *et al.* Complete steric exclusion of ions and proton transport through confined monolayer water. *Science* **363**, 145–148 (2019).
- [25] Fumagalli, L. *et al.* Anomalously low dielectric constant of confined water. *Science* **360**, 1339–1342 (2018).
- [26] Mousterde, T. *et al.* Molecular streaming and its voltage control in ångström-scale channels. *Nature* **567**, 87–90 (2019).
- [27] Esfandiar, A. *et al.* Size effect in ion transport through angstrom-scale slits. *Science* **358**, 511–513 (2017).
- [28] Novoselov, K. S. *et al.* Electric field effect in atomically thin carbon films. *science* **306**, 666–669 (2004).
- [29] Geim, A. K. & Grigorieva, I. V. Van der waals heterostructures. *Nature* **499**, 419–425 (2013).
- [30] Ni, Z. *et al.* Graphene thickness determination using reflection and contrast spectroscopy. *Nano letters* **7**, 2758–2763 (2007).
- [31] Secchi, E. *et al.* Massive radius-dependent flow slippage in carbon nanotubes. *Nature* **537**, 210–213 (2016).

-
- [32] Marcotte, A., Mouterde, T., Niguès, A., Siria, A. & Bocquet, L. Mechanically activated ionic transport across single-digit carbon nanotubes. *Nature Materials* **19**, 1057–1061 (2020).
- [33] Kavokine, N., Robert, A., Bocquet, M.-L. & Bocquet, L. Fluctuation-induced quantum friction in nanoscale water flows. *arXiv preprint arXiv:2105.03413* (2021).
- [34] Chen, B. *et al.* How good can cvd-grown monolayer graphene be? *Nanoscale* **6**, 15255–15261 (2014).
- [35] Graphenium flakes. <https://www.graphit.de/en/graphite-sales>. Accessed: 2021-08-23.
- [36] Garaj, S. *et al.* Graphene as a subnanometre trans-electrode membrane. *Nature* **467**, 190–193 (2010).
- [37] Bandurin, D. *et al.* Negative local resistance caused by viscous electron backflow in graphene. *Science* **351**, 1055–1058 (2016).
- [38] Kidambi, P. R. *et al.* Facile fabrication of large-area atomically thin membranes by direct synthesis of graphene with nanoscale porosity. *Advanced Materials* **30**, 1804977 (2018).
- [39] Jiang, T., Kravtsov, V., Tokman, M., Belyanin, A. & Raschke, M. B. Ultrafast coherent nonlinear nanooptics and nanoimaging of graphene. *Nature nanotechnology* **14**, 838–843 (2019).
- [40] Nair, R., Wu, H., Jayaram, P., Grigorieva, I. & Geim, A. Unimpeded permeation of water through helium-leak-tight graphene-based membranes. *Science* **335**, 442–444 (2012).
- [41] Chen, L. *et al.* Ion sieving in graphene oxide membranes via cationic control of interlayer spacing. *Nature* **550**, 380–383 (2017).
- [42] Li, X., Zhu, B. & Zhu, J. Graphene oxide based materials for desalination. *Carbon* **146**, 320–328 (2019).
- [43] Zhang, Z. *et al.* Vertically transported graphene oxide for high-performance osmotic energy conversion. *Advanced Science* **7**, 2000286 (2020).
- [44] Ghanbari, H. & Esfandiari, A. Ion transport through graphene oxide fibers as promising candidate for blue energy harvesting. *Carbon* **165**, 267–274 (2020).
- [45] Lanyon, Y. H. *et al.* Fabrication of nanopore array electrodes by focused ion beam milling. *Analytical chemistry* **79**, 3048–3055 (2007).
- [46] Tian, Z.-P., Lu, K. & Chen, B. Unique nanopore pattern formation by focused ion beam guided anodization. *Nanotechnology* **21**, 405301 (2010).
- [47] Vieu, C. *et al.* Electron beam lithography: resolution limits and applications. *Applied surface science* **164**, 111–117 (2000).
- [48] Yuzvinsky, T., Fennimore, A., Mickelson, W., Esquivias, C. & Zettl, A. Precision cutting of nanotubes with a low-energy electron beam. *Applied Physics Letters* **86**, 053109 (2005).

-
- [49] Thiele, C. *et al.* Electron-beam-induced direct etching of graphene. *Carbon* **64**, 84–91 (2013).
- [50] ToanáTran, T., HuaáLi, L. *et al.* Electron beam directed etching of hexagonal boron nitride. *Nanoscale* **8**, 16182–16186 (2016).
- [51] Feng, J. *et al.* Electrochemical reaction in single layer mos2: nanopores opened atom by atom. *Nano letters* **15**, 3431–3438 (2015).
- [52] Storm, A., Chen, J., Ling, X., Zandbergen, H. & Dekker, C. Fabrication of solid-state nanopores with single-nanometre precision. *Nature materials* **2**, 537–540 (2003).
- [53] Feng, J. *et al.* Observation of ionic coulomb blockade in nanopores. *Nature materials* **15**, 850–855 (2016).
- [54] Feng, J. *et al.* Identification of single nucleotides in mos 2 nanopores. *Nature nanotechnology* **10**, 1070–1076 (2015).
- [55] Feng, J. *et al.* Single-layer mos 2 nanopores as nanopower generators. *Nature* **536**, 197–200 (2016).
- [56] Lee, C. Y., Choi, W., Han, J.-H. & Strano, M. S. Coherence resonance in a single-walled carbon nanotube ion channel. *Science* **329**, 1320–1324 (2010).
- [57] Siria, A. *et al.* Giant osmotic energy conversion measured in a single transmembrane boron nitride nanotube. *Nature* **494**, 455–458 (2013).
- [58] Secchi, E., Niguès, A., Jubin, L., Siria, A. & Bocquet, L. Scaling behavior for ionic transport and its fluctuations in individual carbon nanotubes. *Physical review letters* **116**, 154501 (2016).
- [59] Stein, D., Kruithof, M. & Dekker, C. Surface-charge-governed ion transport in nanofluidic channels. *Physical Review Letters* **93**, 035901 (2004).
- [60] Keerthi, A. *et al.* Ballistic molecular transport through two-dimensional channels. *Nature* **558**, 420–424 (2018).
- [61] Yang, W. *et al.* Translocation of dna through ultrathin nanoslits. *Advanced Materials* **33**, 2007682 (2021).
- [62] Keerthi, A. *et al.* Water friction in nanofluidic channels made from two-dimensional crystals. *Nature communications* **12**, 1–8 (2021).
- [63] Thiele, C. *et al.* Electron-beam-induced direct etching of graphene. *Carbon* **64**, 84–91 (2013).
- [64] Martin, A. A., McCredie, G. & Toth, M. Electron beam induced etching of carbon. *Applied Physics Letters* **107**, 041603 (2015).
- [65] Grosjean, B., Bocquet, M.-L. & Vuilleumier, R. Versatile electrification of two-dimensional nanomaterials in water. *Nature communications* **10**, 1–8 (2019).
- [66] Xie, Q. *et al.* Fast water transport in graphene nanofluidic channels. *Nature nanotechnology* **13**, 238–245 (2018).

-
- [67] Mouterde, T. & Bocquet, L. Interfacial transport with mobile surface charges and consequences for ionic transport in carbon nanotubes. *The European physical journal E* **41**, 1–10 (2018).
- [68] Xie, Y., Fu, L., Niehaus, T. & Joly, L. Liquid-solid slip on charged walls: the dramatic impact of charge distribution. *Physical Review Letters* **125**, 014501 (2020).
- [69] Siria, A., Bocquet, M.-L. & Bocquet, L. New avenues for the large-scale harvesting of blue energy. *Nature Reviews Chemistry* **1**, 1–10 (2017).
- [70] Siria, A., Bocquet, M.-L. & Bocquet, L. New avenues for the large-scale harvesting of blue energy. *Nature Reviews Chemistry* **1**, 1–10 (2017).
- [71] Logan, B. E. & Elimelech, M. Membrane-based processes for sustainable power generation using water. *Nature* **488**, 313–319 (2012).
- [72] Xiao, F. *et al.* A general strategy to simulate osmotic energy conversion in multi-pore nanofluidic systems. *Materials Chemistry Frontiers* **2**, 935–941 (2018).
- [73] Gao, J. *et al.* Understanding the giant gap between single-pore-and membrane-based nanofluidic osmotic power generators. *Small* **15**, 1804279 (2019).
- [74] Kim, D.-K., Duan, C., Chen, Y.-F. & Majumdar, A. Power generation from concentration gradient by reverse electrodialysis in ion-selective nanochannels. *Microfluidics and Nanofluidics* **9**, 1215–1224 (2010).
- [75] Guo, W. *et al.* Energy harvesting with single-ion-selective nanopores: a concentration-gradient-driven nanofluidic power source. *Advanced functional materials* **20**, 1339–1344 (2010).
- [76] Gao, M., Tsai, P.-C., Su, Y.-S., Peng, P.-H. & Yeh, L.-H. Single mesopores with high surface charges as ultrahigh performance osmotic power generators. *Small* **16**, 2006013 (2020).
- [77] Macha, M., Marion, S., Nandigana, V. V. & Radenovic, A. 2d materials as an emerging platform for nanopore-based power generation. *Nature Reviews Materials* **4**, 588–605 (2019).
- [78] Graf, M. *et al.* Light-enhanced blue energy generation using mos2 nanopores. *Joule* **3**, 1549–1564 (2019).
- [79] Ma, T., Balanzat, E., Janot, J.-M. & Balme, S. Nanopore functionalized by highly charged hydrogels for osmotic energy harvesting. *ACS applied materials & interfaces* **11**, 12578–12585 (2019).
- [80] Pendse, A. *et al.* Highly efficient osmotic energy harvesting in charged boron-nitride-nanopore membranes. *Advanced Functional Materials* **31**, 2009586 (2021).
- [81] Bocquet, L. Nanofluidics coming of age. *Nature materials* **19**, 254–256 (2020).

-
- [82] Faucher, S. *et al.* Critical knowledge gaps in mass transport through single-digit nanopores: A review and perspective. *The Journal of Physical Chemistry C* **123**, 21309–21326 (2019).
- [83] Abraham, J. *et al.* Tunable sieving of ions using graphene oxide membranes. *Nature nanotechnology* **12**, 546–550 (2017).
- [84] Yang, Q. *et al.* Ultrathin graphene-based membrane with precise molecular sieving and ultrafast solvent permeation. *Nature materials* **16**, 1198–1202 (2017).
- [85] Wang, H. *et al.* Blue energy conversion from holey-graphene-like membranes with a high density of subnanometer pores. *Nano Letters* **20**, 8634–8639 (2020).
- [86] Walker, M. I. *et al.* Extrinsic cation selectivity of 2d membranes. *ACS nano* **11**, 1340–1346 (2017).
- [87] Graf, M. *et al.* Light-enhanced blue energy generation using mos2 nanopores. *Joule* **3**, 1549–1564 (2019).
- [88] Xin, W. *et al.* High-performance silk-based hybrid membranes employed for osmotic energy conversion. *Nature communications* **10**, 1–10 (2019).
- [89] Zhao, Y. *et al.* Robust sulfonated poly (ether ether ketone) nanochannels for high-performance osmotic energy conversion. *National Science Review* **7**, 1349–1359 (2020).
- [90] Ji, J. *et al.* Osmotic power generation with positively and negatively charged 2d nanofluidic membrane pairs. *Advanced Functional Materials* **27**, 1603623 (2017).
- [91] Liu, X. *et al.* Power generation by reverse electrodialysis in a single-layer nanoporous membrane made from core–rim polycyclic aromatic hydrocarbons. *Nature nanotechnology* **15**, 307–312 (2020).
- [92] Salanne, M. *et al.* Efficient storage mechanisms for building better supercapacitors. *Nature Energy* **1**, 1–10 (2016).
- [93] Zhang, Z. *et al.* Vertically transported graphene oxide for high-performance osmotic energy conversion. *Advanced Science* **7**, 2000286 (2020).
- [94] Mouhat, F., Coudert, F.-X. & Bocquet, M.-L. Structure and chemistry of graphene oxide in liquid water from first principles. *Nature communications* **11**, 1–9 (2020).
- [95] Ferrari, A. C. & Robertson, J. Interpretation of raman spectra of disordered and amorphous carbon. *Physical review B* **61**, 14095 (2000).
- [96] Dresselhaus, M., Jorio, A. & Saito, R. Characterizing graphene, graphite, and carbon nanotubes by raman spectroscopy. *Annu. Rev. Condens. Matter Phys.* **1**, 89–108 (2010).
- [97] Nakahara, M. & Sanada, Y. Modification of pyrolytic graphite surface with plasma irradiation. *Journal of materials science* **28**, 1327–1333 (1993).

-
- [98] Levita, G., Restuccia, P. & Righi, M. C. Graphene and mos2 interacting with water: A comparison by ab initio calculations. *Carbon* **107**, 878–884 (2016).
- [99] Hueso, J., Espinós, J., Caballero, A., Cotrino, J. & González-Elipe, A. Xps investigation of the reaction of carbon with no, o2, n2 and h2o plasmas. *Carbon* **45**, 89–96 (2007).
- [100] Gonella, G. *et al.* Water at charged interfaces. *Nature Reviews Chemistry* 1–20 (2021).
- [101] Grosjean, B., Bocquet, M.-L. & Vuilleumier, R. Versatile electrification of two-dimensional nanomaterials in water. *Nature communications* **10**, 1–8 (2019).
- [102] Maduar, S., Belyaev, A., Lobaskin, V. & Vinogradova, O. Electrohydrodynamics near hydrophobic surfaces. *Physical review letters* **114**, 118301 (2015).
- [103] Manghi, M., Palmeri, J., Yazda, K., Henn, F. & Jourdain, V. Role of charge regulation and flow slip in the ionic conductance of nanopores: An analytical approach. *Physical Review E* **98**, 012605 (2018).
- [104] Biesheuvel, P. & Bazant, M. Analysis of ionic conductance of carbon nanotubes. *Physical Review E* **94**, 050601 (2016).
- [105] Uematsu, Y., Netz, R. R., Bocquet, L. & Bonthuis, D. J. Crossover of the power-law exponent for carbon nanotube conductivity as a function of salinity. *The Journal of Physical Chemistry B* **122**, 2992–2997 (2018).
- [106] Joly, L., Ybert, C., Trizac, E. & Bocquet, L. Liquid friction on charged surfaces: From hydrodynamic slippage to electrokinetics. *The Journal of chemical physics* **125**, 204716 (2006).
- [107] Squires, T. M. Electrokinetic flows over inhomogeneously slipping surfaces. *Physics of Fluids* **20**, 092105 (2008).
- [108] Lin, C.-Y., Combs, C., Su, Y.-S., Yeh, L.-H. & Siwy, Z. S. Rectification of concentration polarization in mesopores leads to high conductance ionic diodes and high performance osmotic power. *Journal of the American Chemical Society* **141**, 3691–3698 (2019).
- [109] Ma, T., Balanzat, E., Janot, J.-M. & Balme, S. Nanopore functionalized by highly charged hydrogels for osmotic energy harvesting. *ACS applied materials & interfaces* **11**, 12578–12585 (2019).
- [110] Chua, L. Memristor-the missing circuit element. *IEEE Transactions on circuit theory* **18**, 507–519 (1971).
- [111] Strukov, D. B., Snider, G. S., Stewart, D. R. & Williams, R. S. The missing memristor found. *nature* **453**, 80–83 (2008).
- [112] Jo, S. H. *et al.* Nanoscale memristor device as synapse in neuromorphic systems. *Nano letters* **10**, 1297–1301 (2010).
- [113] Zou, X., Xu, S., Chen, X., Yan, L. & Han, Y. Breaking the von neumann bottleneck: architecture-level processing-in-memory technology. *Science China Information Sciences* **64**, 1–10 (2021).

- [114] An, H., Zhou, Z. & Yi, Y. Opportunities and challenges on nanoscale 3d neuromorphic computing system. In *2017 IEEE International Symposium on Electromagnetic Compatibility & Signal/Power Integrity (EMCSI)*, 416–421 (IEEE, 2017).
- [115] Sebastian, A., Le Gallo, M., Khaddam-Aljameh, R. & Eleftheriou, E. Memory devices and applications for in-memory computing. *Nature nanotechnology* **15**, 529–544 (2020).
- [116] Chua, L. O. & Kang, S. M. Memristive devices and systems. *Proceedings of the IEEE* **64**, 209–223 (1976).
- [117] Häusser, M. The hodgkin-huxley theory of the action potential. *Nature neuroscience* **3**, 1165–1165 (2000).
- [118] Ginoux, J.-M. & Rossetto, B. The singing arc: the oldest memristor? In *Chaos, CNN, Memristors and Beyond: A Festschrift for Leon Chua With DVD-ROM, composed by Eleonora Bilotta*, 494–507 (World Scientific, 2013).
- [119] Zhang, Y. *et al.* Brain-inspired computing with memristors: Challenges in devices, circuits, and systems. *Applied Physics Reviews* **7**, 011308 (2020).
- [120] Jo, S. H., Kim, K.-H. & Lu, W. Programmable resistance switching in nanoscale two-terminal devices. *Nano letters* **9**, 496–500 (2009).
- [121] Chen, J.-Y., Huang, C.-W., Chiu, C.-H., Huang, Y.-T. & Wu, W.-W. Switching kinetic of vcm-based memristor: evolution and positioning of nanofilament. *Advanced Materials* **27**, 5028–5033 (2015).
- [122] Ielmini, D. Resistive switching memories based on metal oxides: mechanisms, reliability and scaling. *Semiconductor Science and Technology* **31**, 063002 (2016).
- [123] Ielmini, D., Bruchhaus, R. & Waser, R. Thermochemical resistive switching: materials, mechanisms, and scaling projections. *Phase Transitions* **84**, 570–602 (2011).
- [124] Sarwat, S. G. Materials science and engineering of phase change random access memory. *Materials Science and Technology* **33**, 1890–1906 (2017).
- [125] Leong, I. W. *et al.* Quasi-stable salt gradient and resistive switching in solid-state nanopores. *ACS Applied Materials & Interfaces* **12**, 52175–52181 (2020).
- [126] Sheng, Q., Xie, Y., Li, J., Wang, X. & Xue, J. Transporting an ionic-liquid/water mixture in a conical nanochannel: a nanofluidic memristor. *Chemical Communications* **53**, 6125–6127 (2017).
- [127] Bu, Y., Ahmed, Z. & Yobas, L. A nanofluidic memristor based on ion concentration polarization. *Analyst* **144**, 7168–7172 (2019).
- [128] Robin, P., Kavokine, N. & Bocquet, L. Modeling of emergent memory and voltage spiking in ionic transport through angstrom-scale slits. *Science* **373**, 687–691 (2021).
- [129] Di Martino, G. & Tappertzhofen, S. Optically accessible memristive devices. *Nanophotonics* **8**, 1579–1589 (2019).

- [130] Zhang, P. *et al.* Nanochannel-based transport in an interfacial memristor can emulate the analog weight modulation of synapses. *Nano letters* **19**, 4279–4286 (2019).
- [131] Zhang, J., Kamenev, A. & Shklovskii, B. Conductance of ion channels and nanopores with charged walls: A toy model. *Physical review letters* **95**, 148101 (2005).
- [132] Kavokine, N., Marbach, S., Siria, A. & Bocquet, L. Ionic coulomb blockade as a fractional wien effect. *Nature nanotechnology* **14**, 573–578 (2019).
- [133] Tang, J. *et al.* Bridging biological and artificial neural networks with emerging neuromorphic devices: fundamentals, progress, and challenges. *Advanced Materials* **31**, 1902761 (2019).
- [134] Biological synapse. <https://www.vulgaris-medical.com/encyclopedie-medicale/synapse>. Accessed: 2021-09-06.
- [135] Tan, Z.-H. *et al.* Synaptic metaplasticity realized in oxide memristive devices. *Advanced Materials* **28**, 377–384 (2016).
- [136] Alle, H., Jonas, P. & Geiger, J. R. Ptp and ltp at a hippocampal mossy fiber-interneuron synapse. *Proceedings of the National Academy of Sciences* **98**, 14708–14713 (2001).
- [137] Wang, Z. *et al.* Memristors with diffusive dynamics as synaptic emulators for neuromorphic computing. *Nature materials* **16**, 101–108 (2017).
- [138] Kim, S. *et al.* Experimental demonstration of a second-order memristor and its ability to biorealistically implement synaptic plasticity. *Nano letters* **15**, 2203–2211 (2015).
- [139] Boyn, S. *et al.* Learning through ferroelectric domain dynamics in solid-state synapses. *Nature communications* **8**, 1–7 (2017).
- [140] Yao, P. *et al.* Fully hardware-implemented memristor convolutional neural network. *Nature* **577**, 641–646 (2020).
- [141] Yeon, H. *et al.* Alloying conducting channels for reliable neuromorphic computing. *Nature Nanotechnology* **15**, 574–579 (2020).
- [142] Wang, Z. *et al.* Fully memristive neural networks for pattern classification with unsupervised learning. *Nature Electronics* **1**, 137–145 (2018).
- [143] Shi, L., Zheng, G., Tian, B., Dkhil, B. & Duan, C. Research progress on solutions to the sneak path issue in memristor crossbar arrays. *Nanoscale Advances* **2**, 1811–1827 (2020).
- [144] Davis, S. J. *et al.* Pressure-induced enlargement and ionic current rectification in symmetric nanopores. *Nano Letters* **20**, 8089–8095 (2020).
- [145] Karnik, R., Duan, C., Castelino, K., Daiguji, H. & Majumdar, A. Rectification of ionic current in a nanofluidic diode. *Nano letters* **7**, 547–551 (2007).
- [146] Wu, Y. *et al.* 2d heterostructured nanofluidic channels for enhanced desalination performance of graphene oxide membranes. *ACS nano* **15**, 7586–7595 (2021).

-
- [147] Kim, S. J., Ko, S. H., Kang, K. H. & Han, J. Direct seawater desalination by ion concentration polarization. *Nature nanotechnology* **5**, 297–301 (2010).
- [148] Tu, Q., Yang, Q., Wang, H. & Li, S. Rotating carbon nanotube membrane filter for water desalination. *Scientific reports* **6**, 1–11 (2016).
- [149] Debanne, D., Daoudal, G., Sourdet, V. & Russier, M. Brain plasticity and ion channels. *Journal of Physiology-Paris* **97**, 403–414 (2003).
- [150] Somjen, G. G. Ion regulation in the brain: implications for pathophysiology. *The Neuroscientist* **8**, 254–267 (2002).
- [151] Rollings, R. C., Kuan, A. T. & Golovchenko, J. A. Ion selectivity of graphene nanopores. *Nature communications* **7**, 1–7 (2016).
- [152] Hong, S. *et al.* Scalable graphene-based membranes for ionic sieving with ultrahigh charge selectivity. *Nano letters* **17**, 728–732 (2017).
- [153] Ohno, T. *et al.* Short-term plasticity and long-term potentiation mimicked in single inorganic synapses. *Nature materials* **10**, 591–595 (2011).
- [154] Chua, L. If it is pinched it is a memristor. *Semiconductor Science and Technology* **29**, 104001 (2014).
- [155] Fioravante, D. & Regehr, W. G. Short-term forms of presynaptic plasticity. *Current opinion in neurobiology* **21**, 269–274 (2011).
- [156] Martin, S. J., Grimwood, P. D. & Morris, R. G. Synaptic plasticity and memory: an evaluation of the hypothesis. *Annual review of neuroscience* **23**, 649–711 (2000).
- [157] Rat hippocampal Neuron. <https://commons.wikimedia.org/w/index.php?search=rat+hippocampal+neuron&title=Special:MediaSearch&go=Go>. Accessed: 2021-08-11.
- [158] Elswick, D. *et al.* Advanced nanofabrication using helium, neon and gallium ion beams in the carl zeiss orion nanofab microscope. *Microscopy and Microanalysis* **19**, 1304–1305 (2013).
- [159] Randolph, S., Fowlkes, J. & Rack, P. Focused, nanoscale electron-beam-induced deposition and etching. *Critical reviews in solid state and materials sciences* **31**, 55–89 (2006).

RÉSUMÉ

Dans cette thèse, nous avons conçu et fabriqué un nouveau type de nano-canal en carbone destiné au passage de l'eau et des ions. Le transport ionique dans ces canaux est fortement amplifié grâce à une combinaison favorable de charge de surface et de glissement hydrodynamique. Cela permet de convertir efficacement l'énergie osmotique, provenant de gradients salins. De plus, on montre que ces canaux possèdent une mémoire à long terme. Nous utilisons cette mémoire pour implémenter des algorithmes d'apprentissage inspiré des synapses biologiques.

MOTS CLÉS

Nanofluidique, matériaux 2D, transport ionique, énergie osmotique, memristor, synapses

ABSTRACT

In this thesis, we designed and fabricated a new kind of water and ionic nanochannel made of carbon. They exhibit ionic transport of considerable magnitude thanks to a combination of high surface charge and hydrodynamic slippage. This enables efficient harvesting of osmotic energy, coming from salinity gradients. Furthermore, we found that these channels possess a long-term memory. We used this memory to implement learning algorithms inspired by biological synapses.

KEYWORDS

Nanofluidics, 2D materials, ionic transport, osmotic energy, memristor, synapses

